

Structural and Functional Imaging of Pancreatic Islets using Optical Coherence Microscopy

THÈSE N° 6560 (2015)

PRÉSENTÉE LE 1^{ER} MAI 2015

À LA FACULTÉ DES SCIENCES ET TECHNIQUES DE L'INGÉNIEUR
LABORATOIRE D'OPTIQUE BIOMÉDICALE
PROGRAMME DOCTORAL EN PHOTONIQUE

ÉCOLE POLYTECHNIQUE FÉDÉRALE DE LAUSANNE

POUR L'OBTENTION DU GRADE DE DOCTEUR ÈS SCIENCES

PAR

Corinne BERCLAZ

acceptée sur proposition du jury:

Prof. N. Grandjean, président du jury
Prof. T. Lasser, Prof. A. Grapin-Botton, directeurs de thèse
Prof. L. Bouwens, rapporteur
Dr E. Ilegems, rapporteur
Prof. E. Liebling, rapporteur



ÉCOLE POLYTECHNIQUE
FÉDÉRALE DE LAUSANNE

Suisse
2015

Abstract

In diabetes, pancreatic β -cells play a key role. These cells are organized within structures called islets of Langerhans inside the pancreas and produce insulin. Insulin is one of the main hormones contributing to glucose homeostasis, i.e, a stable regulation of blood sugar. A decreased secretion of insulin leads to hyperglycemia, which is the hallmark of diabetes. *In vivo* imaging of β -cells and their function are required for diagnosis purposes and assessment of new treatments. However, this task is challenging due to the localization of the pancreas deep inside the abdominal cavity, the small size of islets of Langerhans (ranging from 30-500 μm in diameter) and their heterogeneous distribution throughout the organ. Indeed, islets of Langerhans represent only 1-2% of the pancreas' total volume.

All state-of-the-art medical imaging techniques such as Magnetic Resonance Imaging (MRI), Single-Photon Emission Computed Tomography (SPECT) or Positron Emission Tomography (PET) cannot resolve individual islets. Furthermore, they require the use of tracers to detect the β -cells. Hence, the research for imaging islets of Langerhans, including the identification of specific β -cell tracers is a highly active field of research. Indeed, no marker is currently available for clinical studies and diagnosis. For animal models, optical techniques offer a sufficient spatial resolution to image individual islets with a high specificity provided by fluorescent markers.

Optical Coherence Microscopy (OCM) is a novel interferometric imaging technique measuring the back-scattered light from a sample to reveal its structure in depth. OCM provides an intrinsic contrast depending on the spatial variation of the index of refraction. A Fourier transform of the acquired spectrum extracts the whole depth structure, thereby requiring only scans in two dimensions to obtain a three-dimensional image with a fast acquisition time.

In this thesis, we exploited the label-free capabilities and fast acquisition rate of OCM to study islets of Langerhans. We demonstrated that OCM signal is specific to the β -cell volume due to the dominant scattering of the zinc-insulin crystalline structures inside the secretory granules. Besides structural information, OCM reveals the vascularization of pancreatic islets *in situ*. These advantages were exploited to image the progression of autoimmune diabetes and for the characterization of β -cell tracers. The intrinsic contrast of OCM does not require genetically modified mice, nor the use of exogenous agents to image islets and their vascularization. OCM enhanced with a confocal fluorescence channel can assess β -cell tracers labeled with a fluorophore *in vitro* and *in vivo* in wild

type mice. As a proof of principle, we assessed the specificity of Cy5.5-exendin-3, an analogue of the glucagon-like peptide-1 receptor (GLP1R) for β -cells. Our results confirmed the co-localization of the fluorescence-tagged tracer with the OCM islet signal. Time-lapse imaging reveals the accumulation of this tracer in the endocrine pancreas a few minutes after injection and lasting over 4 hours. The high resolution of OCM serves as a pre-clinical optical platform to facilitate the initial tests aiming to determine the specificity of β -cell tracers *in vivo* in mice.

Finally, in order to perform non-invasive longitudinal studies, islets of Langerhans were transplanted into the anterior chamber of the eye. This transplantation model allowed us to follow individual islets over time during the autoimmune inflammation progression in a spontaneous mouse model of type I diabetes. Using this approach, we quantified the inflammation process together with the vascularization. We demonstrated that alterations of the islet microvasculature accompany the progression of diabetes with a strong correlation between the degree of insulitis and the density of the vascular network.

Keywords: Optical coherence Microscopy (OCM), Fourier domain or spectral domain, extended focus OCM (xfOCM), dark field OCM (dfOCM), islet of Langerhans, vascularization, angiography, blood flow, *in vivo* imaging, 3-dimensional imaging, fluorescence, label-free, exendin-3, glucagon-like peptide 1 receptor, quantitative imaging, nonobese diabetic mouse, longitudinal, anterior chamber of the eye.

Résumé

Les cellules β pancréatiques ont un rôle majeur dans le diabète. Elles s'organisent en structures appelées îlots de Langerhans dans le pancréas et produisent l'insuline. L'insuline est une des hormones qui contribue à l'homéostasie du glucose, c'est-à-dire une régulation stable du niveau de sucre dans le sang. Une diminution de la production d'insuline cause l'hyperglycémie, qui est une caractéristique importante du diabète. L'imagerie *in vivo* des cellules β et de leur fonction est requise pour le diagnostic et l'évaluation de nouveaux traitements. Cependant, il s'agit d'une tâche ardue en raison de la localisation des îlots dans le pancréas, un organe situé à l'intérieur de la cavité abdominale, et donc difficilement accessible. De plus, les îlots dont le diamètre varie entre 30-300 μm sont distribués de manière non-homogène à travers le pancréas et représentent seulement 1 à 2% du volume total de l'organe.

Toutes les techniques d'imagerie médicales disponibles, telles que l'imagerie par résonance magnétique (MRI), la tomographie d'émission monophotonique (SPECT) ou la tomoscintigraphie par émission de positons (PET) ne peuvent pas résoudre d'îlots individuels. En outre, elles nécessitent l'utilisation d'un traceur pour détecter les cellules β . Par conséquent, l'imagerie des îlots de Langerhans ainsi que l'identification de traceurs pour les cellules β sont des domaines de recherche très actifs. En effet, il n'existe pas encore de traceur disponible pour des études cliniques ou pour le diagnostic. Pour des modèles animaux, les méthodes optiques possèdent un pouvoir de résolution spatial qui permet l'imagerie d'îlots individuels avec une haute spécificité en utilisant des marqueurs fluorescents.

La microscopie par cohérence optique (OCM) est une nouvelle technique d'interférométrie qui mesure la lumière rétrodiffusée par un échantillon, permettant ainsi de révéler sa structure en profondeur. L'OCM possède un contraste intrinsèque qui dépend des variations spatiales de l'indice de réfraction. Une transformée de Fourier du spectre extrait l'information sur toute la profondeur, permettant ainsi d'effectuer seulement un balayage de l'échantillon en deux dimensions pour obtenir un volume complet avec un temps d'acquisition court.

Dans cette thèse, nous exploitons l'avantage de la microscopie sans agent de contraste et la rapidité d'acquisition de l'OCM pour étudier les îlots de Langerhans. Nous démontrons que le signal en OCM des îlots de Langerhans est spécifique aux cellules β grâce à la rétrodiffusion dominante des structures cristallines composées d'insuline et de zinc stockées dans les granules sécrétrices. Outre des informations structurales, l'OCM

révèle la vascularisation des îlots dans le pancréas. Ces avantages ont été exploités pour l'imagerie de la progression du diabète auto-immune et pour caractériser la spécificité de traceurs pour les cellules β . La microscopie sans agent de contraste ne requiert ni de souris modifiées génétiquement pour détecter les îlots, ni l'injection d'un agent de contraste pour révéler la vascularisation. L'ajout d'un canal de fluorescence à l'OCM permet de déterminer la spécificité de traceurs marqués avec un fluorophore pour les cellules β , tant au niveau cellulaire que dans des souris. Nous illustrons cette fonctionnalité en évaluant la spécificité du traceur Cy5.5-exendine-3, un analogue du récepteur glucagon-like peptide-1 (GLP1R) pour les cellules β . Nos résultats confirment la co-localisation du traceur marqué avec un fluorophore avec le signal OCM de l'îlot. Des images dans le temps montrent l'accumulation du traceur dans la partie endocrine du pancréas quelques minutes après l'injection et qui persiste 4 heures après l'injection. La haute résolution de l'OCM sert de plateforme pré-clinique facilitant les tests initiaux visant à déterminer la spécificité de marqueurs pour les cellules β chez les souris.

Enfin, afin d'effectuer des études longitudinales, nous avons adopté le modèle de transplantation d'îlots dans la chambre antérieure de l'œil. Ce modèle de transplantation a permis d'étudier dans le temps des îlots individuels durant la progression de l'inflammation auto-immune dans un modèle spontané du diabète de type I chez la souris. Grâce à cette approche, nous avons quantifié l'inflammation des îlots en même temps que la vascularisation. Nous avons ainsi démontré qu'une altération de la microvascularisation accompagne la progression du diabète avec une forte corrélation entre le degré d'inflammation et la densité de la vascularisation.

Mots clés : microscopie par cohérence optique (OCM), détection dans le domaine de Fourier (FDOCM), OCM à profondeur de champ (xfOCM), OCM à champ sombre (dfOCM), îlots de Langerhans, vascularisation, angiographie, flux sanguin, imagerie dans un organisme vivant, imagerie en trois dimensions, fluorescence, imagerie sans agent de contraste, exendin-3, récepteur du glucagon-like peptide 1, imagerie quantitative, souris diabétique non-obèse, longitudinal, chambre antérieure de l'œil.

Contents

Abstract (English/Français)	i
1 General concepts	1
1.1 Pancreas, islets and β -cells	1
1.2 Diabetes mellitus	3
1.3 Imaging the pancreas	5
1.3.1 Structural imaging of islets of Langerhans	5
1.3.2 Vascularization and blood flow in the pancreas and islets of Langerhans	7
1.4 Light: an electromagnetic wave	8
1.5 Optical Coherence Microscopy	10
1.6 Thesis objectives	14
2 Label-free structural imaging of the pancreas	15
2.1 Journal article	16
2.1.1 Introduction	16
2.1.2 Methods	18
2.1.3 Results	25
2.1.4 Discussion	30
2.1.5 Conclusion	32
3 Label-free functional imaging of the pancreas	35
3.1 Introduction	35
3.2 Research design and methods	36
3.3 Results	41
3.4 Discussion	46
4 OCM and the specificity of β-cell tracers	49
4.1 Specific tracers for β -cells	49
4.2 Journal article	52
4.2.1 Introduction	52
4.2.2 Research design and methods	53
4.2.3 Results	56

Contents

4.2.4	Discussion	63
5	Label-free longitudinal study of type I diabetes	69
5.1	Journal article	70
5.1.1	Introduction	71
5.1.2	Results	73
5.1.3	Discussion	81
5.2	Material and Methods	86
5.2.1	Animals	86
5.2.2	Pancreatic islet isolation, culture and ACE transplantation	86
5.2.3	Immunohistochemistry	87
5.2.4	<i>Ex vivo</i> imaging with dfOCM	87
5.2.5	FOCI imaging	88
5.2.6	Data processing	89
5.2.7	Image post processing	92
5.3	ACE long term imaging	94
6	Conclusion and Perspective	97
	Acknowledgements	103
	Bibliography	123
	Curriculum Vitae	123

1 General concepts

1.1 Pancreas, islets and β -cells

The pancreas is a gland located in the abdominal cavity (Fig. 1.1). This organ is attached to the stomach, the duodenum and the spleen. The pancreas has two distinct functions: an exocrine function involved in digestion and an endocrine function important for glucose homeostasis. The major part of the pancreas consists of exocrine tissue composed of acinar cells producing digestive enzymes and ducts that transport these enzymes into the duodenum. The endocrine function is assumed by structures called islets of Langerhans, which are scattered throughout the exocrine tissue, and release hormones into the blood vessels. The endocrine tissue represents only 1-2% of the total mass of the pancreas. The islet size (ranging from ~ 30 -500 μm) is conserved among different species [1] whereas the number of islets depends on the species. Indeed, the human pancreas contains ~ 1 million of islets [2, 3] whereas a mouse pancreas contains ~ 4500 islets as demonstrated using Optical Projection Tomography (OPT) [4]. A human pancreas weighs between 60-100 g (12-15 centimeters long), therefore the β -cell mass represents only around 1-2 g.

In rodents, islets of Langerhans are made of a core of β -cells (75%) producing insulin surrounded by a ring of α -cells (19%), δ -cells (6%), PP-cells and ϵ -cells producing glucagon, somatostatin, pancreatic polypeptide and ghrelin, respectively [5]. Human islets have a more heterogeneous organisation, with more α -cells (35%) and δ -cells (11%) mixed with the β -cells (54 %) [5–7]. Insulin is stored in secretory granules in a crystalline form made of hexamers of two zinc ions per six insulin molecules [8, 9]. A β -cell contains $\sim 10'000$ granules [10], each with a diameter of ~ 240 nm and carrying $\sim (3 - 4) \cdot 10^5$ insulin molecules [11, 12]. Insulin regulates glucose homeostasis mainly through its action on the liver, muscles and adipose tissues. Additional insulin target cells can be found in the central nervous system, endocrine cells of the pancreas and the gut. These target cells participate in glucose clearance from the blood upon insulin signal transduction. Insulin secretion is a complex process where glucose concentration is one of the important actors. The autonomic nervous system [13] and incretin hormones from

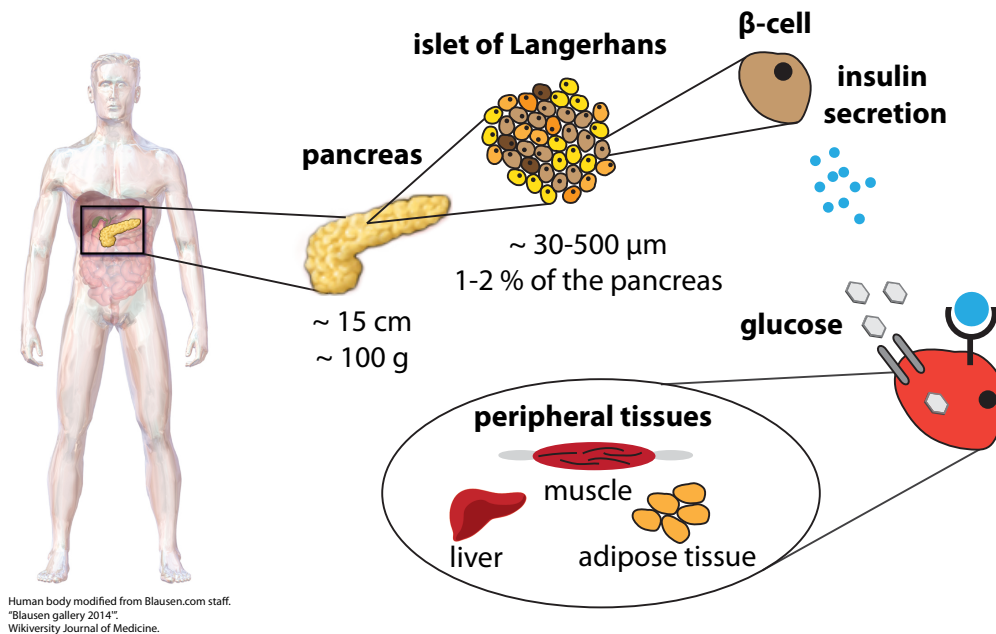


Figure 1.1: **Overview of the relation between the pancreas, islets of Langerhans, β -cells and insulin.** Insulin enables peripheral cells to take up glucose from the blood stream.

the intestines such as glucagon-like peptide 1 (GLP1) and gastrointestinal insulinotropic peptide (GIP) [3] also regulate insulin secretion. Amino acids alone do not trigger insulin secretion or enhance glucose-stimulated insulin secretion (GSIS) [14, 15]. However, either an acute administration of individual amino acids or a mixture of specific amino acids at physiological concentrations can increase GSIS [16]. Indeed, co-injections of carbohydrate with a mixture of amino acids and protein increase insulin response in type II diabetic patients [17]. Similarly, fatty acids can be important for GSIS, but in the absence of glucose they have no effect on GSIS [18]. Undeniably, islets of Langerhans are important actors in glucose homeostasis. However, recently there have been indications that adipose tissues contribute to glucose homeostasis by secretion of adipokines such as adiponectin and leptin [19, 20]. Leptin treatments in a spontaneous autoimmune mouse model or in chemically induced (alloxan, streptozotocin) diabetic mice restore normoglycemia [21–23], even in the absence of increased insulin secretion. Similarly, grafts of brown adipose tissue can revert diabetes [24]. The full mechanisms beyond this glucose regulation are not yet fully elucidated. Finally, an underestimated player of glucose homeostasis is the brain. Indeed, there are evidences that the brain can regulate glucose via both insulin dependent and insulin-independent mechanisms [25]. This suggests a tight link between the brain and the pancreatic islets in glucose homeostasis.

Although the endocrine part constitutes a small portion of the pancreas, it receives around 5% to 15% of the total pancreatic blood flow [26–30]. Pancreatic blood vessels have a particular anatomy both at the organ level and inside islets of Langerhans. In the

pancreas, larger islets are located centrally near large blood vessels whereas smaller islets are mainly situated at the periphery of the organ [31, 32]. Inside the islets of Langerhans capillaries form a glomerular-like network [32], which is ten times more fenestrated than exocrine capillaries [33].

A correct vascularization of the islets seems required for a proper secretion of the different hormones [34–36]. Different studies suggest that the specific organisation of the different cell types inside islets of Langerhans and the vascularization pattern are functionally linked. Three different blood flow patterns have been proposed: (i) *inner-to-outer* in which the center β -cells are perfused before the other endocrine cells, (ii) *outer-to-inner* in which the non- β -cells are first perfused and (iii) *top-to-bottom* where the islet is perfused from one side to another independently of the cell types [26, 37]. However, by using line-scanning confocal microscopy, Nyman *et al.* [38] showed a preferential *inner-to-outer pattern* in murine islets although 35% of the islets had a *top-to-bottom* pattern. These results are in agreement with studies that indicate an *inner-to-outer* pattern in hamster [39], rat and human islets by using corrosion cast [32] or anterograde and retrograde perfusion experiments [40–42]. Furthermore, blood flow is tightly regulated by glucose. Indeed, different techniques have shown in rodents an increased blood flow in the endocrine pancreas during hyperglycemia whereas no blood flow change was observed in the exocrine part [28, 30, 43]. The studies reported above seem to indicate that vascularization plays an important role in the functioning of islets of Langerhans. However, different studies targeting the vascular endothelial growth factor¹ (VEGF) [35, 45, 46] indicate that a 50% decrease of the islet vasculature does not impair β -cell survival. Yet, impaired glucose tolerance have been observed with a decrease in the first phase of insulin secretion but no change in β -cell mass or proliferation. Nevertheless, there are indications that islet vascularization is remodeled during the pathogenesis of diabetes [47–49] and that the vascular permeability is decreased [30, 50–52].

1.2 Diabetes mellitus

The hallmark of diabetes is hyperglycemia resulting from insufficient insulin secretion from pancreatic β -cells, insulin resistance of tissues or a combination of both. Other symptoms of diabetes are ketoacidosis, polyuria, polydipsia, weight loss and blurred vision. Long term effects of diabetes include retinopathy, renal failure, peripheral neuropathy (foot ulcers, amputations), increase risk of heart and cerebrovascular diseases [53]. According to the World Health Organisation (WHO), more than 340 million people worldwide have diabetes [54, 55].

Diabetes can be separated into type I and type II diabetes mellitus [56]. Type I diabetes mellitus (T1DM) accounts for 5-10% of diabetic people, but its prevalence

¹Vascular endothelial growth factor (VEGF) stimulates angiogenesis and has been shown to be involved in the vascularization of pancreatic islet [44].

is increasing [57]. The characteristic of T1DM is an auto-immune destruction of β -cells, which results in an insufficient insulin production [58–60]. T1DM is a polygenic disorder [61] with environmental factors [62]. Indeed, the concordance rate between monozygotic twins is only around 50% [63]. T1DM is usually diagnosed before or during puberty even if later diagnosis sometimes occurs. Treatment of T1DM includes daily exogenous insulin injection and multiple blood glucose tests. An alternative, but rare treatment is the transplantation of islets of Langerhans [64] (Edmonton protocol [65]) or pancreas transplantation [66]. In most cases, transplantation of islets of Langerhans is performed into the liver through the hepatic portal vein. However, the scarcity of organ donors and the need of multiple cadaveric pancreases to transplant one patient is a limiting factor. In addition, transplantation success is limited since only 10% of the patients are insulin-independent 5 years after transplantation [67–69].

Type II diabetes mellitus (T2DM) accounts for the majority of diabetic people. T2DM is more heterogeneous than T1DM, involving both defects in insulin secretion and insulin action (insulin resistance) [70], and is often associated with obesity and older age even if genetic factors have been discussed [71]. Treatments for T2DM include insulin injection or other drugs that target β -cell or peripheral tissues. In general, drugs that would preserve the β -cell mass by promoting proliferation, preventing apoptosis or improving insulin secretion are potential treatments for both types of diabetes [72].

In most patients, diabetes is a multi-factorial disease with environmental factors and multiple genetic predispositions. However, maturity onset diabetes of the young (MODY) are examples of rare monogenic autosomal dominant inherited forms of diabetes. Up to now, mutations in 6 genes have been reported in MODY [73, 74]. Some syndromic forms of MODY are associated with defects in other organs. Indeed, mutations in the hepatocyte nuclear factor (HNF) as in MODY3 (HNF-1 α) have been associated with liver defects [75] and mutations in HNF-1 β present in MODY5 are mainly linked to kidney defects (renal cysts) [76, 77].

There are also rare cases of neonatal diabetes (transient or permanent), with no evidence of autoimmune markers. This neonatal diabetes are mainly due to mutations in genes involved in β -cells function and pancreas development [78]. Finally, gestational diabetes mellitus is defined as glucose intolerance during the pregnancy. Even if usually glycemia is restored after delivery, gestational diabetes is associated with a higher risk to develop diabetes in the future [79].

To mimic diabetes mellitus, rodent models have been extensively used in diabetes research to study the pathogenesis and its complications [80, 81]. Similarly, new treatments and preventative strategies are initially tested in animals. Animal models for T1DM can be chemically induced by using drugs such as alloxan or streptozotocin, which selectively destroy β -cells. Spontaneous models of T1DM exist both in the Biobreeding (BB) rat [82] and Nonobese diabetic (NOD) mouse [83]. Nevertheless, the most widely used model

in the literature is the NOD mice. In the NOD mice, 60-90% of females and 10-30% of males spontaneously develop T1DM. Some NOD mice show an inflammation of the islets, a process called insulinitis already at 4-5 weeks old and develop diabetes around 10-14 weeks [84–86]. Animal models for T2DM are also available [87]. Mice deficient for leptin signaling are widely used as a model for T2DM. Leptin is a hormone that regulates food intake. Rodents that carry mutations either in the leptin (ob/ob mice) or in the leptin receptor (db/db mice, Zucker Diabetic Fatty rat) become obese and insulin resistant [88, 89]. An alternative and closer model to the reality of T2DM are high fat diet mice [90].

1.3 Imaging the pancreas

1.3.1 Structural imaging of islets of Langerhans

Currently, the progression of diabetes can only be monitored in indirect ways, e.g., blood glucose, HbA1c levels (glycated haemoglobin indicates the average blood sugar level over weeks/months), insulin, and C-peptide measurements. A more direct and informative way of monitoring the progress of the disease would be via direct imaging of the β -cells, and especially their mass, to follow diabetes progression. However, this is challenging for multiple reasons: (1) the localization of the pancreas deep inside the abdominal cavity, (2) the low density of these islets in the pancreas and (3) their varying shape and small size, which varies from 30 to 300 μm in diameter. Therefore, an ideal imaging technique should have a high spatial resolution, a good sensitivity, a sufficient penetration depth, a large field of view, and be fast. Several methods are available for imaging β -cells, always with a trade-off between penetration depth and resolution. A global overview of these methods is provided in Figure 1.2.

Non-invasive techniques such as Magnetic Resonance Imaging (MRI), Positron Emission Tomography (PET), and Single-Photon Emission Computed Tomography (SPECT) are currently the most suitable methods for human pancreas imaging. SPECT and PET have a higher sensitivity but lower resolution than MRI. In a recent paper, Lamprianou *et al.* showed an enhanced contrast of murine islets after manganese infusion based on MRI. This small animal imaging enabled the localization of big islets ($> 50 \mu\text{m}$) with a 14.1 Tesla MRI instrument [91]. Standard equipments used in clinical settings have a much lower spatial resolution ($> 5 \text{ mm}$) and can therefore not resolve individual islets [92, 93]. Nevertheless, imaging of the pancreas after manganese injection allows discriminating type II diabetic and normoglycemic patients with 1.5 Tesla MRI [94] and is sensitive enough to detect a β -cell mass decrease before the clinical onset of T1DM in mice with a 7 Tesla MRI [95]. In addition, MRI and SPECT/PET require the use of contrast agents or radioligands to distinguish between the endocrine and exocrine pancreas. No contrast agent currently has the appropriate specificity for β -cell imaging to be used in clinics [96, 97]. Even though, from a clinical point of view, only non-invasive techniques are appropriate, invasive or semi-invasive techniques could be

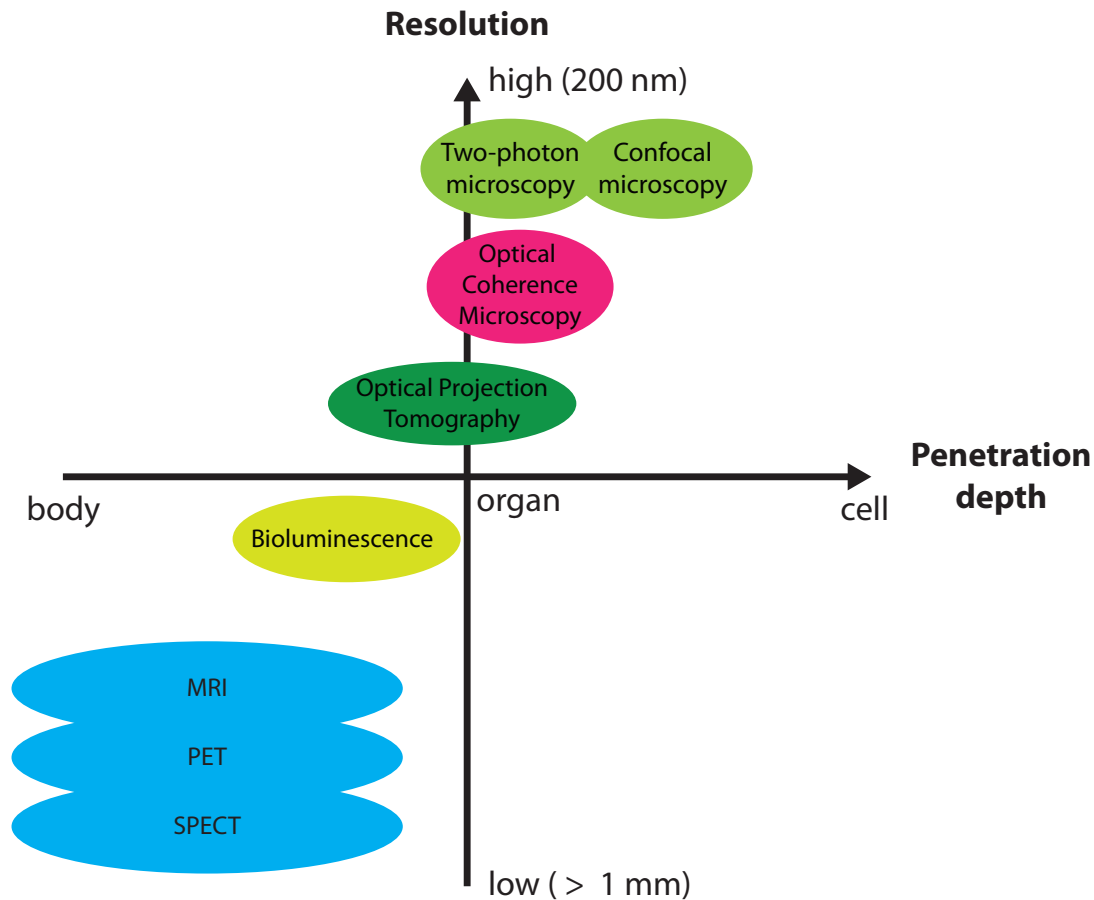


Figure 1.2: **Overview of the different techniques available for β -cell imaging as a function of their resolution and penetration depth.** Except OCM, all these techniques require labeling. MRI, PET and SPECT are the only non-invasive techniques applied in clinical settings.

used as a tool for understanding the mechanisms underlying diabetes in animal models. To date, immunohistochemistry of the pancreas has been the most widely used technique to quantify the β -cell volume. This method is limited to 2-dimensional view of fixed tissue lacking spatial and temporal information and it may lead to biases. This approach, while being technically straightforward, is time consuming, and is not suitable for analyzing a large cohort of mice. In order to perform quantitative studies on a large number of animals, new methods capable of visualizing and determining the β -cell volume are needed. For animal research, bioluminescence imaging of transgenic mice expressing luciferase in β -cells is very sensitive, and has a better resolution than MRI or PET [98–101]. However, bioluminescence has a very poor axial resolution that makes it unable to resolve individual islets. The development of transgenic mice expressing the green fluorescent protein (GFP) in β -cells [102, 103] allowed the use of optical techniques

to image the pancreatic islets. Optical techniques like confocal microscopy allow for very high resolution, but their penetration depth is limited to about 50 μm [38] in the pancreas. Two-photon microscopy allows for a deeper penetration of about 250 μm in the pancreas [104]. However, it is limited to small sample sizes due to the time-consuming three-dimensional scanning required. In contrast, Optical Projection Tomography (OPT), is ideal to obtain a global and quantitative measurement of the β -cell volume, but is limited to *ex vivo* small organ imaging [4, 31, 105, 106]. Still, these methods depend on fluorescent labels.

Optical Coherence Microscopy (OCM) is the only reported technique to resolve *in vivo* and *ex vivo* individual islets without labeling up to 300-400 μm in depth with a micrometric resolution [107]. Owing to this label-free property, OCM does not rely on genetically engineered mice to detect islets [92]. Therefore, it holds great promises to better understand changes in β -cell volume during diabetes progression.

Furthermore, transplantation of islets into the anterior chamber of the eye [108] is a new method that allows longitudinal and non-invasive studies of islets. This approach enables to monitor re-vascularization of the graft [109], the immune response after transplantation [110], the autoimmune response in T1DM [111, 112], the autonomic nervous system innervation of islets [13], islet plasticity [113] and the role of β -cell volume during the onset and remission of T1DM [114]. A study in a baboon model rendered diabetic with streptozotocin demonstrates that the grafted islets are functional in this location and control glucose homeostasis over almost a year [115].

1.3.2 Vascularization and blood flow in the pancreas and islets of Langerhans

The deep localization of the pancreas in the abdominal cavity and the distribution of the islets throughout the pancreas renders imaging their vascular network and blood flow measurements very challenging. To measure the blood flow in the pancreas, one method consists in injecting microspheres into the blood stream. During the experiment, reference blood samples are taken. After dissection, the number of microspheres in the organ is compared to the average number of microspheres in these reference blood samples. Blood flow Q_{org} is calculated by counting the number of microspheres in the islet N_{org} using the following equation: $Q_{org} = Q_{ref} \times N_{org}/N_{ref}$ where N_{ref} represents the number of microsphere present in a blood sample and withdrawn at a rate Q_{ref} . This microsphere-based technique was applied mainly on rats and showed that (1) the endocrine part received approximatively 10% more blood flow than the exocrine pancreas [29] and (2) after glucose injection, islets blood flow increases by about 80% [28, 30] whereas insulin injection has no influence on islets blood flow [116]. *In vivo* measurements have been achieved through intravital fluorescent microscopy either in the native pancreas [38, 43, 117] or in grafted islets in striated muscle by using a dorsal window [39, 118–120]. The blood flow is measured by injecting labeled dextran or labeled red blood cells.

Recently, Nyman *et al.* [38] showed that there are two predominant blood flow patterns in murine islets: (1) a perfusion of the β -cell core center before the peripheral part and (2) a perfusion from one side to the other of the islet regardless of cell type. They confirmed that glucose infusion increases islet blood flow without change in the exocrine pancreas [43]. Nevertheless, islets blood flow patterns are still subject to discussion. Closer to clinical imaging, MRI using paramagnetic contrast agent is applied in animal models to see difference in vascular permeability [52, 121].

1.4 Light: an electromagnetic wave

The relevant description of light in the context of this thesis is based on wave theory where light is described as an electromagnetic field, which can be expressed as [122]:

$$E_R(z, t) = a(z) \cos(kz - \omega t + \phi) \quad (1.1)$$

where z is the spatial coordinate along the propagation axis, t the temporal coordinate, and $a(z)$ is the amplitude of the wave. k is the wavenumber defined as $k = \frac{2\pi}{\lambda}$ where λ is the wavelength. $\omega = 2\pi\nu$ is the angular frequency related to the frequency ν and ϕ the phase. The light frequency can also be related to the speed of light in vacuum c_0 and the refractive index n of the medium: $\nu = \frac{c_0}{\lambda n}$. The sign of the wavenumber dependency is related to the forward or backward propagation. Assuming $\phi = 0$ and using the Euler's formulas², we can rewrite the real wavefunction $E_R(z, t)$ (Equation 1.1) using complex notation:

$$E(z, t) = a(z) e^{i\omega t} e^{-ikz} \quad (1.2)$$

If we look only at the time dependence, we can write:

$$E(t) = a e^{i\omega t} \quad (1.3)$$

Figure 1.3a shows a graphical representation of Equation 1.3. Here, the light field is represented by an arrow rotating with a frequency ω .

The frequency of light is in the order of 10^{14} Hz, which is too fast to be detected by any detector. Detectors integrate over a certain time T (much longer than an optical period $\frac{1}{\nu}$) and measure the light intensity instead of the field amplitude:

$$I = \langle EE^* \rangle = \frac{1}{T} \int_0^T E(t) E^*(t) dt = |E(t)|^2 \quad (1.4)$$

where $E^*(t)$ is the complex conjugate of $E(t)$. Interferometry compares or correlates light fields propagating over a certain distance. This distance translates into a phase

² $\cos(\theta) = \frac{e^{i\theta} + e^{-i\theta}}{2}$

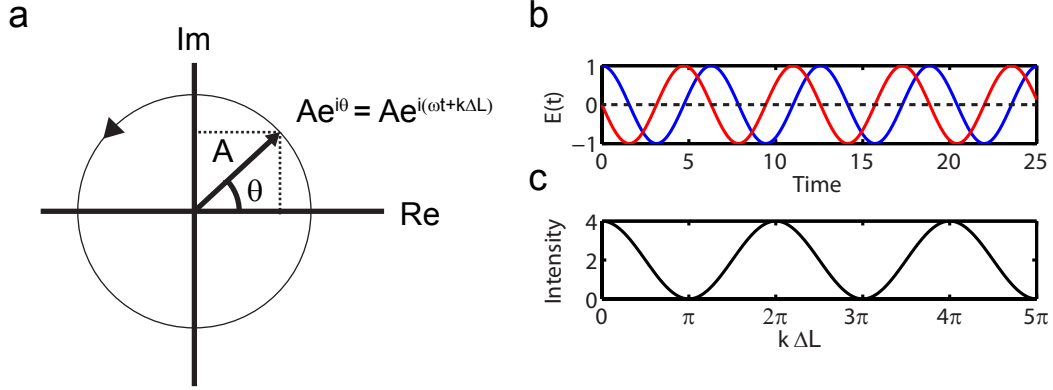


Figure 1.3: **Representation of a light wave.** (a) Representation of the complex wave as a vector rotating with a pulsation ω on the real (Re) and imaginary (Im) axis. (b) Two waves with a phase delay and (c) intensity resulting of the superposition of two coherent waves as a function of the phase difference.

shift $\phi = k \Delta L = 2\pi \Delta L / \lambda$ where L represents a distance. The corresponding shifted wave is described as:

$$E(t) = a e^{i(\omega t + \phi)} = a e^{i(\omega t + k \Delta L)} \quad (1.5)$$

Figure 1.3b represents two waves with the same frequency but shifted by $k \Delta L$. If we denote:

$$E_1(t) = a_1 e^{i\omega t} \quad \text{and} \quad E_2(t) = a_2 e^{i(\omega t + \phi)} = a_2 e^{i(\omega t + k \Delta L)}, \quad (1.6)$$

the intensity of $E_1(t)$ alone is $I_1 = \langle E_1 E_1^* \rangle = a_1 e^{i\omega t} \cdot a_1 e^{-i\omega t} = a_1^2$. Similarly for $E_2(t)$, the intensity is $I_2 = a_2^2$. However, the intensity detected by the *superposition* of these two coherent fields yields:

$$\begin{aligned} I &= \langle (E_1 + E_2)(E_1 + E_2)^* \rangle = \langle |E_1|^2 + |E_2|^2 + E_1 E_2^* + E_2 E_1^* \rangle \\ &= |a_1 e^{i\omega t}|^2 + |a_2 e^{i(\omega t + k \Delta L)}|^2 + a_1 a_2 e^{i\omega t} e^{-(i\omega t + k \Delta L)} + a_1 a_2 e^{-i\omega t} e^{i(\omega t + k \Delta L)} \\ &= a_1^2 + a_2^2 + a_1 a_2 e^{(-k \Delta L)} + a_1 a_2 e^{(k \Delta L)} \\ &= a_1^2 + a_2^2 + 2 a_1 a_2 \cos(k \Delta L) \end{aligned}$$

If we assume equal field strengths, i.e, $a = a_1 = a_2$, we obtain:

$$I = 2a^2 + 2a^2 \cos(k \Delta L) = 2a^2(1 + \cos(k \Delta L)) \quad (1.7)$$

The intensity in an interferogram depends directly on the value of $k \Delta L$. If $\cos(k \Delta L) = 1$, the recorded intensity is $I = 4a^2$, which is higher than the sum of the intensities of the two beams. On the other hand, if $\cos(k \Delta L) = -1$, the recorded intensity is $I = 0$.

Here, we see directly *constructive* and *destructive* interferences:

- constructive interference if $k\Delta L = 2n\pi$, with $n = 0, 1, 2, \dots$
- destructive interference if $k\Delta L = (2n + 1)\pi$ with $n = 0, 1, 2, \dots$

Figure 1.3c depicts the measured intensity in function of the phase delay $k\Delta L$.

1.5 Optical Coherence Microscopy

Optical Coherence Microscopy (OCM) enables non-invasive cross-sectional imaging of biological tissue by detecting the back-reflections of a broadband light source from a sample. OCM is an interferometric imaging method based on Optical Coherence Tomography (OCT), but with a lateral resolution increased by optics with higher numerical aperture (NA). The contrast of OCM depends on the variation of index of refraction in the sample. In order to assess the sample in depth, the scattered light is superimposed with a strong reference field resulting in an optical coherent amplification. This superposition yields an interference pattern containing a spectral modulation depending on the difference of optical path length between the reference and the different reflective interfaces of the sample. Optical Coherence Microscopy (OCM) is based on a Michelson interferometer to split a broadband light source into a reference and a sample arms (Fig. 1.4).

While two monochromatic waves as in Equation 1.7 will interfere for “ever”, i.e., even for macroscopic distances, polychromatic can only interfere within a given range called the coherence length l_c :

$$l_c = \frac{2 \ln 2}{n\pi} \frac{\lambda_0^2}{\Delta\lambda}, \quad (1.8)$$

where λ_0 is the central wavelength, $\Delta\lambda$ the full-width-at-half-maximum (FWHM) of the light source and n the index of refraction of the medium. The coherence length l_c determines the axial resolution in OCM whereas the lateral resolution depends on the wavelength and on the numerical aperture of the optical system, like in classical microscopy.

In OCM, the sample beam E_s is back-scattered by a sample whereas the reference beam E_r is reflected by a fixed “reference” mirror:

$$E_s(k, t) = S(k) \sum_{n=1}^N r_{s,n} e^{i(2kz_{s,n} + \omega t)} \quad \text{and} \quad E_r(k, t) = S(k) r_r e^{i(2kz_r + \omega t)} \quad (1.9)$$

where $r_{s,n}$ and $z_{s,n}$ are the reflectivity and the depth position of the n -th layer in the sample, r_r the reflectivity of the reference arm, z_r the distance to the reference mirror,

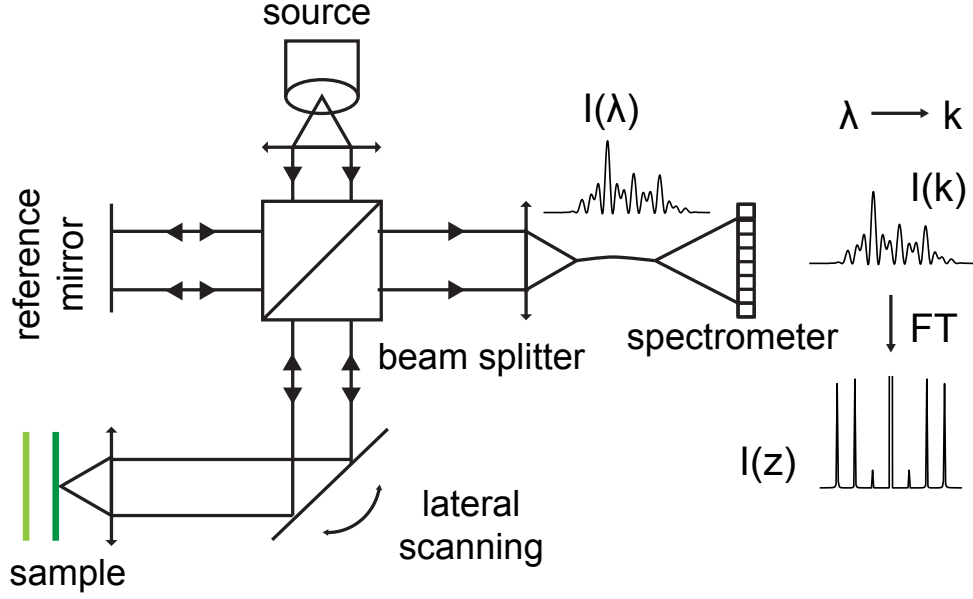


Figure 1.4: **Scheme of OCM principles.** The light source is split into two parts, the *reference* and the *sample* arm. The superposition of the two fields is detected by a spectrometer and mapped into the k -space. Finally, a Fourier transform (FT) allows for the reconstruction of the tomograms in the spatial domain, providing a view of the depth structure.

and $S(k)$ the field amplitude of the source. The two beams are recombined together and interfere constructively or destructively for the different wavenumbers k of the source (Equation 1.10). The correlation between the reference and sample field gives the cross-correlation term (CC). If the optical distance between two different layers in the sample is smaller than the coherence length (Equation 1.8), the light reflected from these two layers interferes and gives rise to the so-called autocorrelation (AC) contribution. This term is independent of the reference field. The DC term is a constant signal containing the back-reflected intensities of both the sample and the reference arm.

$$\begin{aligned}
 I(k) &= \langle (E_r(k, t) + E_s(k, t))(E_r(k, t) + E_s(k, t))^* \rangle \\
 &= |S(k)|^2 \left\{ \left(r_r^2 + \sum_{n=1}^N r_{s,n}^2 \right) + \sum_{n \neq m}^N r_{s,n} r_{s,m} \cos(2k(z_{s,n} - z_{s,m})) \right. \\
 &\quad \left. + \sum_{n=1}^N r_r r_{s,n} \cos(2k(z_r - z_{s,n})) \right\} \\
 &= I_{\text{DC}} + I_{\text{AC}} + I_{\text{CC}}
 \end{aligned} \tag{1.10}$$

The expression of Equation 1.10 represents the intensity per k -channel, where the interference of the light field $E(k, t)$ is averaged during the integration time of the

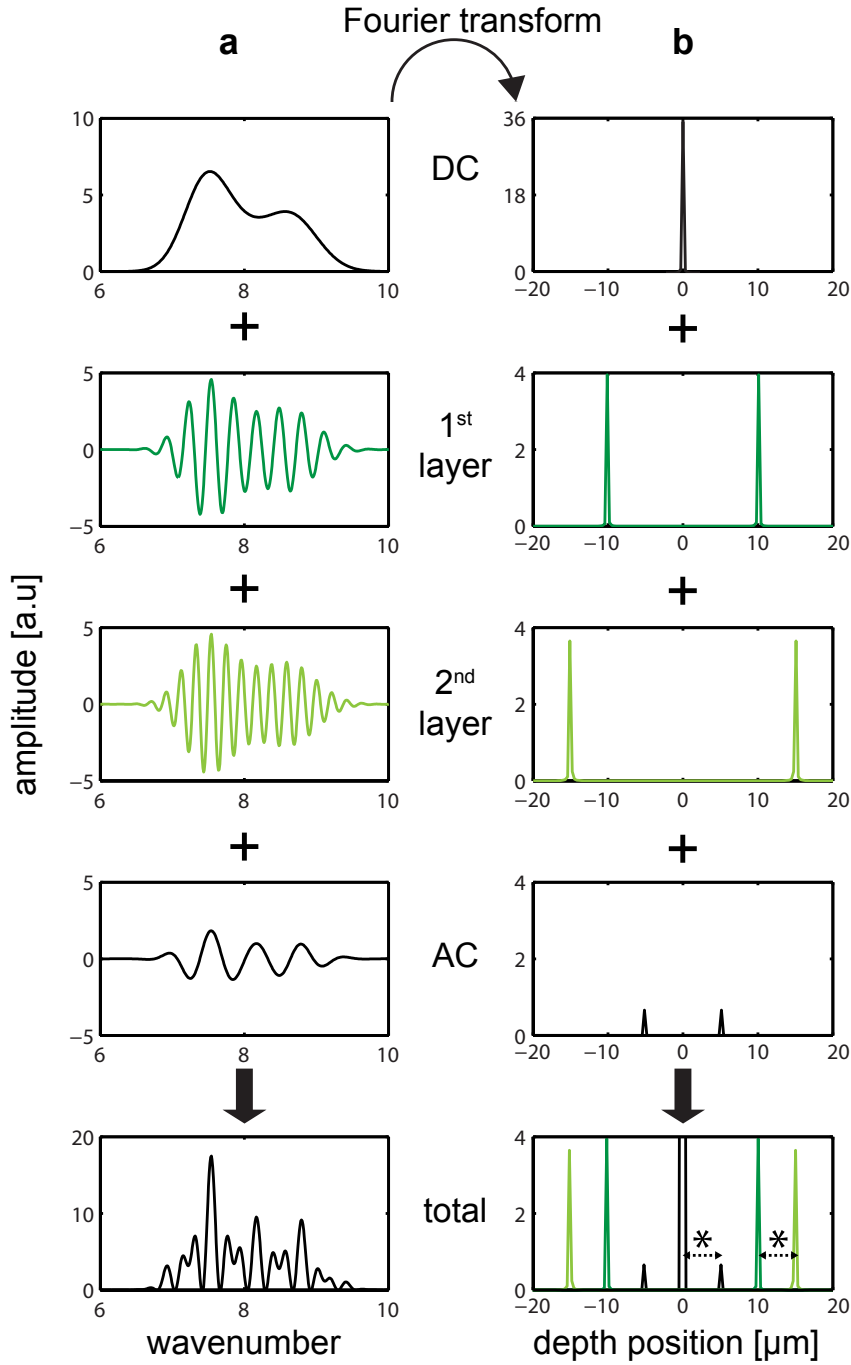


Figure 1.5: **Decomposition of the OCM signal in the case of a simple sample made of two layers like in Figure 1.4.** (a) The different components of the interference pattern in the wavenumber detected by a spectrometer. (b) The corresponding Fourier transform of each modulation. The stars indicate that the distance between the two peaks representing the two layers of the sample corresponds to the distance between the zero position and the autocorrelation peak.

detector according to Equation 1.4. Figure 1.5a shows the different contributions of a sample with N -reflective layers in the simplified case of $N = 2$ layers. The depth structure of the sample can be obtained by applying a Fourier transform along k :

$$\begin{aligned} \mathcal{F}\{I(k)\}(z) = \mathcal{F}\{|S(k)|^2\}(z) * & \underbrace{\left\{ \left(r_r^2 + \sum_{n=1}^N r_{s,n}^2 \right) \delta(z) \right\}}_{\text{DC}} \\ & + \underbrace{\sum_{n \neq m}^N r_{s,n} r_{s,m} \left(\delta(z - 2(z_{s,n} - z_{s,m})) + \delta(z + 2(z_{s,n} - z_{s,m})) \right)}_{\text{AC}} \\ & + \underbrace{\sum_{n=1}^N r_r r_{s,n} \left(\delta(z - 2(z_r - z_{s,n})) + \delta(z + 2(z_r - z_{s,n})) \right)}_{\text{CC}} \end{aligned} \quad (1.11)$$

where $\mathcal{F}\{I(k)\}(z)$ is the Fourier transform of $I(k)$ and $\delta(z)$ is the Dirac function³. Since $I(k)$ is a real function, $\mathcal{F}\{I(k)\}(z)$ is symmetric and only half of the information in Equation 1.11 is needed. To prevent an overlapping of these two symmetric parts, the reference arm has to be shorter than the sample arm. The first part in Equation 1.11 is the DC contribution centered around $z = 0$ and does not depend on k . The second term is the AC contribution caused by the interference between the different layers inside the sample. Normally, the AC contribution is weak and can be neglected. However for pancreas imaging, the islet scattering is so strong that this AC contribution appears. Finally, the CC term contains the sample information. Figure 1.5b shows the corresponding Fourier transform of the different signal contributions coming from a simple sample.

Classical OCT systems have both a Gaussian illumination and detection. Therefore, by increasing the lateral resolution (proportional to $\frac{1}{\text{NA}}$) the depth of field is decreased (proportional to $\frac{1}{\text{NA}^2}$). Leitgeb *et al.* [123] proposed an extended focus OCM (xfOCM) by using a Bessel beam illumination to maintain an almost uniform resolution over the whole depth of field despite a high NA.

OCT is an established technique in ophthalmology [124] which has driven OCT development. Other medical fields such as cardiology [125], dentistry [126] and dermatology [127] appeared with novel applications at a later time. xfOCM has been applied successfully to image murine islets of Langerhans [107] and to visualize cerebral amyloid- β plaques, a major neuropathological hallmark of Alzheimer's disease [128]. When weakly scattering tissues such as cells or culture tissues are observed with OCM, the weakly scattered signal of the sample is overwhelmed by the strong reflection of the sample holder. To overcome

³Using the definitions of the Fourier Transform: $F(z) = \mathcal{F}\{f(k)\}(z) = \int_{-\infty}^{+\infty} f(k) e^{-2\pi i z k} dk$, the Inverse Fourier Transform : $f(k) = \int_{-\infty}^{+\infty} F(z) e^{2\pi i z k} dz$, and the following properties: $\mathcal{F}\{\cos(2ks)\}(z) = \frac{1}{2}(\delta(z + s) + \delta(z - s))$ and $\mathcal{F}\{1\}(z) = \delta(z)$.

this limitation, Villiger *et al.* [129] implemented a dark field contrast for OCM (dfOCM). The basic configuration of dfOCM is similar to the xfOCM setup but a disc-shaped amplitude mask is added in the Fourier detection plane to block specular reflections from the sample slide.

1.6 Thesis objectives

The aim of this thesis is to establish OCM as a new tool to study pancreatic islets. In chapters 2 and 3, we implement the tools required to apply OCM to the study of pancreatic islets. Chapter 2 implements an algorithm for segmenting islets of Langerhans in OCM tomograms. This algorithm was further used to extract the distribution of islets of Langerhans and confirmed a similar distribution that the one obtained with Optical Projection Tomography (OPT). Based on this distribution, we developed *in silico* simulations to compare the performance of two metrics to detect deviations from a regular situation by imaging only a subpart of the pancreas: (1) a metric based on the integral β -cell volume and (2) a metric based on islet distribution. The statistical analysis confirmed the islets of Langerhans to be non-homogeneously distributed throughout the pancreas and the islet distribution to perform better than the integral β -cell volume criterion.

Structural information on the β -cell volume is an important parameter to measure since it is significantly reduced upon the clinical declaration of autoimmune diabetes. However, another important feature of pancreatic islets is their rich and dense vascularization. Since OCM can detect variations in index of refraction, it is also sensitive to moving scatters such as red blood cells. Chapter 3 establishes the potential of OCM to reveal the vascular network within the pancreas as well to assess blood flow velocity.

There is an intensive worldwide research to find specific tracers for β -cell in order to image the β -cell volume in a non-invasive manner in humans (Section 4.1). Since OCM allows for the label-free detection of islets of Langerhans, we demonstrate in Chapter 4 that OCM combined to a fluorescence channel can facilitate the initial screening for potential β -cell markers in animal models.

The label-free imaging of both the β -cell volume and vascularization makes OCM highly suitable for longitudinal studies in animal models. However, the possibility to perform longitudinal imaging in the pancreas is limited as it is almost impossible to follow the same islet at different points in time during the disease progression or treatments, i.e., several weeks. In order to study pathological effects at the level of a single islet, we adopt the anterior chamber of the eye (ACE) transplantation model in Chapter 5. Using this approach, we were able to follow the destruction of the β -cell volume and the associated reorganization of the vascularization of individual islets in a spontaneous animal model of T1DM. In this chapter, we also investigated the origin of the strong OCM signal for the pancreatic islet.

2 Label-free structural imaging of the pancreas

Visualization of pancreatic islets is essential to understand the onset and progression of diabetes, as well as to monitor putative beneficial treatments for conserving β -cell function or for promoting their neogenesis. Proof of principle of the structural imaging of both the pancreas and islets of Langerhans has been demonstrated by Villiger *et al.* [107]. However, no comparison with other imaging techniques in terms of estimation of the β -cell volume or distribution has been performed. In order to gain quantitative information from OCM measurements, a segmentation of the targeted structure is required. In this chapter, we describe a method for segmenting pancreatic islets in the pancreas using an active contours algorithm [130]. *In vivo* imaging with OCM is limited to a subpart of the pancreas. Therefore, it is important to determine which kind of information can be extracted based on a partial imaging of the pancreas. Based on *ex vivo* imaging data, we oppose the classical total β -cell volume to the islet-based distribution as a criterion to detect early deviation from a healthy state. Taking into account several hypotheses for the islets destruction during the progression of diabetes, we conclude on the performance and information gain of this alternative distribution-based criterion.

2.1 Journal article

Published in: Biomedical Optics Express, vol. 3, num. 6, p. 1365–1380, 2012.

Diabetes imaging—quantitative assessment of islets of Langerhans distribution in murine pancreas using extended-focus Optical Coherence Microscopy

Corinne Berclaz^{1,2}, Joan Goulley², Martin Villiger¹, Christophe Pache¹, Arno Bouwens¹, Erica Martin-Williams¹, Dimitri Van de Ville^{3,4}, Anthony C. Davison⁵, Anne Grapin-Botton², and Theo Lasser¹

¹Laboratoire d'Optique Biomédicale, École Polytechnique Fédérale de Lausanne, 1015 Lausanne, Switzerland; ²Swiss Institute for Experimental Cancer Research (ISREC), École Polytechnique Fédérale de Lausanne, 1015 Lausanne, Switzerland; ³Institute of Bioengineering, École Polytechnique Fédérale de Lausanne, 1015 Lausanne, Switzerland; ⁴Department of Radiology and Medical Informatics, University of Geneva, 1211 Geneva, Switzerland; ⁵Chair of Statistics, MATHAA, École Polytechnique Fédérale de Lausanne, 1015 Lausanne, Switzerland

Diabetes is characterized by hyperglycemia that can result from the loss of pancreatic insulin secreting β -cells in the islets of Langerhans. We analyzed *ex vivo* the entire gastric and duodenal lobes of a murine pancreas using extended-focus Optical Coherence Microscopy (xfOCM). To identify and quantify the islets of Langerhans observed in xfOCM tomograms we implemented an active contour algorithm based on the level set method. We show that xfOCM reveals a three-dimensional islet distribution consistent with Optical Projection Tomography, albeit with a higher resolution that also enables the detection of the smallest islets ($\leq 8000 \mu\text{m}^3$). Although this category of the smallest islets represents only a negligible volume compared to the total β -cell volume, a recent study suggests that these islets, located at the periphery, are the first to be destroyed when type I diabetes develops. Our results underline the capability of xfOCM to contribute to the understanding of the development of diabetes, especially when considering islet volume distribution instead of the total β -cell volume only.

2.1.1 Introduction

Diabetes is a major health problem that results from defective pancreatic β -cells in the islets of Langerhans, causing hyperglycemia [131]. T1DM is an autoimmune disease in which T-cells infiltrate the islets, leading to the destruction of the insulin producing β -cells [58]. T2DM diabetes, on the other hand, results from insulin resistance of the

peripheral tissues and from insufficient compensation by β -cells [70]. According to the World Health Organisation (August 2011), 346 million people worldwide suffer from diabetes. Although many aspects of the disease mechanism are understood, several open questions about the mechanisms involved in the progression of type I and II diabetes remain. Indeed, the difficulties faced in observing individual islets in patients or live mice significantly hinder research, and limit our ability to monitor putative beneficial treatments that should protect β -cells, improve their function or promote their proliferation during diabetes.

The main challenges for imaging islets of Langerhans are (1) the localization of the pancreas deep inside the abdominal cavity, (2) the very low density of these islets in the pancreas and (3) their diverse shapes and small size, which varies approximately from 30 to 300 μm in diameter. Current non invasive clinical imaging techniques such as PET, SPECT or MRI have insufficient resolution to detect individual islets and rely on a specific marker or contrast agent [132–134]. The development of a specific tracer for the β -cells is still a matter of research [96]. In order to detect individual islets optical resolution is needed. However, current *in vivo* optical techniques able to visualize β -cells *in situ* are limited in speed, penetration depth and require labeling [43, 103, 105, 106, 135]. Optical Coherence Tomography (OCT) [136–138] is a well-established imaging technique that provides cross-sectional views of biological tissue with micrometric resolution and has successfully been applied to a wide range of *in vivo* and *ex vivo* imaging in both clinical settings and small animal research. OCT has been applied to image fixed human pancreatic tissue [139] and the main pancreatic duct [140]. It has also been successfully employed to *ex vivo* distinguish between benign and malignant pancreatic cysts [141]. Recently, we have shown that extended-focus Optical Coherence Microscopy (xfOCM) [123] can image *in vivo* and *ex vivo* islets of Langerhans without labeling, with a spatial resolution close to cellular dimensions [107, 129]. xfOCM is based on OCT but allows to use higher numerical aperture objectives without reducing the depth of field. The increased depth of field is obtained by using an axicon in the sample arm, which generates a Bessel beam illumination. *In vivo* xfOCM pancreas imaging is possible by making a small incision through the flank of the anaesthetized mouse and by gently pulling out the duodenum encircling the pancreas. The anatomy of the pancreas allows only to access a subpart of the organ. *In vivo* xfOCM can image the surface volume of the pancreas down to 300 μm in depth. To compare xfOCM imaging of islets of Langerhans to other techniques, we dissected the pancreas of a 15-week-old NOD SCID gamma (Nonobese Diabetic Severe Combined Immunodeficiency) mouse. NOD SCID gamma mice are a well-known control for NOD mice, which spontaneously develop T1DM [83]. To have access to the islets of Langerhans located deeper in the pancreas, we cut the two lobes of the pancreas that are easily accessible *in vivo* into slices 250 μm thick. Segmentation and extraction of quantitative data from OCT images are challenging [142–144] but are required to facilitate and improve diagnosis. In order to obtain quantitative data, we implemented an automatic segmentation of islets of

Chapter 2. Label-free structural imaging of the pancreas

Langerhans in xfOCM tomograms based on an active contours algorithm. In this work, we performed automatic and quantitative islet imaging with xfOCM, revealing the three-dimensional size distribution of these islets. In addition, we assessed the possibility of measuring only a portion of the pancreas to extrapolate the total β -cell volume. Finally, we evaluated *in silico* the discrimination of healthy and pre-diabetic or diabetic animals based on two criteria: the total β -cell volume and the islet volume distribution.

2.1.2 Methods

xfOCM setup

The xfOCM instrument is based on a Mach-Zehnder interferometer (Fig. 2.1) [123]. A broadband light source (Ti:Sapphire laser, Femtolasers, Vienna, Austria; $\lambda_c = 800$ nm, $\Delta\lambda = 135$ nm) is coupled into a polarization maintaining single mode fiber and then collimated and split by beam splitter BS1 into reference and illumination fields. The illumination beam passes through an axicon (175° apex angle, Del Mar Photonics) which generates a Bessel-like field with an extended focus over a length of about 400 μm . The field behind the axicon is relayed by two telescopes into the intermediate image plane (IIP), and from there demagnified by the lens combination L_t , L_s (Zeiss Neofluar, 10x, NA 0.3), resulting in a lateral definition of 1.3 μm . The illumination beam is raster scanned over the sample, typically scanning a range of $0.5 \text{ mm} \times 1 \text{ mm}$. In order to increase the field of view, the objective can also be moved by two lateral motorized scanning axes (Thorlabs, model Z812B). The light backscattered by the sample is superimposed with the reference field by beamsplitter BS2. The optical signal is analyzed through a custom spectrometer consisting of a transmission grating (1200 lines/mm) and a line-scan camera (Atmel Aviva 2048 pixels, Stemmer Imaging, Pfäffikon, Switzerland) set to an integration time of 40 μs and working at an A-line rate of 20 kHz. The depth profile is reconstructed after background removal, k-mapping and Fourier analysis.

Specimen preparation

Anatomically, the pancreas can be segmented into three lobes [4, 145]: the splenic, gastric and duodenal lobes (Fig. 2.2a). After cervical dislocation, the duodenal and gastric lobes of a 15-week-old female NOD SCID gamma mouse (NOD.Cg-Prkdc^{scid} Il2rg^{tm1Wjl}/SzJ, Jackson Laboratory, Bar Harbor, USA) [146] were fixed for 90 min in a 10% (vol./vol.) paraformaldehyde solution in phosphate buffered saline (PBS) at room temperature, prior to an overnight incubation in a 30% (wt/vol.) sucrose solution in PBS at 4°C . The tissue was embedded in gelatin and frozen at -80°C . 34 sections of 250 μm thickness were prepared for xfOCM imaging.

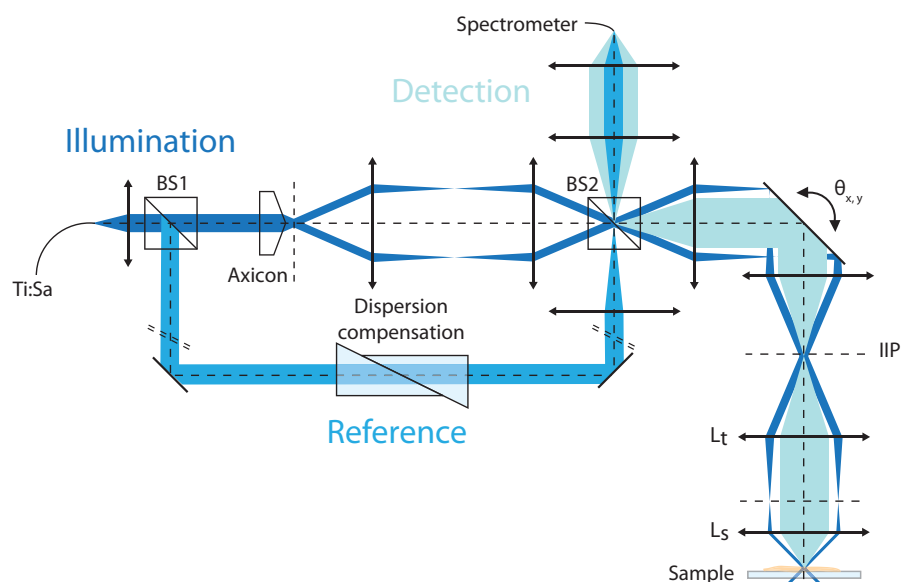


Figure 2.1: Schematic layout of the xfOCM setup.

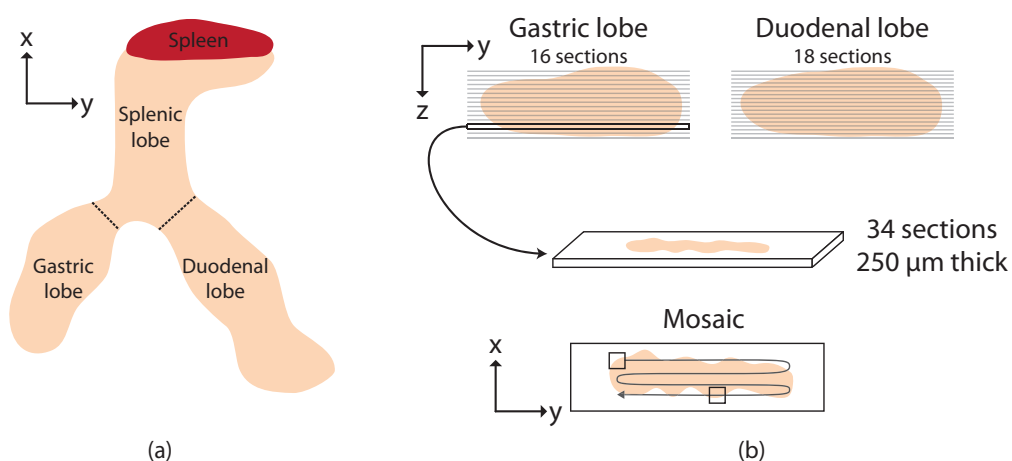


Figure 2.2: (a) Schematic representation of the three lobes of a pancreas. (b) Illustration of the experimental procedure.

Chapter 2. Label-free structural imaging of the pancreas

Three-dimensional image processing

Each of the 34 sections of the gastric and duodenal lobes were imaged individually. Due to the instrument design a field of view of only 0.5 mm x 1 mm is accessible. Therefore, we performed mosaics of each slice by a lateral displacement of the objective with motorized scanning axes (Fig. 2.2b). The three-dimensional imaging of the gastric and duodenal lobes resulted in more than $7 \cdot 10^8$ A-scans and represents approximately 5 Terabytes of data. The image processing was performed on the log scale, by taking $10 \cdot \log(|\text{FFT}(I(k))|^2)$, where FFT is the Fast Fourier Transform and $I(k)$ is the interferogram recorded on the spectrometer. The processing time was one week on a computational cluster composed of four 8-core 2.27 GHz nodes with 48 GB of RAM and 20 Gb/s Infiniband interconnect. Figure 2.3 shows an example of 8 adjacent en face views of a fixed murine pancreas at different depths. The largest islet in the center extends over more than 50 μm in depth which illustrates the importance of having a 3D segmentation. In order to assess and quantify the islet shape and the ratio of islet volume to tissue volume, two segmentation tasks were performed: first, tissue versus background, defining which fraction of the volume was filled by tissue; and, second, the islets within the detected tissue volume. The islet segmentation algorithm relies on active contours [130] with a level set method implementation [147]. The active contour model iteratively deforms an initial surface towards the boundary of the object by minimizing a function according to the properties of the image. The level set method allows tracking of the evolution of this surface using a surface of higher dimension. The initial conditions required for active contours are automatically defined from the histogram intensity of the image. The tissue segmentation relies on a cluster analysis which divides the image into two groups: tissue and background. A schematic overview of the main principles of these algorithms is illustrated in Figure 2.4.

Segmentation of the islets of Langerhans

Definition of the initial conditions: In xFOCM tomograms, islets of Langerhans are characterized by a higher scattering signal; as a result, the islets appear as dense clouds of points of high intensity (Fig. 2.5a). One major difficulty is caused by intensity variation along the depth of the sample, caused by sample attenuation, the variation of the focal volume, and the system intrinsic sensitivity roll-off. The signal-to-noise ratio (SNR) of deep islets is reduced compared to islets near the surface. In order to obtain an automatic detection procedure, an initialization of the Active Contours algorithm (AC-algorithm) is essential. The initial conditions algorithm uses an initial adaptive thresholding step (see flowchart in Fig. 2.5). The adaptive threshold is fixed by using the pixel intensity distribution of each xy -slice. The pixel intensities appear to be roughly normally distributed, but an exponential distribution can be fitted to those above a chosen threshold intensity. We chose a higher threshold at the 0.75 percentile of this exponential distribution, allowing us to distinguish pixels belonging to islets, and also some other structures (Fig. 2.5b). Then, we applied the morphological *closing* operator

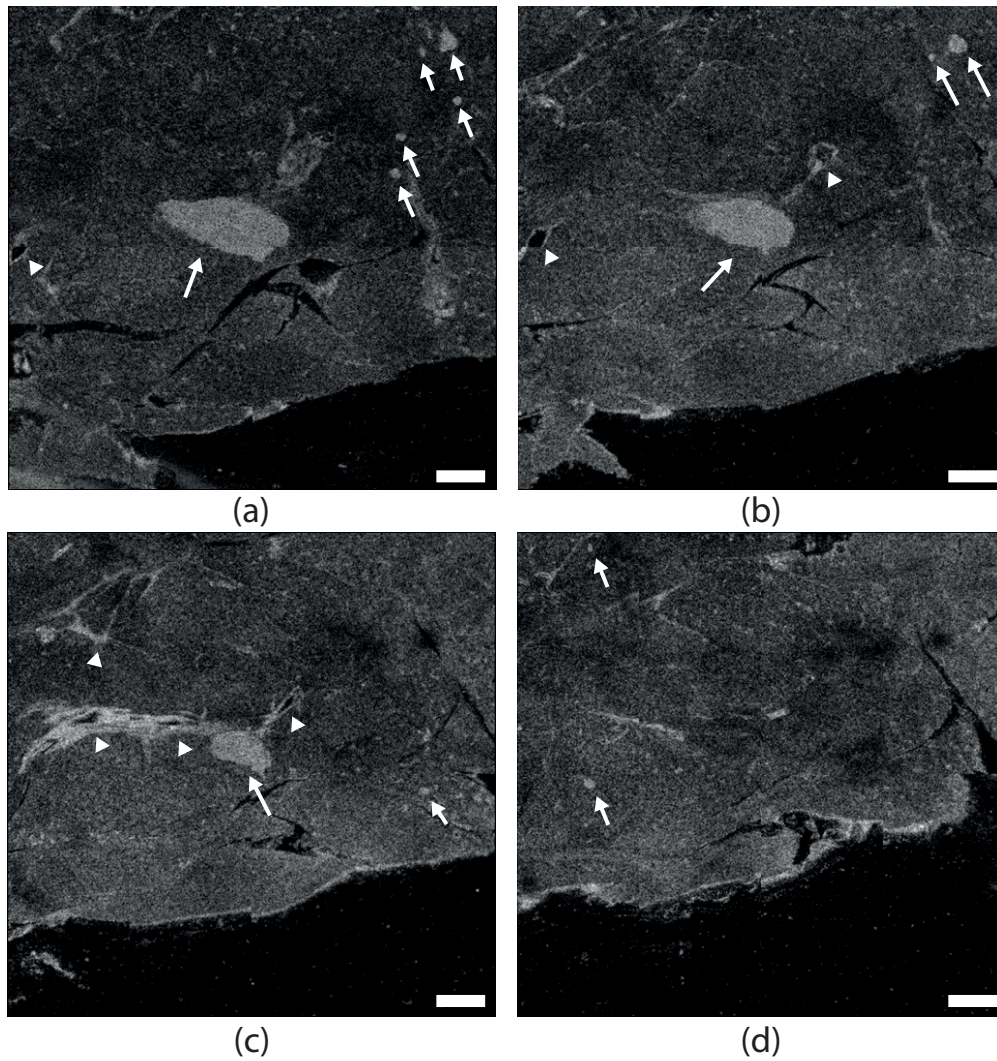


Figure 2.3: **Mosaic of 8 en-face views recorded on a pancreatic section.** Arrows indicate islets. In addition to the islets, one can clearly observe ducts (arrowhead) and lobe structures. Each picture shows the same area but at different depth positions. (a) 11 μm in depth, (b) 54 μm , (c) 97 μm , (d) 140 μm . Scale bar: 200 μm .

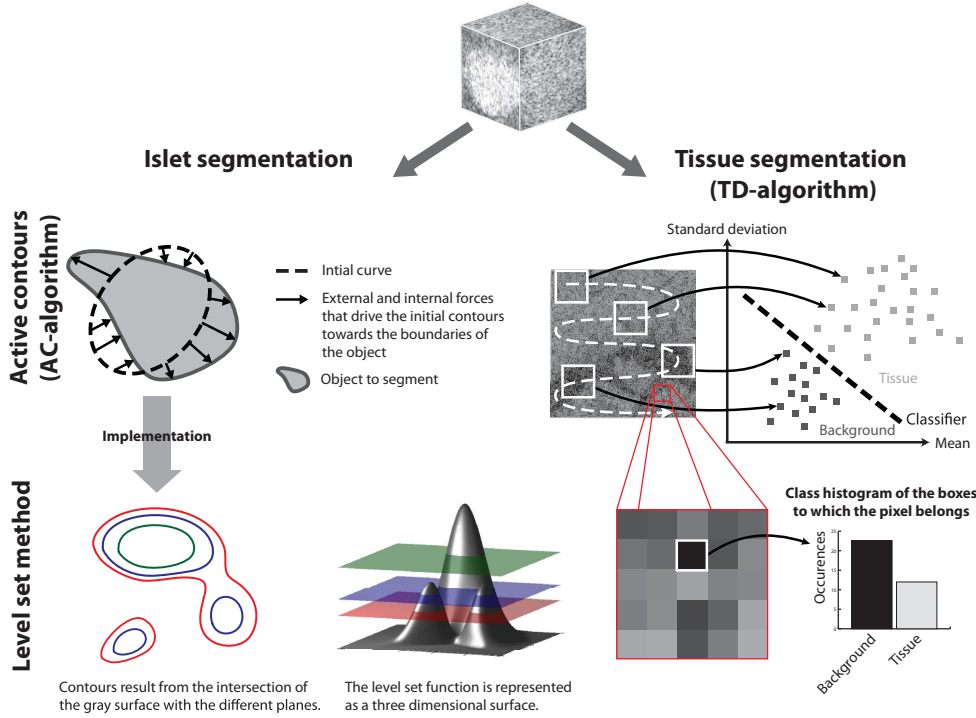


Figure 2.4: **Schematic 2D representation of the detection principles.** The segmentation of the islet is based on an active contours algorithm starting with an initial curve which evolves towards the boundaries of the islet. The active contours algorithm is implemented with the level set method. In this example, the intersection of the grey 3D surface with the plane in blue creates a 2D contour. By moving this plane up (in green) and down (in red), one can make the contour evolve, and even split or merge. The segmentation of the tissue is based on a cluster analysis.

to obtain filled structures (Fig. 2.5c). The Euclidean distance transform (i.e., each pixel is associated to its distance from the nearest border) of the resulting binary image is computed (Fig. 2.5d). Finally, each pixel corresponding to a regional maximum is used as the origin of a sphere of radius equal to the computed Euclidean distance of the pixel (Fig. 2.5e).

Active Contours and Sparse Field Algorithms: The AC-algorithm has several important features: (i) generation of smooth and continuous boundaries, (ii) robustness against intensity variations and speckle, and (iii) detection of objects with various shapes and sizes. The AC-algorithm searches for the boundary of an object by using a surface that deforms under external and internal forces (Fig. 2.4). External forces are computed based on image properties, whereas the internal forces depend only on the curve geometry. Usually, external forces drive the curve or the surface to the edge of the object, whereas the internal force tends to keep the curve or the surface smooth. Among the numerous variations of the AC-algorithm, we used the Chan-Vese algorithm [130] which proved to be the most efficient for this type of dataset. Each image was normalized according

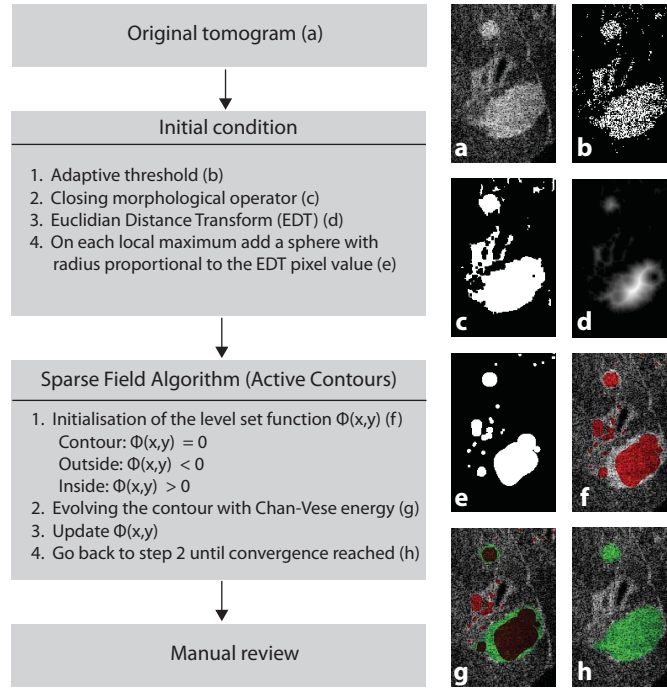


Figure 2.5: Flowchart and illustration of the different steps for islet segmentation.

to an adaptive threshold based on the histogram. In addition, saturated pixels or black pixels were discarded in order not to take artifacts or areas without tissue into account. One drawback of the AC-algorithm is the requirement for initial conditions. In our study, these were automatically defined based on the pixel intensity of the image, as explained above.

The evolving curve is represented using the level set method which captures n -dimensional surfaces as the intersection of a plane and a $(n + 1)$ -dimensional surface (Fig. 2.4). The three-dimensional surfaces are internally represented using the Sparse Field algorithm (SF-algorithm) [148], a particular efficient implementation of the level set method. Importantly, the level set method allows splitting or merging of the currently detected blobs as well as detection of several islets in parallel. In order to assess the convergence of the algorithm, we monitor the evolution of the detected volume. If the discrete derivative is less than 10^{-5} during 50 iterations, then the algorithm is stopped. The SF-code was written in Matlab and is partly based on the software package developed by J.G. Malcolm *et al.* [149, 150].

Tissue segmentation

Since one of our goal is to calculate the ratio of β -cell volume to pancreas volume, we need to compute the total volume of tissue. The general idea behind the tissue detection algorithm (TD-algorithm) presented hereafter is to classify each pixel into one of two

Chapter 2. Label-free structural imaging of the pancreas

categories: tissue or background. The TD-algorithm has two main steps (Fig. 2.4 and 2.6 provides a more detailed flowchart of the algorithm). First, a large dataset of spatial features is built by scanning the whole image with overlapping boxes of fixed size. To each box we associate one two-dimensional data point $p = (\mu, \sigma)$ where μ is the mean and σ is the standard deviation of all pixels within the box, without taking into account pixels with extreme values (i.e., black or saturated pixels). Boxes with extreme mean values are removed from the dataset before performing a cluster analysis using the **kmeans** function in Matlab. Finally, we use a linear classifier to find the line that separates the two clusters found by the **kmeans** function. The second step consists in attributing to each pixel a score that depends on the boxes the pixel belongs to; i.e., the number of boxes classified as tissue minus the number of boxes classified as background. Then, based on its score, each pixel is set as tissue or background.

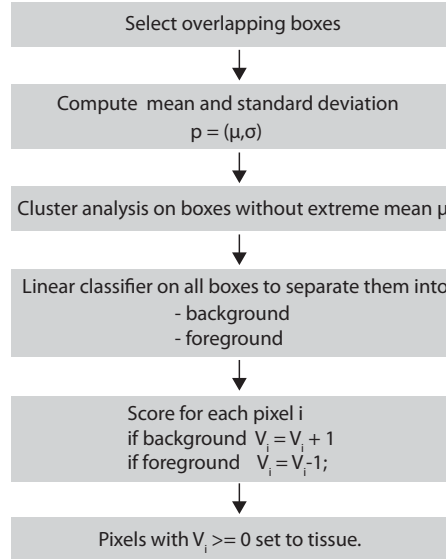


Figure 2.6: Flowchart of the TD-algorithm.

Validation

The efficiency of segmentation of the islets was determined using two criteria: the number of islets detected and the detection accuracy over a set of islets of different shapes and sizes and with various intensities. The number of islets detected by the algorithm is validated against the observations of a trained user. The detection accuracy is calculated by comparing the results with the best detection ever obtained for each islet and defined as correct by a trained user; this notion of “best detection” is subtle and subjective, as it is difficult to visually evaluate the quality of detection in three dimensions. Indeed, two detections of the same islet that are both visually accurate could differ significantly after quantification in terms of volume. In such cases and for referencing, we systematically chose the detection with the highest volume defined by a trained user as correct. By

using these criteria, we obtained 90% of islets detected with a relative mean square error for the volume of the islets of 30%. The error on the volume of each islet depends on the size category, with a larger error for the small islets. A major effort was dedicated to the detection and handling of false positives, i.e., pancreas structures designated by the algorithm as islets, but rejected by a trained user (Fig. 2.7). Due to the small number of islets in a pancreas, these “false positives” have been addressed individually in order to minimize false detection. Although this step is time-consuming, it is much faster and, most importantly, much less error-prone than a manual search through thousands of tomograms. In addition, it allows the user to restart the detection with a better manual initial condition if an islet is missed or not completely detected.

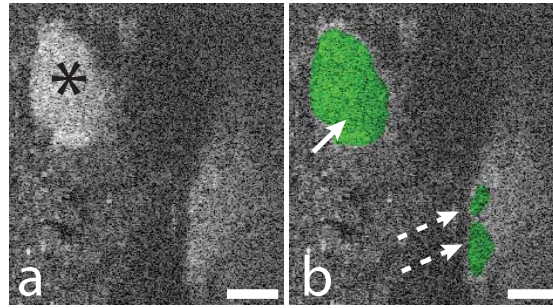


Figure 2.7: The picture in **(a)** shows two areas with a higher intensity. By using a three dimensional view, only the area marked by a (*) is defined as an islet by a trained user. However, the result of the algorithm, shown in **(b)**, finds three blobs. The solid arrow shows the correct detection of an islet whereas the dashed arrows indicate false positives. Scale bar: 100 μm .

2.1.3 Results

Assessing β -cell volume

The development of T1DM is closely related to the total β -cell volume (or calculated β -cell mass). Assessing the β -cell volume is therefore crucial to understanding and monitoring diabetes onset. However, *in vivo* xFOCM can only image a subvolume of the pancreas due to its anatomy and localization into the abdominal cavity. Therefore, we asked ourselves whether we can extrapolate the total β -cell volume by imaging only a part of the pancreas. We answered this question by comparing the β -cell volume extrapolated from a part of our data with the total β -cell volume obtained from the complete *ex vivo* measurements. Following an approach called bootstrapping in statistics [151], we re-sampled the data for varying sample sizes. For each sample size, we re-constructed 2500 random samples and calculated the resulting percentage of β -cell volume per pancreas volume. Figure 2.8 shows the variability in the error obtained by comparing the percentage of β -cell volume per pancreas volume extrapolated from the small sample and the true value from the comprehensive experimental measurement. This procedure shows that we cannot reliably

Chapter 2. Label-free structural imaging of the pancreas

extrapolate the β -cell volume based on small samples of the pancreas. Indeed, even for 50% of the measured tissue, the relative error is still around 30%. This result outlines the difficulty in determining, at least on a mouse model, the total β -cell volume.

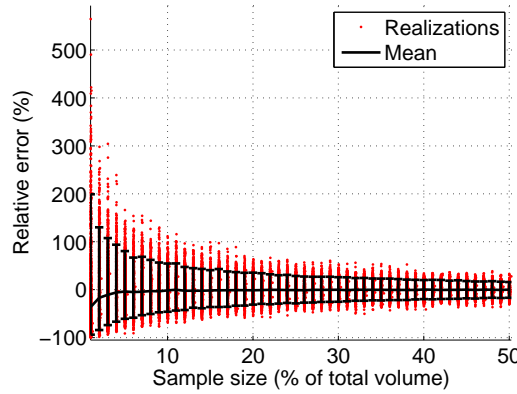


Figure 2.8: **Relative error for the extrapolated percentage of β -cell volume per pancreas volume based on different sample sizes.** Each red circle represents the results of an individual trial. The black near-horizontal line represents the median and the vertical black error bars show the 5th and 95th percentile. Even if the median relative error is below 5% for 5% of the total volume, the spreading error is still of 57% for 25% of the tissue.

3D islet distribution in the duodenal and gastric lobes

The resolution of xFOCM offers the possibility to determine the whole islet volume distribution instead of looking at an integral value such as the total β -cell volume. According to Bock *et al.*, the mean β -cell volume is $1280 \mu\text{m}^3$, which corresponds roughly to 150 voxels [152]. Therefore, objects smaller than the volume of a β -cell are considered below threshold and have been automatically discarded. After a manual review of the output of the algorithm, we detected 924 islets in the duodenal and gastric lobes of a 15-week-old NOD SCID gamma mouse. A histogram with logarithmic binning shows that the smallest islets ($\leq 8000 \mu\text{m}^3$) are the most common, and account for 20% of the total number of islets (Fig. 2.9b). However, this category contributes only 3% of the total β -cell volume (Fig. 2.9c), whereas the largest islets ($\geq 4 \times 10^6 \mu\text{m}^3$) contribute more than 45% of the β -cell volume and represent 4% of the total islet number. The important contribution of the small islets can, therefore, only be discovered by plotting the islet volume distribution and would be undetectable in the integral β -cell volume. The largest islet found has a volume of $9 \times 10^6 \mu\text{m}^3$. The total volume of β -cells corresponds to 0.26 mm^3 , which yields a percentage of β -cell volume per pancreas volume of 0.175%. The islet volume distribution seemed to follow a power law. We verified this hypothesis by fitting different discrete power law distributions (Yule–Simon, Zeta, Zipf and Zipf–Mandelbrot) to the islet volume data. After goodness

of fit testing [153], only the Zipf–Mandelbrot distribution appears to fit the data at this level of discretisation (Fig. 2.9a):

$$f(k; N, q, s) = \frac{(k + q)^{-s}}{\sum_{i=1}^N (i + q)^{-s}}, \quad k = 1, \dots, N, \quad (2.1)$$

with $N = 600$, and estimated parameters $q = 0.45$ and $s = 1.55$ (Fig. 2.9a).

The principle of goodness of fit testing is to compare the empirical distance (i.e., the distance between the experimental data and their fitted distribution) with an artificial distance (i.e., the distance between artificial data generated according to the hypothesized distribution and their fitted distribution). When the number of bins is large (> 500), the discrete chi-square distance becomes computationally intractable. In this case, because the number of bins is sufficiently large, we used the continuous Kolmogorov–Smirnov distance. The p-value corresponds to the proportion of trials where the artificial distance exceeds the empirical one, and in this case is 0.17, estimated from 2500 simulated artificial datasets, so we conclude that our data are close to following a Zipf–Mandelbrot law, at least at this discretization.

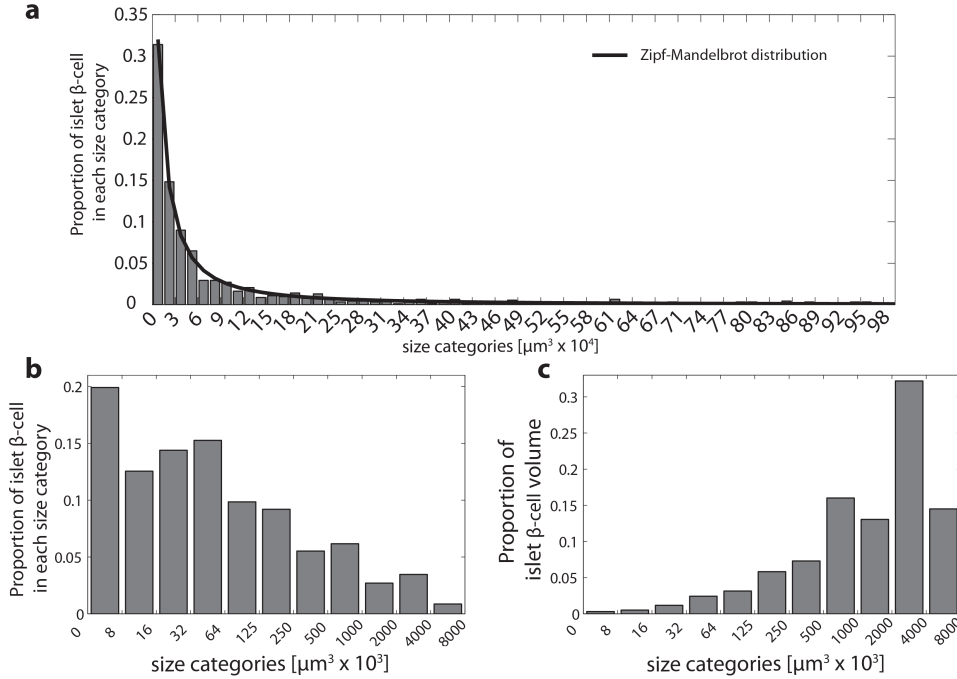


Figure 2.9: Histogram of the islet volumes in the gastric and duodenal lobes of a 15-week-old female NOD SCID gamma mouse. The islet volume distribution follows a Zipf–Mandelbrot distribution (a). A logarithmic visualization of the size categories shows that the most common islets are those of volume less than $8000 \mu\text{m}^3$, followed by those between 32000 and $64000 \mu\text{m}^3$ (b). The proportion of the islet volume of each size category to the total β -cell volume is inversely related to their occurrences, with the smallest categories of $8000 \mu\text{m}^3$ contributing only 3% (c).

Different distributions between the duodenal and the gastric lobe

Interestingly, we noticed that the distribution of islet volumes from the gastric lobe is different from that in the duodenal lobe: we found 315 islets in the gastric lobe and 609 islets in the duodenal lobe, even though the total β -cell volumes are comparable (0.129 mm^3 and 0.132 mm^3 respectively). The total tissue volumes of the gastric and the duodenal lobes were 70.79 mm^3 and 78.47 mm^3 . Both islet distributions follow a Zipf–Mandelbrot law (Fig. 2.10). Thus the duodenal lobe contains more small islets than the gastric lobe.

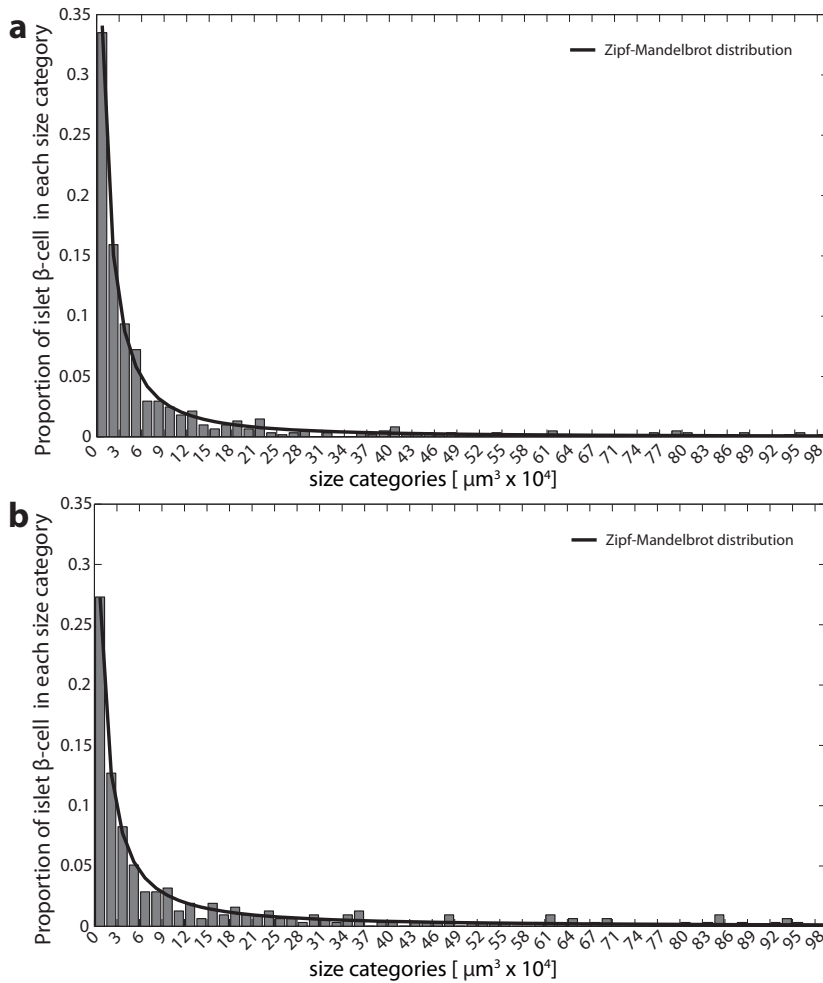


Figure 2.10: **(a)** Histogram distribution of the duodenal lobe and **(b)** of the gastric lobe. The Zipf-Mandelbrot parameters are $N = 600$, $q = 0.56$ and $s = 1.65$ for the duodenal lobe and $N = 600$, $q = 0.38$ and $s = 1.41$ for the gastric lobe, with a p-value of 0.11 and 0.7, respectively.

***In silico* discrimination of healthy and sick animals**

We cannot extrapolate the total β -cell volume of an animal by analyzing only a subvolume of the pancreas. Due to the anatomical configuration around the pancreas, only a small portion is accessible *in vivo*. Therefore, extrapolation of the total β -cell volume in a living animal is almost impossible. However, this might not preclude the possibility to discriminate between healthy, pre-diabetic or diabetic mice (hereafter referred as *sick* mice). A full study is well beyond the scope of this project, given the variability across the different animals, which would demand a large cohort of animals. Therefore, we propose an *in silico* approach consisting of generating simulated islet datasets of a sick mouse, and detecting deviation from a healthy situation based only on a subvolume. To date, not much is known about the dynamics leading to the apoptosis of β -cells in T1DM. The work of Alanentalo *et al.* suggests that the smallest islets are the first to disappear in NOD mice and that the T-cells infiltration does not seem homogenous throughout the whole organ [31]. One may hypothesize that at first only the smallest islets disappear or all islets are attacked at the same rate, therefore leading to the earlier destruction of the smallest islets. However, the reality might involve more randomness and the islets might be attacked at different rates. Therefore, we propose for our *in silico* analysis three scenarios in an attempt to simulate this degenerative process: (A) all islets smaller than a certain size are removed from the dataset, (B) all islets are shrunk by a certain percentage in volume, and (C) a stochastic approach in which islets are attacked with a predetermined probability. The latter approach involves two parameters: (i) the probability that an islet is attacked, and (ii) the conditional probability that each individual cell is destroyed given that the islet is attacked. By applying these three scenarios to the healthy experimental data, we obtain a set of simulated datasets of sick mice. Further on we asked the question, which percentage of the tissue should be analyzed to discriminate a deviation from a healthy situation. For this approach, we can apply to these datasets the same bootstrapping method as described previously. To this end, we selected small samples of variable volume at random locations within the tissue until we obtain the desired volume. For this analysis, we can try to use either the β -cell volume or the islet volume distribution as a criterion to detect a deviation from a healthy situation. The β -cell volume would indicate an onset of the disease if it is smaller than a given threshold. Importantly, this threshold must account for the intrinsic variability of the underlying dataset. In our case, the threshold is fixed to the 0.1 percentile of the variability of the percentage of β -cell volume per pancreas volume obtained by bootstrapping in Figure 2.8, thereby leading to a 10% tolerance of false positives. For the islet volume distribution criterion, we compared re-sampled distributions from the sick and healthy datasets. To achieve that, we apply the Kolmogorov-Smirnov non-parametric statistical test. Figure 2.11 and Figure 2.12 show the success rate to detect a deviation, which is indicated by the colorbar. In all scenarios, the ability to detect a deviation based on the islet volume distribution performs far better than the integral criterion based on the total β -cell volume. In scenario A, if all islets smaller than 20'000 μm^3

Chapter 2. Label-free structural imaging of the pancreas

are destroyed, then the proportion of successful detection is 30% even for small sample sizes of 1.5% of the total measured volume. If we double this volume to 6% we can reach 60% of successful detection of diabetes onset. In scenario B, the difference between the two criteria is less pronounced; yet, the islet volume distribution performs better. The results become conclusive only for high percentages of reduction. Scenario C exhibits less favorable results, but it illustrates again the superiority of a diagnostic approach based on distributions rather than solely the total β -cell volume. However, it becomes reliable only for high probabilities of an islet being attacked and that individual β -cell are destroyed. Overall, this *in silico* study indicates an alternative way to determine diabetes onset and evolution. A distribution based criterion in contrast to the integral β -cell volume criterion seems to be a more sensitive diagnosis for the onset of T1DM.

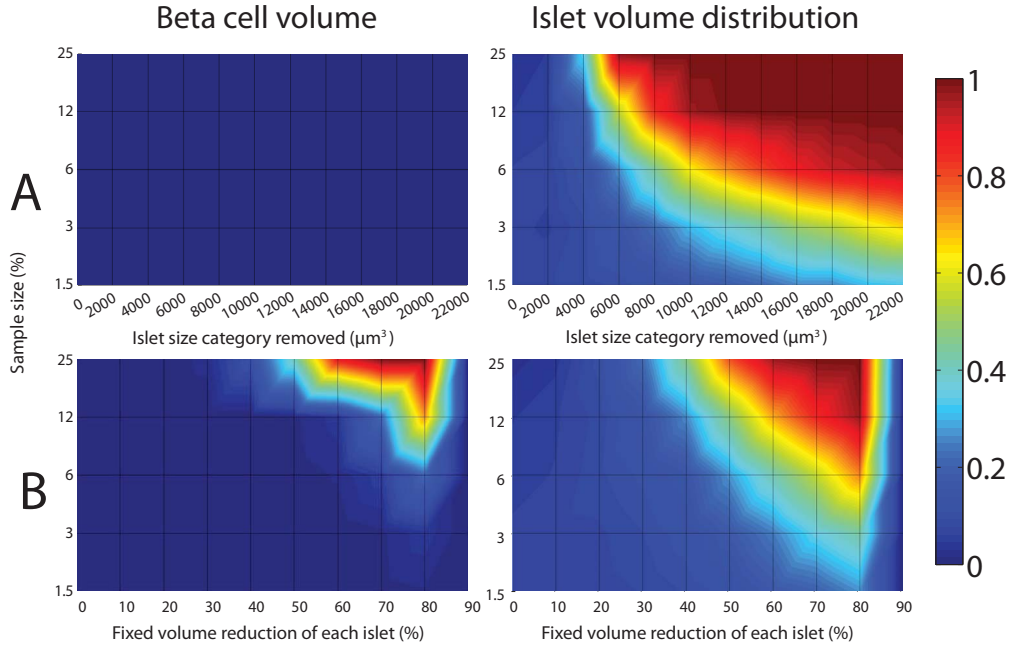


Figure 2.11: Success rate to detect a deviation between the healthy and simulated sick datasets for scenarios A and B. The colorbar indicates the proportion of successful detection over 2500 trials.

2.1.4 Discussion

In this study, we described the complete three-dimensional distribution of islets of Langerhans in the duodenal and gastric lobes of a 15-week-old female NOD SCID gamma mouse. An alternative estimation of the islet distribution in a pancreas was done *ex vivo* using Optical Projection Tomography (OPT) [105]. Although we analyzed only the duodenal and gastric lobes of the pancreas with xfOCM, the islet distribution is similar to the distribution obtained with OPT for an entire pancreas. However, xfOCM is capable of resolving an islet size category of less than $8000 \mu\text{m}^3$ ($\sim 6 - 10$ cells), which is not

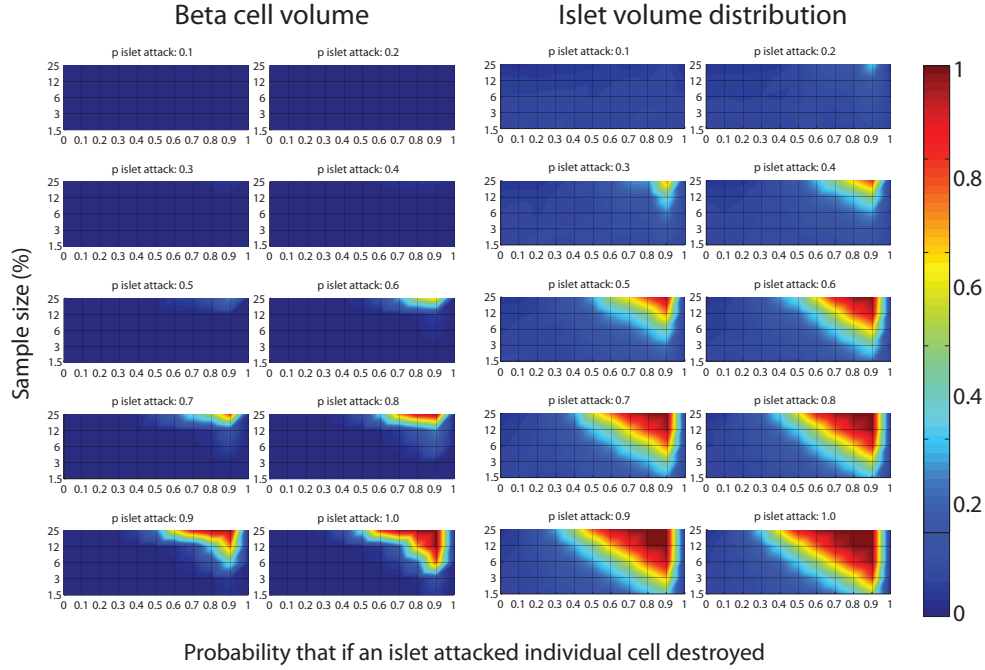


Figure 2.12: **Success rate for discrimination between the healthy and simulated sick datasets for scenario C.** Each diagram represents a probability (p) of an islet being attacked. The x-axis shows the probabilities that if an islet is attacked the individual cell will be destroyed. The y-axis always represents the different sample size used to do the test. The colorbar indicates the proportion of successful detection over 2500 trials.

yet detectable with OPT [105]. The same authors recently suggested that the smallest and peripherally located islets are the first to be destroyed during infiltration in T1DM in NOD mice [31]. Therefore, even if this small size category represents only 3% of the total β -cell volume, the ability to resolve these islets might be crucial to detecting the early onset of T1DM. Since *in vivo* xFOCM is limited by a penetration depth of about 300 μm and by anatomical constraints to a small portion of the total pancreas, it would be interesting to determine the islet volume distribution in this accessible region only. However, due to the location and the morphology of the pancreas and due to the protocol of our experiment it is difficult to determine the distance of an islet to the organ's surface. A potential solution would be to image directly the entire organ in three dimensions, like in OPT. The β -cell volume per pancreas volume of 0.175% detected in our analysis is in the same range, but slightly lower than the percentages reported in the literature [49, 154–157], although some authors report a higher β -cell volume [4, 158, 159]. It should be noted that there are significant variations between strains and across species [154]. In addition, the β -cell mass is most often given in mg and rarely with the corresponding pancreas weight or as a percentage of β -cell area per pancreas area. Finally, the majority of these imaging techniques relies on partial measurement of the pancreas and are done in two dimensions. Therefore, this lower

Chapter 2. Label-free structural imaging of the pancreas

value can be attributed to the difference between the strains and/or the use of different imaging techniques, in particular the fact that our method is three-dimensional and applied to the duodenal and gastric lobes only. Our statistical analysis reveals a huge variability on the extrapolated percentage β -cell volume which confirms the fact that the islets of Langerhans are non-homogeneously distributed throughout the pancreas [105]. This result shows that measurements based on a small part of the pancreas cannot be used to extrapolate reliably the total β -cell volume. This outcome does not confirm the statements of Chintinne *et al.*. They claim that 1.2% of the adult rat pancreas being systematically sampled is sufficient to obtain predictions of the β -cell mass with an error below 10% [160]. Besides the fact that the study is not based on the same species, this discrepancy might be attributed to a different experimental approach. First, they perform imaging only in two dimensions (area) whereas we have fully three-dimensional data. Second, their ground truth is the average β -cell mass measured on 2% of the pancreas of 6 rats whereas we obtain it from the complete dataset of one mouse. In this work, the experimental islet volumes follow a Zipf-Mandelbrot distribution. However, more mice would be required to conclude that a healthy islet volume distribution can be associated to a Zipf-Mandelbrot distribution. Yet, in this study we used a NOD SCID gamma mouse, which is a control for NOD mice, a reference strain for T1DM. Therefore we can safely assume that our islet volume distribution is indeed a reference distribution for healthy animals. Finally, the *in silico* analysis strongly suggests the superiority of islet volume distribution compared to the β -cell volume as a criterion for disease progression and detection. The islet distribution criterion performs the best in the case where small islets are removed from the dataset (scenario A in Fig. 2.11). The success rates become acceptable upon removal of all islets smaller than $16'000 \mu\text{m}^3$ ($\sim 25 \mu\text{m}$ in diameter). However, when Analentalo *et al.* suggests that the small islets are the first to disappear, they are referring to islet sizes below $1'000'000 \mu\text{m}^3$ ($\sim 100 \mu\text{m}$ in diameter). In our case, if we remove islets smaller than $122'000 \mu\text{m}^3$ ($\sim 50 \mu\text{m}$ in diameter) we can reach a success rate of detection of 56% for only 1.5% of the total tissue imaged. In the two other scenarios (see Section 2.1.3), the islet volume distribution criterion still performs better than the total β -cell volume, but it is reliable only for more extreme conditions. These results underline the importance of imaging techniques that can resolve individual islets, compared to clinical imaging techniques that detect only a global signal. Although optical techniques are mainly limited to research, they provide a realm of information for a deeper understanding of T1DM in well-established mouse models. Nevertheless, even if diabetic mouse models are well-established, differences in the islet architecture between humans and mice should not be forgotten [5, 7].

2.1.5 Conclusion

We show that xfOCM coupled with an efficient segmentation algorithm is a label-free imaging method to quantify islets of Langerhans over their whole size range ($\leq 8000 - 9 \times 10^6 \mu\text{m}^3$). Their sizes follow a Zipf-Mandelbrot distribution, which suggests a different

way of monitoring T1DM. The conclusions of our statistical analysis are two-fold: first, it shows that we cannot extrapolate quantitative predictions of the total β -cell volume based on small, randomly sampled sets of measurements. Second, criterion based on the islet volume distribution shows better potential than a criterion based on the total β -cell volume alone to detect a deviation from a healthy situation. xfOCM results are consistent with the literature and have sufficient resolution to enable the visualization of the smallest islets, which is crucial for future optical diagnosis techniques of T1DM as well as for the development and optimization of future treatments.

3 Label-free functional imaging of the pancreas

Extended Optical Coherence Microscopy (xfOCM) was previously applied for the detection of islet of Langerhans both *in vivo* and *ex vivo* [107, 161]. Another general application of OCT is blood flow imaging, which can be divided in two parts: (1) angiography and (2) quantitative assessment of the blood flow. Both approaches use the red blood cells as moving scatterers and analyze successive measurements acquired at the same spatial position, but at different time points/delays. OCM and OCT have already been applied to image vascularization in various tissues including the retina [162], the brain [163] and the skin [164]. Blood flow assessments have been mainly applied to the retina [165] and to the brain [166, 167]. In this chapter, we apply xfOCM to image and quantify the rich islet vascularization and to extract blood flow inside the pancreas. The work described hereafter has been done in collaboration with Daniel Szlag [168].

3.1 Introduction

Previous studies have shown the importance of the vascularization in pancreatic islets. For instance, there are indications that a modification of the vascularization is associated with the early onset of both T1DM and T2DM [47, 121, 169, 170]. In particular, islet grafting has become an alternative treatment for selected diabetic patients despite the fact that very few diabetic patient are insulin independent 5 years after transplantation [67]. Nevertheless, even if insulin independence is not achieved, islet grafts allow for a decrease of the daily insulin dose and the frequency of hypoglycemia episodes. One of the reasons of graft failures is a poor revascularization and perfusion [27, 171]. Therefore, monitoring of islet engraftments is important to evaluate islet revascularization in different graft sites [172–174]. In addition, there are indications that the glucose intolerance observed in aged mice is not due to β -cell defects, but to a vascular impairment [175]. The deep localization of islets inside the pancreas in the abdominal cavity and their distribution throughout the organ render imaging of their vascularization challenging. During the last decades, visualization with immunohistochemistry on whole mount preparation [176, 177],

electron microscopy [33] and methacrylate corrosion casting [32, 178] yielded anatomical information on vascularization, but these *ex vivo* techniques have been solely restricted to structural information. Microsphere-based techniques go beyond this limitation by extracting functional blood flow information in the exocrine and endocrine pancreas [28, 29, 34]. However, they require sacrificing the animals at different points in time and therefore cannot assess the full blood flow dynamics and alterations during diabetes progression. *In vivo* imaging of the vascularization of islets has been achieved through intravital fluorescent microscopy in the native pancreas [38, 43, 169], in grafted islets in the anterior chamber of the eye [108, 109, 111, 113, 114], or in striated muscle by using a dorsal skin-fold window [39, 118, 119, 179]. However, fluorescent microscopy requires both genetically modified mice expressing a fluorescent protein to detect islets and the injection of labelled dextran or labelled red blood cells to image the vascularization. Moreover, three-dimensional islet imaging requires optical depth sectioning, which implies a trade-off between axial and time resolution and prevents a complete characterization of functional parameters. Therefore, there is a strong need for an imaging technique that offers a good spatial resolution, high sensitivity, sufficient penetration depth, and fast image acquisition rate to study the vascularization and the blood flow of islets of Langerhans in a longitudinal and non-invasive fashion.

3.2 Research design and methods

A description of the xfOCM instrument used in this chapter can be found in Section 5.2.5.

Animals

Adult ICR female mice were purchased from Harlan. Prior to imaging, they were anesthetized by an intraperitoneal injection of a 10 $\mu\text{l/g}$ of body weight of a solution containing 9 mg/ml Ketazol and 1.45 mg/ml Xylazol. For imaging sessions longer than 30 minutes, the anesthesia was prolonged with 1% isoflurane oxygen mixture. *In vivo* xfOCM pancreas imaging was performed by making a small incision through the flank of the anesthetized mouse and by pulling out the duodenum encircling the pancreas (Fig. 3.1). A small pillar was used for stabilizing the duodenum during imaging acquisition. Both the pancreas and the duodenum were frequently humidified with 0.9% NaCl. The mouse was placed on a heating stage during the whole imaging session. All animal procedures were approved by and performed according to the guidelines of the local authorities and Swiss animal protection law.

Functional OCM

Visualization of the vascular network is based on motion contrast between static structures and moving red blood cells whereas, for blood velocity, the phase difference $\Delta\phi$ or the

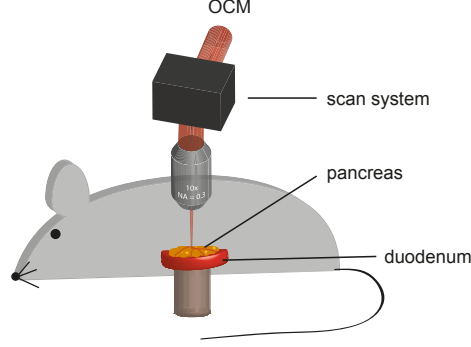


Figure 3.1: Schematic representation of *in vivo* pancreas imaging with xfOCM, including the laparotomy.

Doppler frequency f_D is extracted to compute the velocity v :

$$v = \frac{\lambda_0}{2n} f_D = \frac{\lambda_0 \Delta \phi}{4\pi n \Delta t} \quad (3.1)$$

where Δt is the time delay between successive acquisitions and n is the index of refraction of the tissue ($n = 1.33$).

Vascular network

A Doppler shift induces a frequency shift, which corresponds to a rotation of the electric field vector in the complex plane. Therefore, we need to estimate this variation to assess the red blood cells velocity. One approach to measure this rotation is to look at the phase variance by computing the circular variance \bar{v} [180]¹:

$$\begin{aligned} \bar{p} &= \frac{A_1 A_2^*}{|A_1 A_2^*|} \\ \bar{v} &= 1 - |\bar{p}| \end{aligned} \quad (3.2)$$

such that $0 \leq \bar{v} \leq 1$, where A_1 and A_2 represents two A-scans after a Fourier transform taken at the same position, but separated by a time delay Δt . This method uses a specific scanning protocol where each line (B-scan) is scanned several times [166] (Fig. 3.2). The phase variance method detects all red blood cells moving sufficiently fast, i.e., such that their position has changed significantly between two successive acquisitions. Therefore, this variance-based method shows all vessels and capillaries whose blood speed is higher than a velocity threshold given by the acquisition speed, but it provides no quantitative

¹The circular variance measures the angle variation about the mean direction of the vectors in the complex plane. The circular variance is therefore related to the mean resultant length of these vectors called \bar{p} .

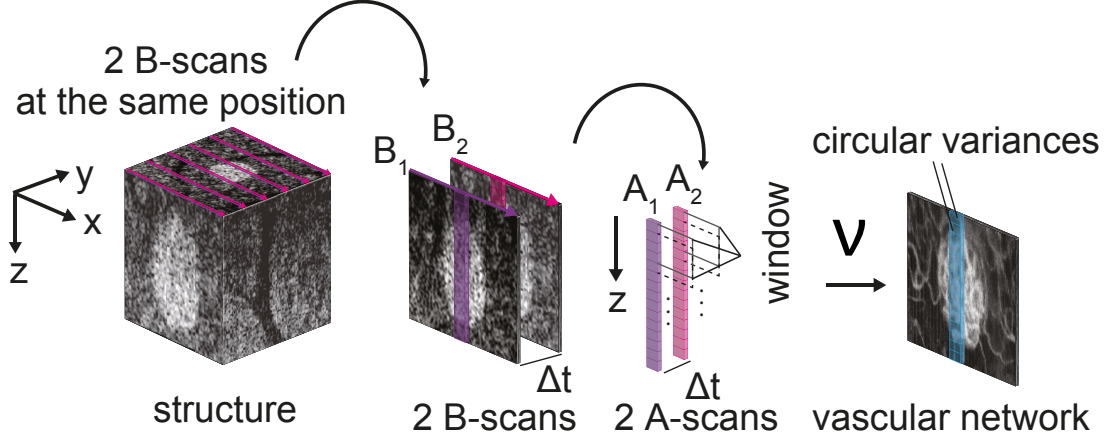


Figure 3.2: **Schematic representation of the data processing to extract vascularization.** An A-scan is a depth-profile. By a lateral scanning of several A-scans, a B-scan (also called tomogram) is created. Taking several B-scans in the other dimension allows the acquisition of a full volume also called a C-scan. In the z -direction, a moving average (window) is applied to improve the contrast. When more than two B-scans are taken, the circular variances obtained at a given pixel are averaged.

information about the actual velocities. To improve the contrast, the circular variance can be averaged over a moving window in the axial direction. However, the regions where there is no structure give rise to random circular variance. To remove these undesired values, the circular variance is multiplied by the structural image. Alternatively, as described in Section 5.2.6 (§*Temporal Derivative*), the weighing can be replaced by the temporal derivative [166]. For our measurements, each A-scan was computed using an axial window of 8 pixels and 6-8 B-scans were taken to perform averaging. The acquisition frequency range spans from 20 to 50 kHz, depending on the pancreas stabilization achieved. The vascular density can then be computed as:

$$\text{vascular density} = \frac{\text{vascular volume}}{\text{structure volume}} \quad (3.3)$$

To extract the vascular density, the islets are segmented using the algorithm described in Section 2.1.2. The vascular volume is computed similarly as described in Sections 5.2.6 and 5.2.7. The vascular network cannot be extracted as deep as the structural information. One explanation is the shadow artifact induced below each vessel (Fig. 3.3), which is likely due to the multiple scattering in the vessels. This artifact can lead to a massive over-evaluation of the vascular density. To solve this problem, we applied an exponential step down filter as described in Section 5.2.7. Still, this method can lead to a slight under-evaluation of the vascular density since portions of vessels that are directly located under another vessel might be cut and some small capillaries might be removed. Similarly, the lower part of large vessels may be removed (Fig. 3.3b).

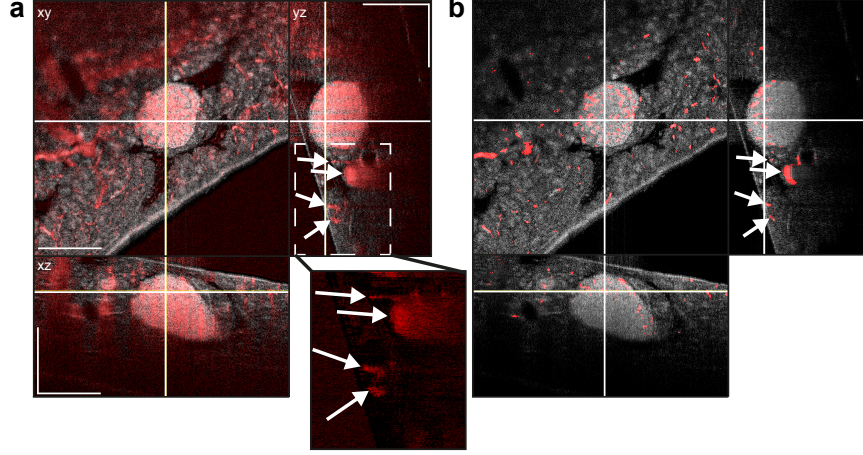


Figure 3.3: **Illustration of the shadow artifact.** (a) Artifact shadows are visible below vessels. (b) Results after application of the exponential step down filter and of the post processing described in Section 5.2.7. Scale bar: 200 μm .

In addition, the islets scatter more light (Section 5.1.2) than the exocrine tissue, thereby yielding a stronger attenuation of the vasculature signal in depth in the endocrine tissue. Except for very small islets, the vascular network cannot be completely observed over the whole islet depth, as shown in Figure 3.4. Therefore, dividing the vascular volume inside an islet by the total volume of this islet would yield an underestimation of the vascular volume as shown in Figure 3.4a. Based on immunohistochemistry, we can assume the vascularization to be uniform throughout a healthy islet [35]. In order to have unbiased absolute value, the vascular density was only computed on a subpart of the islet in depth (Fig. 3.4c) by allowing the user to define a region where the vascular volume was fully visible (Fig. 3.4b).

Blood flow

OCM can quantify the blood flow velocity on top of the structure of the vascular network. To this end, we applied the principle of joint Spectral and Time domain Optical Coherence Tomography (jSTdOCT) [181] to OCM in order to extract axial velocities, which we refer to as joint Spectral and Time domain OCM (jSTdOCM). The structure of a sample is obtained by performing a Fourier transform along the k -space (wavenumber). In the case of vascularized tissue, the Doppler effect created by the moving red blood cells adds a supplemental modulation of the spectrum over time. Hence, a Fourier transform along the temporal dimension allows us to retrieve the Doppler frequencies. The center of mass of the Fourier Transform over time can then be related to the axial velocity [182]. However, only red blood cells moving towards or away from the scanning beam can be detected, which means that only the axial component of the velocity is resolved.

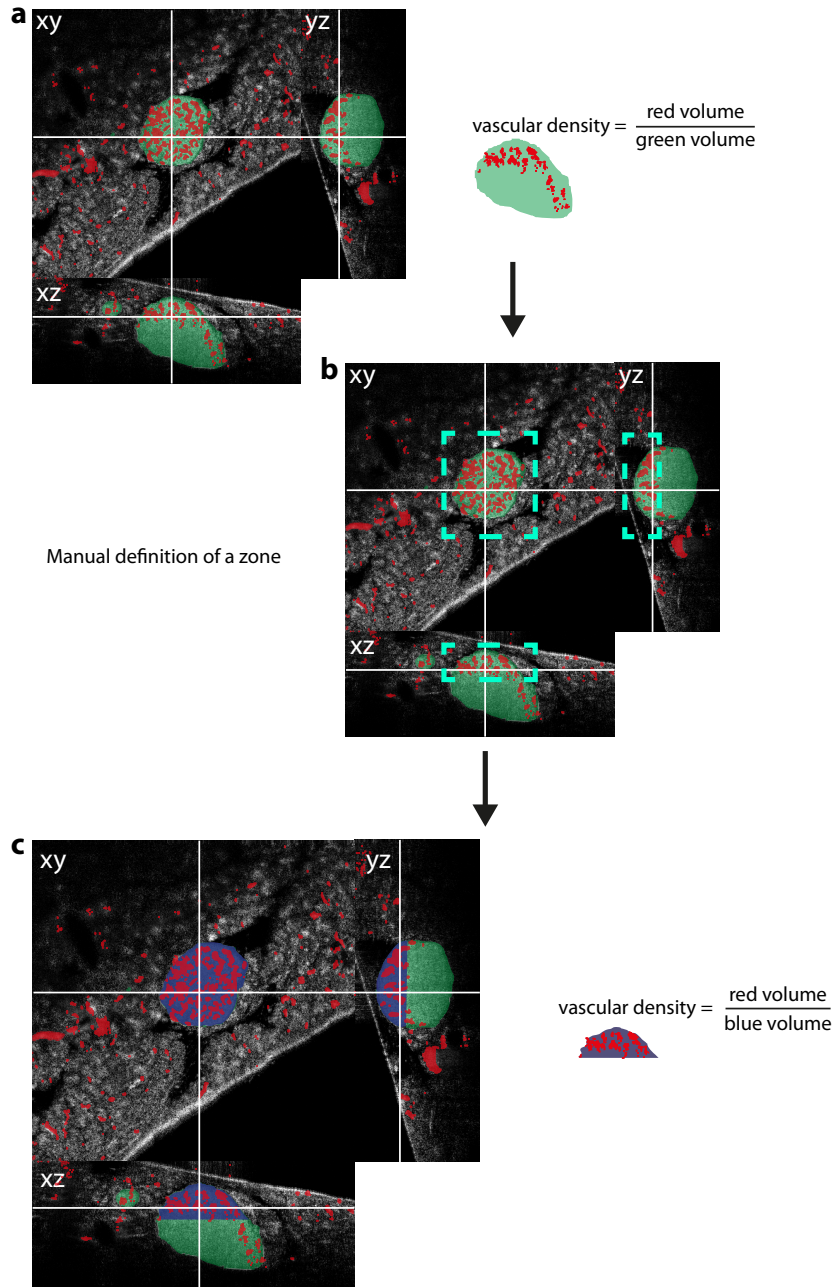


Figure 3.4: **Illustration of vessel attenuation in depth.** (a) When considering the whole islet, the vascular density is generally underestimated. (b) By selecting a subregion in which the vascularization is visible, (c) we can estimate more reliably the vascular density.

Therefore, parts of the vessels that are perpendicular to the beam (i.e., parallel to the tissue surface) are not detected. The acquisition rate defines the range of velocities that can be measured according to the following equation [181]:

$$v_{z,max} = \frac{\lambda_0}{4n\Delta t} \quad (3.4)$$

where $\Delta t = \frac{1}{f_s}$ is related to the sampling frequency f_s between two A-scans and n is the index of refraction of the tissue.

3.3 Results

By performing a laparotomy (Fig. 3.1), we are capable of imaging in three dimensions islets of Langerhans and their vasculature inside the pancreas of a mouse. Our images reveal a highly dense and tortuous vascularization inside the islets of Langerhans as compared to the adjacent exocrine pancreas (Fig. 3.5c), which we quantified to be four times less vascularized than the endocrine part. Our result is almost twice as large as the ~ 2.4 ratio between the endocrine and exocrine vascular density reported by Brissova *et al.* [35]. We measured an endocrine vascular density of 17%, which is in the range of the data observed by Dai *et al.* [169], even though these values are closer to ob/ob or high fat diet mice. These differences could be attributed to the genotype of the mice and to the different approaches to quantify the vascular density. Indeed, in OCM, the vascular network is revealed by moving red blood cells whereas the quantifications of Dai *et al.* and Brissova *et al.* are based on 10 μm cryosections where blood vessels are stained by intravital injection of lectin labeled with fluorescein. Figure 3.6 shows the diversity in term of shape and vascularization of different islets. A typical acquisition time for a three-dimensional stack of $800 \times 800 \times 300 \mu\text{m}^3$ is between 30 to 40 seconds. Decreasing the scanned area and signal averaging can further reduce the acquisition time. Stability of the samples due to motion artifacts (heartbeat, breathing and peristaltic movements in the duodenum) may occasionally lead to residual vertical lines in the images (Fig. 3.6).

We compared the vascular density computed over the whole islet (Fig. 3.4a) with the vascular density obtained over a subpart manually defined by the user (Fig. 3.4c). We found that, without analyzing a subpart, the vascular density is in average under-evaluated by approximatively 33%. This deviation depends on the volume and the orientation of the islet. This user-based definition of a subpart can only be done if we have a uniform structure. During the progression of inflammation like in T1DM, we can compare the relative vascular density either between affected or not affected regions inside a particular islet or in islet over time. By doing the relative comparison in islet over time, we assume that the underestimation bias stays constant over time.

Except for the main vessels visible by eye, blood flow in the pancreas requires a sampling frequency of 5 to 10 kHz. According to Equation 3.4, these sampling frequencies

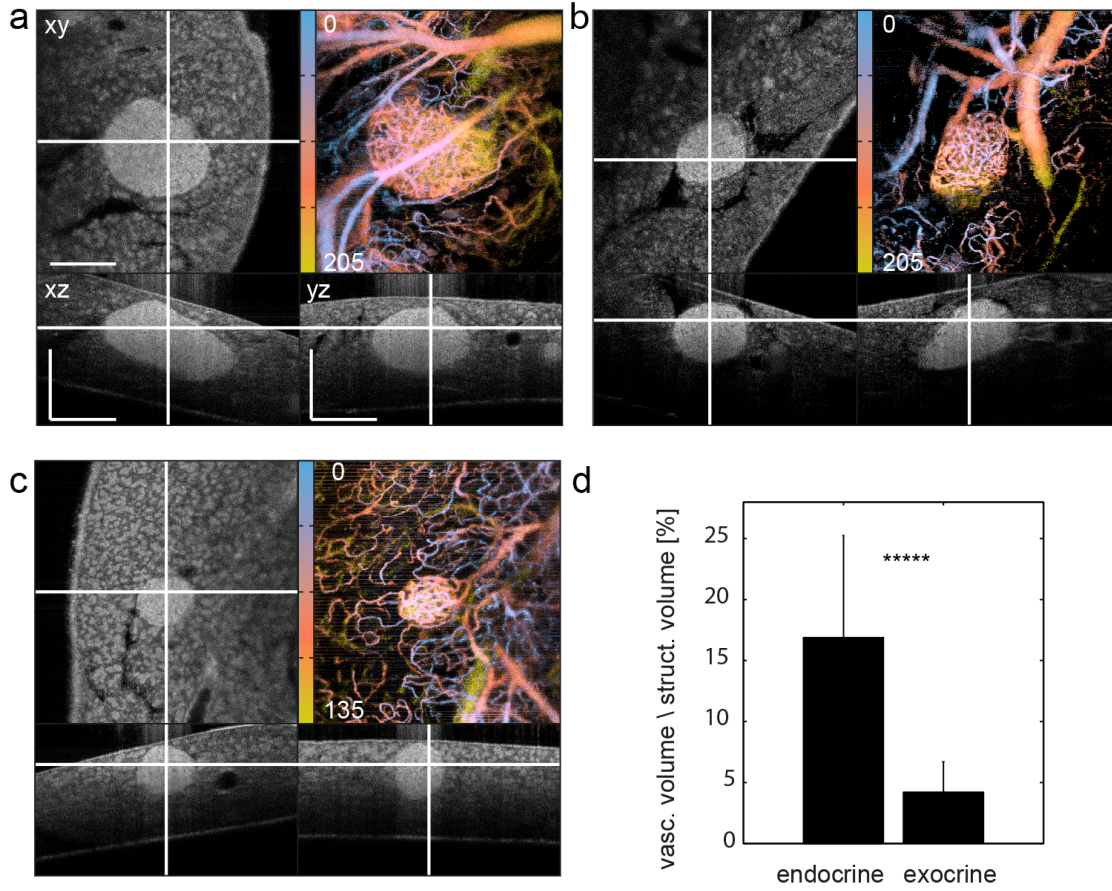


Figure 3.5: **Structure and vascularization of islets of Langerhans.** Representative (a) large islet ($13.7 \times 10^6 \mu\text{m}^3$), (b) medium islet ($7 \times 10^6 \mu\text{m}^3$) and (c) small islet ($2.7 \times 10^6 \mu\text{m}^3$). (d) Quantification of the vascular density, i.e, the vascular (vasc.) volume divided by the structural (struct.) volume in the exocrine and endocrine part. The p-value computed using a Mann-Whitney non-parametric U-test is smaller than 10^{-5} . 9 mice images and 16 islets analyzed. Colorbar indicates the depth in μm . Scale bar: 200 μm .

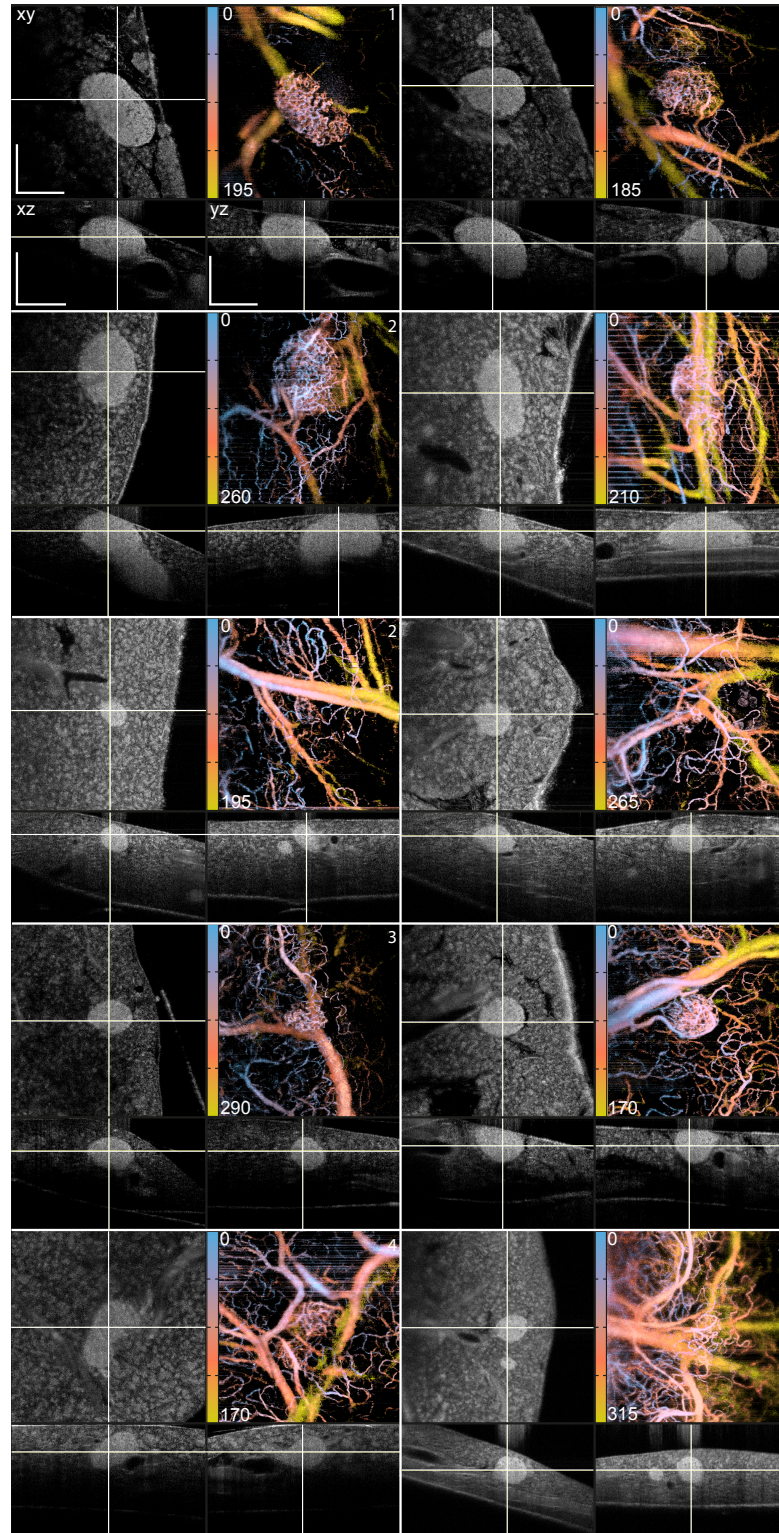


Figure 3.6: **Maximum depth projections of the vasculature for different islets.** The number in the top-right corner indicates in which mouse the islets were imaged from. Colorbars indicate the depth in μm . A-scan acquisition frequency: 20 or 50 kHz depending on pancreas stabilization. Scale bar: 200 μm .

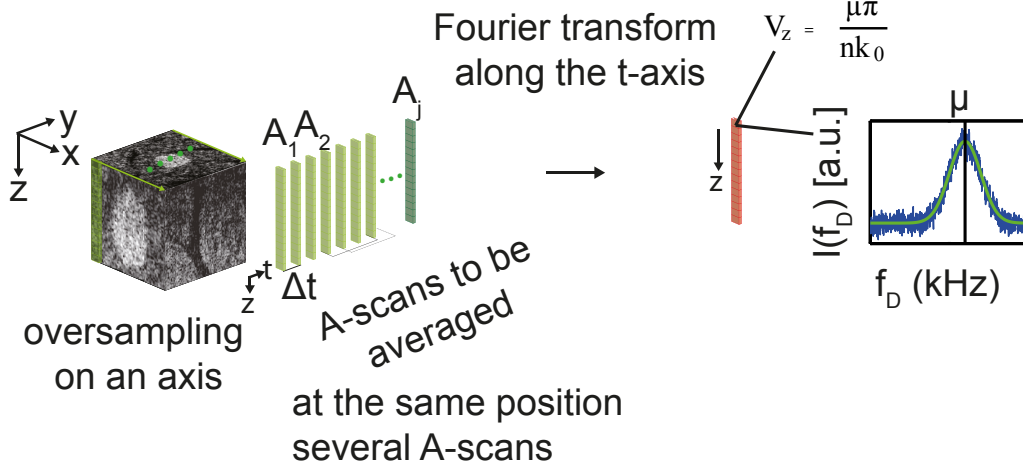


Figure 3.7: **Schematic representation of the data processing to extract blood flow.** For each pixel in a A-scan, the axial velocity V_z is related to the mean μ of the Doppler frequency f_D , the refractive index n and the central wave number of the source k_0 .

correspond to maximum axial velocities of 0.75 mm/s and 1.5 mm/s, which represent a time interval Δt of 100-200 μ s between successive A-scans. For mechanical reasons, the scanning system cannot acquire several points at the same spatial position. However, by oversampling in one direction we can obtain a pixel resolution lower than the beam spot size (Figure 3.7), thereby allowing us to acquire several points (~ 10 times oversampling) at the same position. Figure 3.8 shows axial velocities computed inside the pancreas at 5 kHz. The acquisition time for this image was 10 minutes, thus requiring an excellent stabilization of the pancreas. We noticed that the high scattering coming from the islets impaired the detection of blood flow inside the islets. Even when large islets were at the surface of the pancreas, only a few vessels inside those islets could be detected whereas numerous vessels were visible at the same depth in the exocrine tissue.

Nevertheless, when focusing on a given vessel, the time resolution is sufficient to extract the heart beat. Figure 3.9 shows a large vessel in the exocrine pancreas imaged over time. The blood flow was analyzed using the jSTdOCM algorithm to extract the axial projections of velocity vectors along the vessel. Several pixels in depth were averaged to extract vessel pulsation over time and one line over time was selected to plot the pulsation of the signal amplitude (Fig. 3.9c). As presented in Figure 3.9d using a frequency analysis, the heart beat was found to be around 3.4 Hz, which is in agreement with the study of Janssen *et al.* in the case of mixed anesthetics [183].

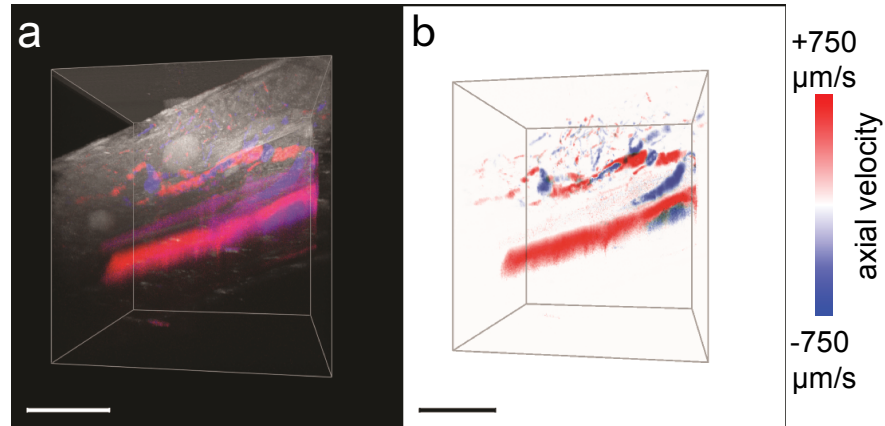


Figure 3.8: **Three-dimensional rendering of the blood flow direction inside the pancreas.** Red and blue color represent opposite axial blood flow direction. (a) Overlay of both the structural and blood flow information. (b) Corresponding three-dimensional blood flow imaging. Scale bar: 100 μm .

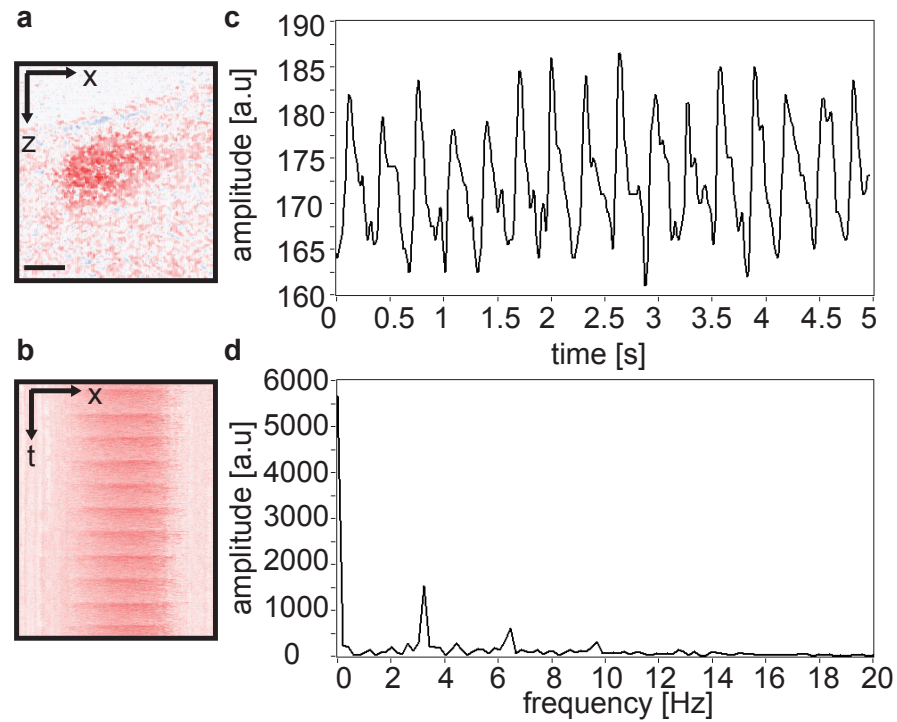


Figure 3.9: **jSTdOCM-based measurement of heart beat frequency.** (a) Blood flow visible in a pancreatic vessel. (b) Vessel pulse over time of the vessel shown in (a). (c) Pulse amplitude of the blood flow over time. (d) Frequency analysis of the signal in (c). Acquisition rate 50 kHz with 512 pixels in the x-direction. Scale bar: 20 μm .

3.4 Discussion

We have conceived, developed and established a label-free imaging technique with a micrometric lateral ($\sim 1.3 \mu\text{m}$) and axial ($\sim 2.5 \mu\text{m}$) resolution, a high sensitivity, and a penetration depth of $\sim 400 \mu\text{m}$ to image individual islets with their vascularization *in situ*. The vascular network was extracted over a sufficient depth to measure significant differences in vascular density between endocrine and exocrine tissue. Compared to fluorescent intravital microscopy, OCM label-free imaging of vascularization eliminates bleaching or toxicity of the fluorescent contrast agent, rendering OCM suitable for longitudinal studies. Studies on islet vascular density have mainly been done *ex vivo* by staining markers of endothelial cells [35, 45, 48, 184]. Intravital microscopy has been used to reveal the vascular network in islet [108, 113] and to extract blood flow velocity [43, 169]. However, these methods can only focus on subpart of vessels lying in a defined axial plane whereas OCM can simultaneously resolve all the pixels along the axial dimension, thereby analyzing several vessels in parallel. This fast acquisition is sufficient to resolve blood flow dynamic as well as to analyze several vessels including a full volume. In addition, axial velocity indicates whether the red blood cells flow towards or away from the optical beam. This axial direction can be further used to determine whether a vessel is entering or exiting an islet. While *in vivo* xFOCM penetration depth is around $400 \mu\text{m}$ for structural information, vascularization cannot be fully extracted over the same depth. Multiple scattering inside blood vessels create a shadow-artifact under each vessel producing a blurred and attenuated signal of the vasculature in depth. Measuring axial blood flow imposes a limitation as vessel segments perpendicular to the optical axis cannot be resolved, which results in non-continuous vessels (Fig. 3.8b). In capillaries, the slow blood flow translates into an irregular red blood cells filling, thereby resulting in weak Doppler shifts comparable to the phase noise. Combined with movements from the sample, this results in a poor sensitivity to resolve blood flow in small capillaries. In addition, despite small capillaries being visible in the exocrine tissue, almost no quantitative blood flow velocity could be extracted in endocrine vessels at the same acquisition rate. Besides the stronger scattering of the endocrine part that could hinder the blood flow signal, this might indicate a slower blood flow inside the islets than in the exocrine tissue. While OCM blood flow is less sensitive to capillaries, fluorescence microscopy is mainly limited to capillaries [185–187]. Indeed, fluorescence microscopy is not suitable to resolve the continuous fast blood flow in large vessels.

In this thesis, we use jSTdOCM to obtain real-time previews (B-scans) of the tissue to assess its vitality. Nevertheless, axial velocity measurements allows extraction of volumetric flow and perfusion [163], or dynamic change in hematocrit content [188]. Recently, Bouwens *et al.* [189] developed a general model allowing quantitative imaging of the transverse and axial velocity components taking into account the NA and beam geometry of the xFOCM, enabling the measurements in three-dimensions of total flow in the brain [167]. These blood flow characteristics require a stabilization of the investigated

tissue over several minutes, which is challenging in the pancreas. However, the anterior chamber of the eye (Chapter 5) as a transplantation site for pancreatic islets might offer an easier stabilization and seems more suitable to investigate blood flow, especially since non-invasive longitudinal studies could be performed. An additional contrast enhancement could be achieved by the injection of an intralipid solution [190]. This intralipid solution contains multiple scatterers increasing the filling rate in the capillaries, allowing for a better measurements of the Doppler shift. In conclusion, OCM opens the door to the study of the interactions between islets of Langerhans, their vascular network and blood flow under both physiological and diabetic conditions.

4 OCM and the specificity of β -cell tracers

Identification of specific tracers for β -cells would have a major impact on diabetes diagnosis and therapy. However, the specificity of tracers cannot be fully assessed using MRI, PET or SPECT due to their low spatial resolution. Indeed, they need labeling to differentiate endocrine from exocrine tissue. So far, only optical imaging has provided sufficient spatial resolution to image individual islets of Langerhans.

In this chapter, we explore OCM as a new technological platform to facilitate initial tests and to speed up the general search of β -cell tracers. In this study, we demonstrate the use of OCM both at the cellular and organ level to assess the specificity of a tracer. We use OCM for an *in vivo* label-free detection of pancreatic β -cells based on their intrinsic back-scattering properties as well as to image cells *in vitro*. In order to follow the tracer, we enhanced our OCM setup with a fluorescent channel that allows simultaneous detection of the OCM and fluorescent signal. As a proof-of-concept, we investigate the specificity of Cy5.5-exendin-3 for β -cells.

4.1 Specific tracers for β -cells

To be suitable for β -cell imaging, an ideal tracer must be small, specific, have a high affinity, be cleared from blood stream and non-target tissues in a short period of time, and of course be non-toxic [96]. Antibodies targeting β -cells have been proposed, but their large size prevents their optimal diffusion into the endocrine tissue. Anti-diabetic drugs such as glibenclamide and tolbutamide have been tested, but they are not specific enough and their signal-to-background ratio is too low [191]. Targeting receptors specific to pancreatic β -cells is another option. Potential candidates are dopamine receptor, vesicular monoamine transporter (VMAT2), glucagon-like peptide-1 receptor (GLP1R) and sulfonylurea receptor 1 (SUR1) [96].

VMAT2 has been targeted by using the ligand dihydrotetrabenazine (DTBZ) [192] with a decrease in ligand uptake observed both in a spontaneous model of type I diabetes [133]

and in streptozotocin-induced diabetes in rats [193]. However, β -cell depletion by diphtheria toxin injection of mice expressing the diphtheria toxin receptor under the insulin promoter did not reveal a change in DTBZ-based PET imaging, thus suggesting that the signal is not β -cell specific. In the same study, no radiotracer retention was observed in human islets grafted under the kidney capsule [194]. However, in long-standing type I diabetic patients with a predicted close to complete loss of the β -cell mass, a decrease of the signal was observed as compared to control even though a significant uptake of DTBZ was still observed [195]. This finding could be explained by the expression of VMAT2 in PP-cells and in nerve fibers, which are both present in the endocrine tissue [196, 197]. In addition, there are indications that VMAT2 is not expressed in rodents, which questions the validity of pre-clinical studies done on rats or mice [198]. Therefore, there is still an on-going controversy about the potential to target VMAT2 as a marker for β -cells.

GLP1 (glucagon-like peptide-1) is derived from proglucagon and is a peptide-hormone released from intestinal L-cells after food ingestion. GLP1 stimulates insulin secretion, decreases glucagon secretion, stimulates β -cell proliferation and inhibits apoptosis [199, 200]. Therefore, it plays a major role in glucose homeostasis. GLP1R mRNA expression is found in human pancreas, but also in lungs, brain, kidneys, stomach and heart [201] with a similar expression in the rat [202]. In a healthy human pancreas, GLP1R density has been shown to be twice as large in islets as in acini using autoradiography for GLP1 [203]. However, this density is lost in pancreatitis and becomes similar to the exocrine pancreas [203]. In addition to the pancreas, a high GLP1R density is present in the central nervous system and in the duodenum [203]. Using freshly isolated whole pancreatic organ, Tornehave *et al.* [204] showed that GLP1R is expressed in pancreatic β -cells of mice, rats and humans, but not in other types of islet cells. GLP1R immunoreactivity was also detected in ducts with strongest expression in most of the large ducts [204]. Recently, Pyke *et al.* [205] developed a monoclonal antibody against the human GLP1R extracellular domain for immunohistochemistry. They demonstrated colocalization of GLP1R and insulin, but not in the other islet cells (glucagon, somatostatin, and pancreatic polypeptide cells) in normal pancreases of monkey. A variable and weaker signal of GLP1R in the acinar cells was present, but no signal of GLP1R was detectable in ducts. Similarly, normal human pancreases show colocalization of GLP1R and insulin, weaker and variable signal in acinar cells and no staining in ducts. Colocalization with insulin is maintained in both human and monkey diabetic pancreas. In addition to monkey pancreas, they analyzed kidney, lung, heart, gastrointestinal tract, liver, and thyroid from monkeys for GLP1R expression. Except for the liver and the thyroid, the other organs have cells expressing GLP1R. Among the analyzed organs that express GLP1R, the duodenum shows the higher signal expression. The absence of GLP1R in the α -cells is in contradiction with the findings of Heller *et al.* [206], who observed GLP1R immunoreactivity on 20% of α -cells using *in vitro* islets. These contradictory results could be explained by the different preparations, i.e., fixed tissue versus *in vitro* islets.

However, compared to the other studies, the specificity of the antibody used by Heller *et al.* [206] was only assessed on cells transfected with the GLP1R and not on pancreatic tissue from knock-out mice for the GLP1R.

GLP1 is the endogenous ligand of GLP1R, but its short half-life (1-2 minutes) due to the inactivation by the enzyme dipeptidyl peptidase-4 (DPP-4) prevents its use for therapeutic or imaging purposes [200]. Exendin-3 and Exendin-4 are more stable agonists of the the GLP1R. Exendin-3 is derived from *Heloderma horridum*, the Beaded Mexican Lizard (Mexico and southern Guatemala), and Exendin-4 from *Heloderma Suspectum*, the Gilamonster (a lizard living in the South West of the United States and northern Mexico) [96]. Following stimulation with GLP1 or analogues, the GLP1R is rapidly internalized with a fast rate of recycling even after prolonged treatment [207]. Using these analogues, promising results have been obtained with PET/SPECT [208–214], MRI [215, 216] and fluorescence microscopy [217, 218]. Intriguingly, a study on streptozotocin-induced diabetic pigs imaged with PET did not show a difference in exendin-4 uptake between non-diabetic and diabetic pigs [219] whereas a difference was detected in streptozotocin treated rats [220]. This discrepancy certainly reflects differences in GLP1R expression between species. Recently, Brand *et al.* [221] used near-infrared fluorescent dye with a radiotracer to label exendin-4 and applied this probe to perform bimodal imaging of insulinomas and β -cells in mice. Indeed, in addition to detect β -cells, GLP1R targeting demonstrates good results to detect insulinomas [134, 222–224]. Even if antagonists of GLP1R such as exendin(9-39) have been less investigated to image β -cells, some studies have shown their potential [225, 226]. Despite these different attempts and trials, an ideal *in vivo* tracer for β -cells is not yet available. Therefore, initial evaluation of tracer specificity is still required on small animals.

4.2 Journal article

Accepted in: Scientific Reports

Combined Optical Coherence and Fluorescence Microscopy to assess dynamics and specificity of pancreatic beta-cell tracers

Corinne Berclaz¹, Christophe Pache¹, Arno Bouwens¹, Daniel Szlag^{1,4}, Antonio Lopez¹, Lieke Joosten², Selen Ekim², Maarten Brom², Martin Gotthardt², Anne Grapin-Botton³, and Theo Lasser¹

¹Ecole Polytechnique Fédérale de Lausanne, Lausanne, Switzerland; ²Radboud University Medical Center, Nijmegen, the Netherlands; ³Danish Stem Cell Center, Copenhagen, Denmark; ⁴Institute of Physics, Faculty of Physics, Astronomy and Informatics, Nicolaus Copernicus University, Grudziadzka 5, PL-87-100 Torun, Poland

The identification of a β -cell tracer is a major quest in diabetes research. However, since MRI, PET and SPECT cannot resolve individual islets, optical techniques are required to assess the specificity of these tracers. We propose to combine Optical Coherence Microscopy (OCM) with fluorescence detection in a single optical platform to facilitate these initial screening steps from cell culture up to living rodents. OCM can image islets and vascularization without any labeling. Thereby, it alleviates the need of both genetically modified mice to detect islets and injection of external dye to reveal vascularization. We characterized Cy5.5-exendin-3, an agonist of glucagon-like peptide 1 receptor (GLP1R), for which other imaging modalities have been used and can serve as a reference. Cultured cells transfected with GLP1R and incubated with different concentrations of Cy5.5-exendin-3 show full tracer internalization. We determined that a dose of 1 μ g of Cy5.5-exendin-3 is sufficient to optically detect *in vivo* the tracer in islets with a high specificity. In a next step, time-lapse OCM imaging was used to monitor the rapid and specific tracer accumulation in murine islets and its persistence over several hours. This optical platform represents a versatile toolbox for selecting β -cell specific markers for diabetes research and future clinical diagnosis.

4.2.1 Introduction

Islets of Langerhans are structures hosting the insulin-producing β -cells, which play a central role in glucose homeostasis. For a deeper understanding of the pathogenesis of diabetes and for developing beneficial treatments protecting β -cells, improving their

function or promoting their proliferation/regeneration during diabetes, an accurate assessment of the β -cell volume is necessary. These ambitious goals motivate the search for specific β -cell markers. The utmost goal is to achieve human *in vivo* imaging of β -cells, which is an on-going worldwide effort of intensive research [96, 227]. Non-invasive clinical imaging techniques such as MRI, PET or SPECT rely on contrast agents or radio-ligand tracers to discriminate between the endocrine and exocrine pancreas. However, these clinical imaging modalities cannot provide a sufficient resolution to resolve individual islets, and therefore rely solely on the contrast quality of the used bio-tracer. Therefore, imaging of smaller individual islets requires the higher spatial resolution of optical imaging. Although optical imaging has a limited penetration depth of a few hundred micrometers and therefore would have very limited use in a clinical setting, it can provide an alternative to assess the specificity of β -cell markers in recognized animal models. In principle, classical optical techniques such as fluorescence microscopy, confocal [217] or two-photon microscopy [104] allow identifying fluorescently labelled β -cell tracers. However, their voxel by voxel scanning results in long imaging acquisition time, making *in vivo* imaging of the pancreas in the abdominal cavity and time-lapse imaging during the tracer accumulation challenging. Line-scanning confocal fluorescence imaging overcomes this speed limitation [38] but similarly to other classical optical techniques requires genetically modified mice to visualize pancreatic islets [103]. Optical Coherence Microscopy (OCM) circumvents all these limitations by providing fast, three-dimensional label-free imaging of islets of Langerhans [107, 161] along with the islet vascularization and blood flow [128, 167, 180]. In this paper, we exploit the advantages of OCM enhanced with a confocal fluorescence channel to assess the specificity and the dynamics of a β -cell tracer linked to a fluorophore. As a proof of principle, we demonstrate the high β -cell specificity of a Cy5.5-exendin-3 tracer *in vitro* and *in vivo* for which other imaging modalities have been used and can serve as reference. Exendin-3 is an agonist of the glucagon-like peptide-1 (GLP1) that targets glucagon-like peptide-1 receptor (GLP1R), a promising candidate due to the specificity and the high level of GLP1R expression on β -cells [204, 205, 228]. Using GLP1 agonists, promising results have been obtained with PET and SPECT [208, 210–213, 220], MRI [215, 216] and fluorescence microscopy [217, 218, 221]. Our study reveals promising specificity and dynamic features of GLP1 tracers and sets a platform for further characterization of β -cell tracers.

4.2.2 Research design and methods

Animals and pancreas imaging with xfOCM

The Swiss veterinary authorities approved all procedures and animal protocols for the described studies. For these investigations, ICR female adult mice were obtained from the Harlan laboratories and underwent laparotomy procedure as previously described [107]. For imaging longer than 30 minutes, the anesthesia was prolonged with 1% isoflurane

Chapter 4. OCM and the specificity of β -cell tracers

mixed with oxygen. During the imaging session the mice are kept on a heating stage. The animals were imaged using the xfOCM/confocal fluorescence (Fig. 4.1) dual system to image the islets (OCM-mode) and the Cy5.5 tracer (fluorescence mode).

Cell culture and imaging with dfOCM

Chinese hamster lung (CHL) cells stably transfected with the human GLP1-receptor (CHL-hGLP1R) [229] are a donation from Martin Béhé (PSI, Switzerland). CHL-hGLP1R were grown in Dulbecco's Modified Eagle's Medium (DMEM) GlutaMax (Gibco, Invitrogen, catalog 61965) supplemented with 10% heat-inactivated fetal calf serum (vol/vol), 100 units/ml penicillin and 100 μ g/ml streptomycin, 50 mg/ml geneticin (G418) sulphate solution (PAA laboratories GmbH, GE Healthcare), 1 mM sodium pyruvate, and 0.1 mM Non-Essential Amino Acids (NEAA), in a humidified 5% CO₂ atmosphere at 37° C. hGLP1R negative CHL cells were grown in the same medium but without geneticin. The cells were harvested by trypsinization with trypsin/EDTA. CHL-hGLP1R and CHL negative cells were seeded on μ -Dish 35 mm (Ibidi) and cultured overnight. The cells were washed three times with Krebs buffer (NaCl 7.795 g/L, KCl 0.354 g/L, KH₂PO₄ 0.162 g/L, MgSO₄H₂O 0.293g/L, CaCl₂H₂O 0.374 g/L, NaHCO₃ 0.424 g/L, Hepes 2.39 g/L) and incubated at 37° C or 4° C with Cy5.5-exendin-3 (0-100 nM) for 90 min in Krebs buffer with 3.9 mM glucose. Following incubation, cells were washed three times with Krebs buffer and put at 4° C before imaging. Cells were imaged using the dfOCM/confocal fluorescence dual system (Fig. 4.1) to match the signals originating from cells and the Cy5.5-exendin-3 tracer.

Conjugation of Exendin-3 with fluorophore and radionuclide and IC₅₀ determination ¹¹¹InCl₃ was obtained from Covidien (Petten, The Netherlands) and (DTPA-) exendin-3 was purchased from Peptide Specialty Laboratories (PSL, Heidelberg, Germany). Cy5.5 Mono NHS Ester was purchased from Amersham (GE Healthcare, Buckinghamshire, UK) and conjugated to exendin-3 by PSL. Both DTPA and CyTM5.5 Mono NHS Ester were conjugated to the ϵ -amino group of the Lysine residue at position 40. DTPA-exendin-3 was radiolabeled with ¹¹¹InCl₃ as described previously [224]. The 50% inhibitory concentrations (IC₅₀) of exendin-3 and Cy5.5-exendin-3 were determined using CHL-GLP1R cells, grown to confluence in 6-wells plates. Concentrations of the unlabeled exendin-3 and Cy5.5-exendin-3 ranging from 0.1 to 300 nmol in DMEM-GlutaMax with 0.5% (w/v) bovine serum albumin (BSA) (n=3) were added to the cells together with 50,000 cpm ¹¹¹In-DTPA-exendin-3. The cells were incubated for 4 hours on ice, washed twice with DMEM-GlutaMax with 0.5% BSA and harvested using 1 ml 0.1M NaOH. The radioactivity associated with the cells was measured in a well-type gamma counter (Wallac 1480-Wizard, Perkin-Elmer, Boston, MA, USA). The IC₅₀ values were calculated by one-site competition analysis with Graphpad Prism (version 5.03, GraphPad Software, San Diego California USA). An unpaired t-test was used for significance determination with a p-value below 0.05 considered as significant.

***In vivo* evaluation of different doses, blocking experiments, time-lapse imaging and image analysis**

Mice were injected intravenously in the tail vein with either 0.1 μg (2.6 $\mu\text{g}/\text{kg}$, 0.5 nmol/kg , $n=4$ mice, 65 islets analyzed in total), 1 μg (26.3 $\mu\text{g}/\text{kg}$, 5.5 nmol/kg , $n=5$ mice, 68 islets analyzed in total) or 14 μg (391.7 $\mu\text{g}/\text{kg}$, 82.2 nmol/kg , $n=4$ mice, 34 islets analyzed in total) of Cy5.5-exendin-3 in 200 μl of PBS and imaged 4 hours after ligand injection. Control mice ($n=5$ mice, 24 islets analyzed in total) were injected with PBS only. For blocking experiments, 1 μg of Cy5.5-exendin-3 and 100 μg of exendin-3 (2.8 mg/kg , 0.6 $\mu\text{mol}/\text{kg}$) in 200 μl of PBS were injected intravenously in the tail vein and imaged 4 hours later ($n=4$ mice, 56 islets analyzed in total). For time-lapse imaging, mice were injected intravenously with 1 μg of Cy5.5-exendin-3 in 200 μl of PBS and imaged for up to 4 hours ($n=4$ mice, 9 islets analyzed in total). Quantification of the fluorescence signal of Cy5.5-exendin-3 was performed on images taken with an open pinhole. The median fluorescent intensity of the pixels belonging to an islet was quantified in a post processing step by a semi-automatic segmentation of the fluorescent signal overlapping the OCM signal of islet. For time-lapse imaging, the time intensity curve was smoothed with an averaging filter of three, i.e., each point represents the averaging of 3 consecutive points.

OCM instruments for small animal and cell imaging

xfOCM All *in vivo* imaging was performed with our xfOCM instrument [123, 167] equipped with a Zeiss Neofluar objective (10x, NA 0.3, Carl Zeiss) with a lateral resolution of 1.3 μm and a depth of field of 400 μm . The illumination power on the pancreas was around 5 mW to acquire a full profile over the extended depth. Imaging the pancreas vascularization is based on a specific scanning protocol [166] and a phase variance algorithm [180]. This method uses a specific scanning protocol where each line (B-scan) is scanned several times. For our measurements, 8 B-scans were taken at 50 kHz (18 μs integration time per depth-profile). The circular variance of temporal phase changes was calculated to extract the vascularization. To improve the contrast, the circular variance was averaged over a window of 8 pixels in the axial direction.

dfOCM The dark field OCM (dfOCM) [129] is used for cell imaging. dfOCM suppresses all specular reflections which originate from the sample slide. For *in vitro* cell imaging, the added darkfield mask placed in a conjugated plane to the back focal plane of the objective, increases the contrast for cell measurements substantially. Our dfOCM instrument contains a plan apochromat immersion objective (25x, NA=0.8, Carl Zeiss) resulting in a 900 nm lateral resolution and 3 μm axial resolution over a field depth of 50 μm .

Both instruments have a fluorescence channel using the same scanning unit for a simultaneous acquisition of the fluorescence and the OCM signal. For suppressing any crosstalk

Chapter 4. OCM and the specificity of β -cell tracers

between the OCM and fluorescence channel detection, a high pass filter (HQ720lp, Chroma Technology Corp.) is placed in the illumination arm. For the fluorescence excitation, a tunable supercontinuum laser was used (Koheras SuperK Extreme, NKT Photonics). A dichroic mirror (720dcxr, Chroma Technology Corp. and a KG1 Schott infrared absorber) in combination with a complementary excitation filter (HQ680/35m, Chroma Technology Corp.) rejects the NIR spectrum and enhances the SNR for the fluorescence detection. Excitation and emission light was separated by a dichroic mirror and excitation filter (z647RDC, Chroma Technology Corp. and Z635/10x, Chroma Technology Corp.). The fluorescence signal was detected by an avalanche photodiode (SPCM-AQR-14-FC; PerkinElmer) and digitized with a NIDAQ card (National instruments).

Immunofluorescence

At the end of the imaging session, mice were intraperitoneally injected with 1 ml/kg body weight of a solution of pentobarbital (150 mg/ml). The deeply anesthetized animals were transcardially perfused for 2 minutes with PBS and for 8 minutes with 4% paraformaldehyde (PFA) solution. The pancreas was further fixed for 1 day at 4° C in 4% PFA, prior to an overnight incubation in a 30% (wt/vol.) sucrose solution in PBS at 4° C. The pancreas was embedded in Optimal Cutting Temperature compound and frozen in isopentane cooled with dry ice. 8 μ m cryosections were prepared for staining. The sections were permeabilized 10 minutes with PBS-TritonX100 0.25% and blocked in 10% fetal bovine serum for 30 minutes at room temperature. Incubation with primary antibodies (guinea pig insulin 1:50 Dako, rabbit glucagon 1:200 Cell Signaling, rat e-cadherin 1:100 Takara Bio) was performed at 4° C overnight in a humid chamber. Secondary antibodies were incubated 45 minutes at room temperature. The sections were further stained with Dapi (1:10000) for 10 minutes at room temperature and mounted with DABCO mounting medium. These immunostained samples were inspected with a Zeiss LSM 710 microscope equipped with a 63x oil Plan-Apochromat objective (NA=1.4).

Statistical analysis

Data are presented as mean with standard deviation.

4.2.3 Results

Exendin-3 coupled to Cy5.5 retains efficient binding to GLP1R

The tracer exendin-3 has already been investigated with different modalities [213, 224]. For an optical monitoring of the exendin-3 binding process to cells expressing GLP1R *in vivo*, we coupled Cy5.5 to exendin-3 to the epsilon amino-group of the C-terminal lysine in analogy to the DTPA conjugated exendin. This strategy allows a straight comparison between the radiolabeled and fluorescently labeled compound. To investigate

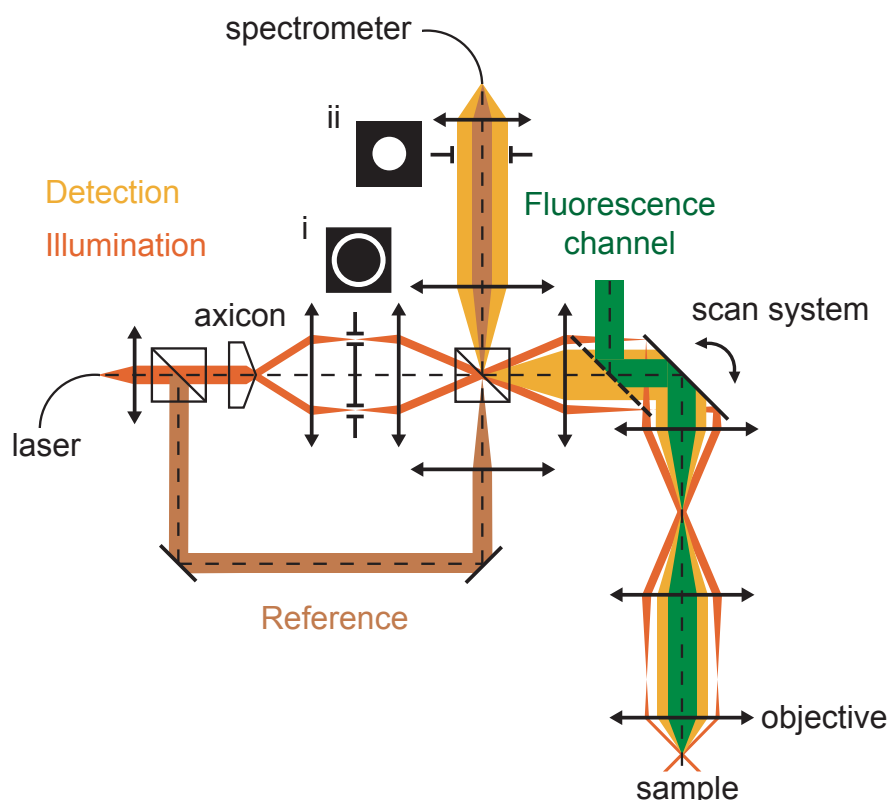


Figure 4.1: **Schematic layout of the dual systems.** The dark-field effect is obtained by adding an annular mask (i) in the illumination and a pupil mask (ii) in the detection arm.

if this modification alters the pharmacological properties DTPA-exendin-3 was labeled with $^{111}\text{InC}_3$ with a specific activity of 700 GBq/ μmol . The radiochemical purity was 95% as determined by ITLC. Radiolabelled exendin-3 and Cy5.5-exendin-3 were used to determine the IC₅₀ diagrams using Chinese hamster lung (CHL) cells stably expressing GLP1R. Both compounds showed a high affinity for the GLP1R. The IC₅₀ values of exendin-3 and Cy5.5-exendin-3 were 2.6 nM and 10.8 nM respectively (Fig. 4.2 with 95% confidence intervals of 1.9-3.4 and 7.0-16.7 respectively). These values in the nanomolar range are not significantly different ($p=0.68$).

Cy5.5-exendin-3 binding and internalization *in vitro* in cells expressing GLP1R

To assess the specificity of Cy5.5-exendin-3 for GLP1R, stably transfected CHL cells with the human GLP1R were used and imaged with dark field OCM (dfOCM). The novel instrument we designed (Fig. 4.1) combines OCM to detect islets or cells based on their natural scattering [107] with fluorescence to detect the tested tracer. OCM part works in two configurations: extended focus OCM (xfOCM) [123] and dark field

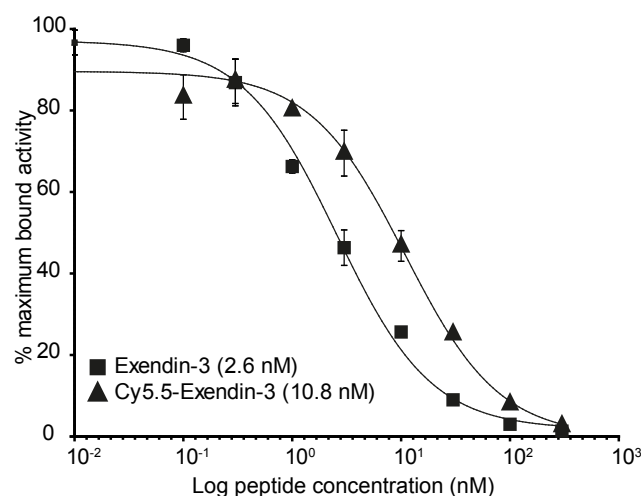


Figure 4.2: **Competition binding assay (IC₅₀) of exendin-3 and Cy5.5-exendin-3 on CHL-GLP1R cells.** ¹¹¹In-DTPA-exendin-3 was used as tracer. The sample with the highest binding percentage was set at 100%.

OCM (dfOCM) [129]. xfOCM is optimized for small animal imaging whereas dfOCM possesses dark field contrast enhancement and is designed for cell imaging. dfOCM allows imaging of the weak scattering signal from cells by suppressing the strong reflection originating from the microscope slide. We investigated a concentration range of 0-100 nM of Cy5.5-exendin-3 on CHL cells positive or negative for GLP1R. To discriminate between internalization and binding, the cells were incubated at either 37° C or 4° C for 90 minutes. As shown in Figure 4.3, complete internalization is observable down to 1 nM at 37° C whereas only a membrane staining is seen at 4° C . In both cases, no signal is detectable in the CHL negative control. As an additional control we used a conventional confocal fluorescence microscope, which confirmed our findings.

Determination of Cy5.5-exendin-3 dose for a specific islet detection

To determine the minimum dose required for *in vivo* tracer detection of a fluorescence labeled tracer, three different doses of Cy5.5-exendin-3 (0.1, 1 and 14 µg per mouse that is 2.6, 26.3 and 391.7 µg/kg) were investigated. No fluorescent signal inside the islets could be detected 4 hours after the intravenous injection of 0.1 µg of Cy5.5-exendin-3. Only in rare cases (< 5%) a weak fluorescence appeared at the limit of observation. Conversely both at 1 µg and 14 µg doses, the tracer accumulates only inside the islet 4 hours after injection (Fig. 4.4a). Although the fluorescence intensity of islets in mice injected with 14 µg was stronger than at 1 µg of Cy5.5-exendin-3 (Fig. 4.4b), the background signal in the exocrine pancreas was higher at 14 µg than at 1 µg of Cy5.5-exendin-3 (Fig. 4.4c),

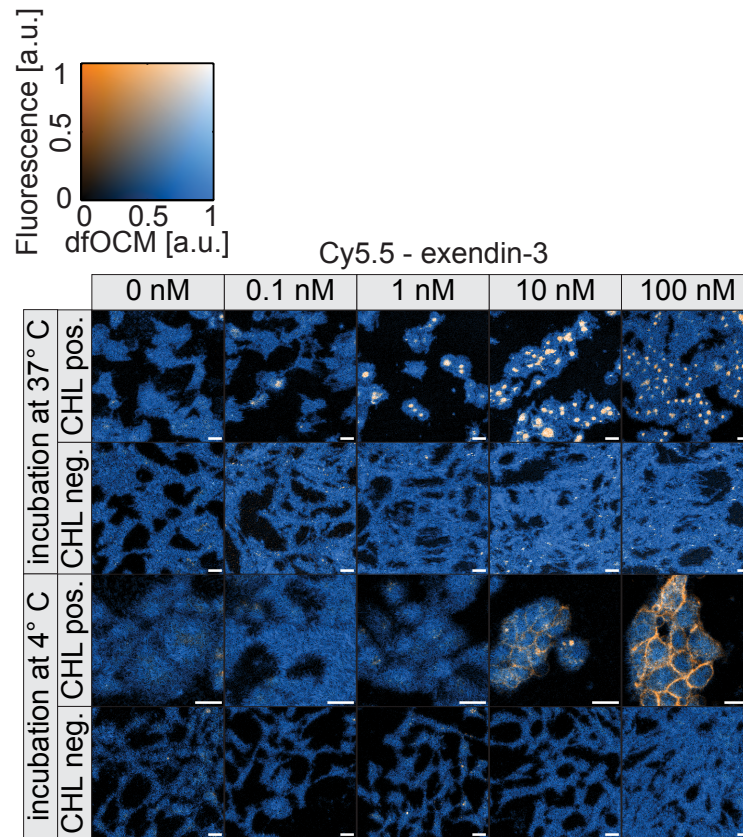


Figure 4.3: Cell imaging with the OCM/fluorescence platform after 90 min of incubation with different concentrations of Cy5.5-exendin-3 (0-100 nM) with CHL positive or negative for hGLP1R. Scale bar: 20 μ m.

with a dot-like staining in the exocrine pancreas (Fig. 4.4a). In addition while right after injection of a 14 μ g tracer dose, a fluorescent signal appeared in the pancreas vasculature, at an intermediate dose of 1 μ g of Cy5.5-exendin-3, no fluorescent signal was observed in the vasculature but a strong fluorescent signal appeared inside the islets right after injection (Fig. 4.5). A dose of 1 μ g of Cy5.5-exendin-3 is considered to be optimal based on our quantitative analysis. Firstly, the ratio (mean endocrine / mean exocrine fluorescence intensity) was ~ 6 for a 1 μ g dose and decreases to 4 for a 14 μ g dose. Secondly, this finding is supported by the fact that the fluorescence signal with 1 μ g dose was well observable at 4 hours (Fig. 4.4b) after injection and that the signal in the exocrine pancreas was as low as in the control animals (Fig. 4.4c). In addition, we investigated whether there was a correlation between islets depth localisation or its volume. However, no correlation could be found (Fig. 4.6). No fluorescent response was measured 4 hours after injection of a blocking solution of 100 μ g of unlabeled exendin-3 (Fig 4.4a,b), confirming the specificity of Cy5.5-exendin-3 for islets of Langerhans.

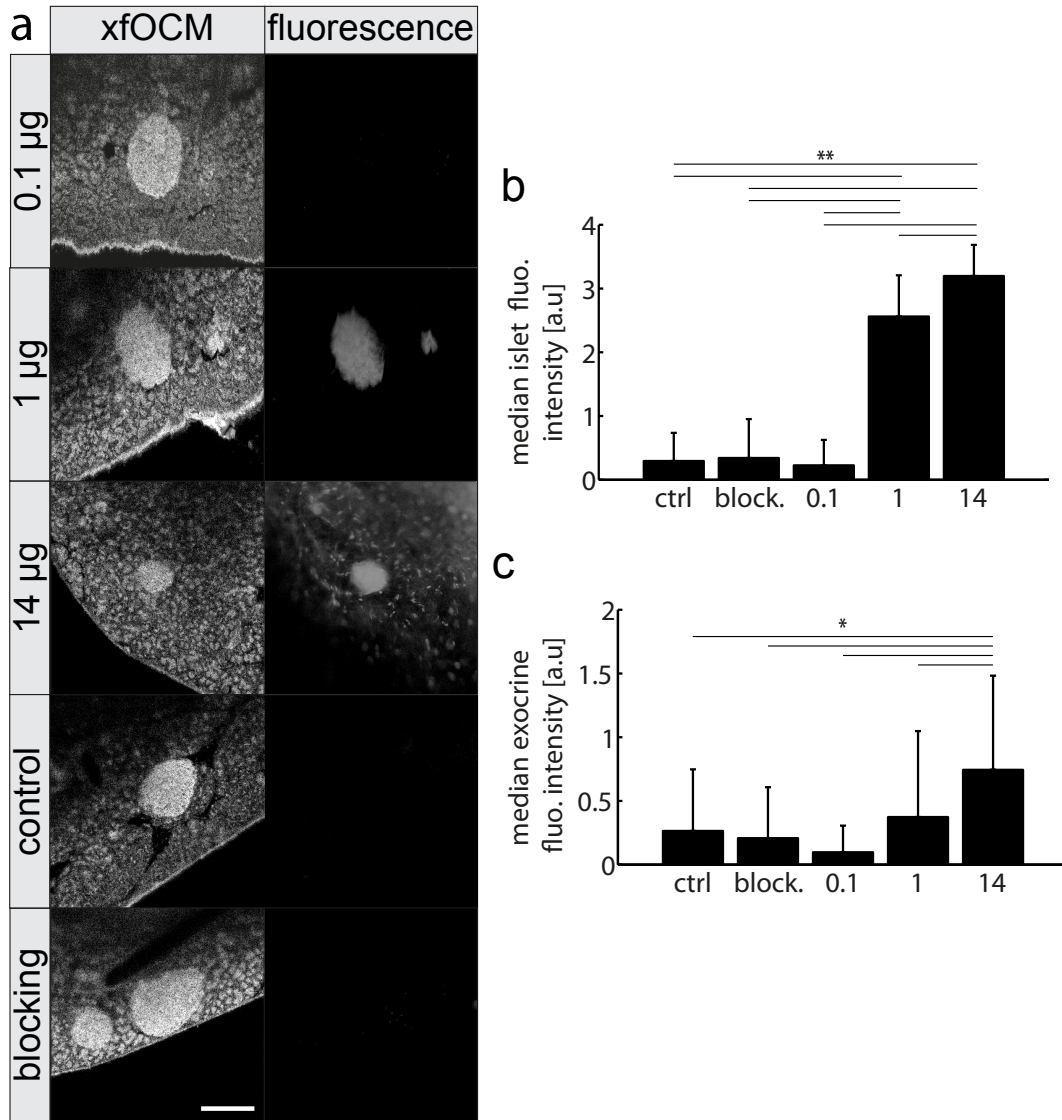


Figure 4.4: **Evaluation of different doses of Cy5.5-exendin-3 *in vivo*.** (a) Representative images of the fluorescence signal and the corresponding xfOCM images 4 hours after injection of different doses of Cy5.5-exendin-3. Scale bar: 200 μ m. (b,c) Quantification of islet fluorescence intensity (b) and exocrine fluorescence intensity (c) 4 hours after injection of different doses of Cy5.5-exendin-3 (0.1, 1, 14 μ g), control (ctrl) and blocking (block.). * $p < 10^{-4}$, ** $p < 10^{-5}$, Mann-Whitney non-parametric U-test.

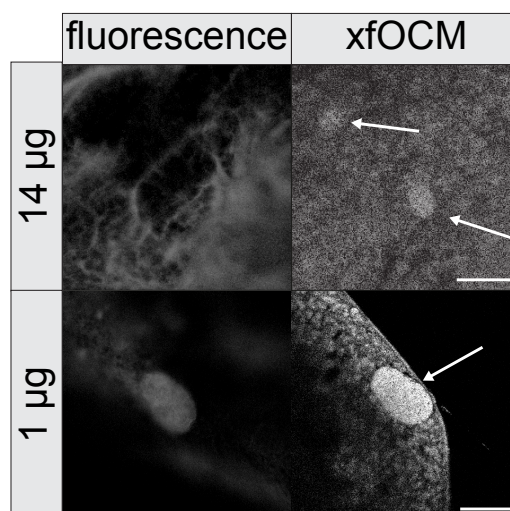


Figure 4.5: **Evaluation of different doses of Cy5.5-exendin-3 *in vivo*.** Fluorescence and corresponding xfOCM image a few minutes after injection of 14 μg or 1 μg of Cy5.5-exendin-3. After injection of 14 μg , the tracer is visible in the vasculature of the pancreas. Arrows indicate islets in the xfOCM image. Scale bar: 200 μm .

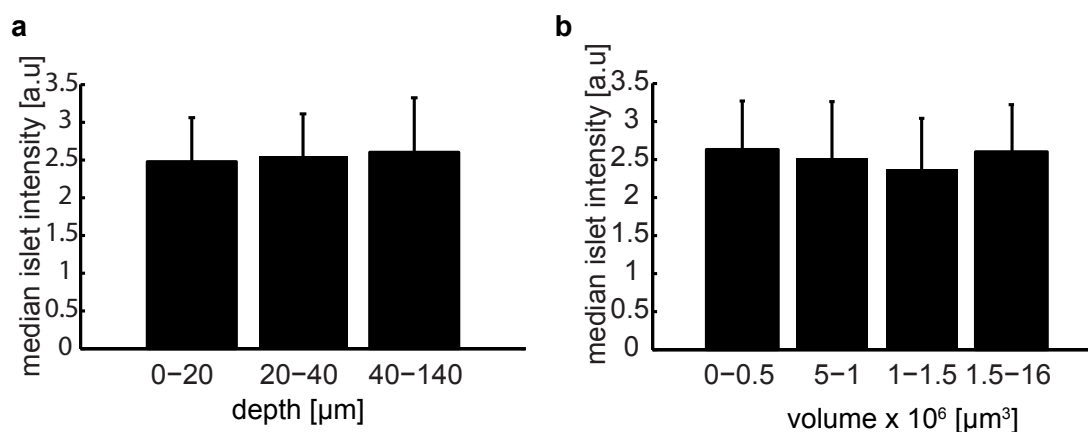


Figure 4.6: **Accumulation of Cy5.5-exendin-3.** Median fluorescence intensity of the islets 4 hours after injection of 1 μg of Cy5.5-exendin-3 with respect to the islet depth position in the tissue (a) or to the islet volume (b).

Chapter 4. OCM and the specificity of β -cell tracers

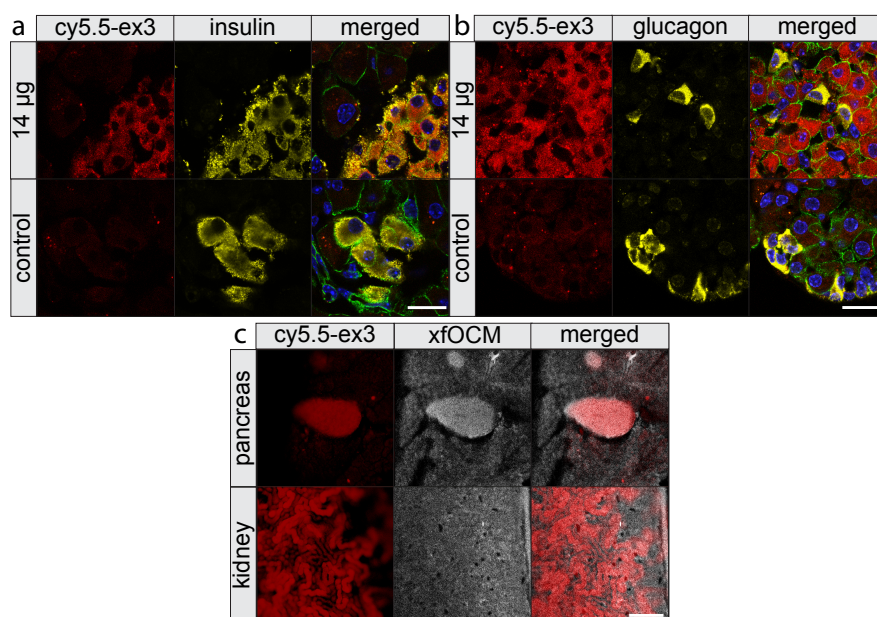


Figure 4.7: **Internalization of Cy5.5-exendin-3.** (a,b) Representative sections showing the internalization of the tracer specifically in β -cells and not in α -cells. E-cadherin staining is shown in green. Scale bar: 20 μ m. (c) *Ex vivo* signal of the tracer is found in pancreatic islet and in the kidneys. The strong fluorescent intensity in the kidney requires using a pinhole to reject out of focus fluorescence. Scale bar: 200 μ m.

***Ex vivo* organ analysis after *in vivo* imaging reveals the specificity of Cy5.5-exendin-3 for β -cells**

To further investigate the specificity of Cy5.5-exendin-3, the pancreata of mice injected with 14 μ g of Cy5.5-exendin-3 or only with PBS were sectioned and stained for insulin, glucagon and e-cadherin (Fig. 4.7a,b) and further analyzed by confocal fluorescence microscopy. This shows that the signal of Cy5.5-exendin-3 is co-localized with the insulin staining and is clearly internalized in β -cells whereas α -cells did not internalize the tracer. No Cy5.5 signal was observed in the control mice injected only with PBS. We performed an *ex vivo* study based on fluorescence imaging for establishing the biodistribution in several organs (heart, lung, duodenum, large intestine, stomach, kidney, spleen and liver). After dissection, a specific Cy5.5-fluorescent signal in the islets is still observable (Fig. 4.7c). Among the organs investigated, only the kidneys showed a strong fluorescent response (Fig. 4.7c) about 2 times higher than the signal observed in the islets (Fig. 4.8), which might cause difficulties for PET/SPECT imaging. In our OCM-fluorescence platform the kidneys and the pancreas are clearly distinguishable: no crosstalk was observed during the *in vivo* assessment.

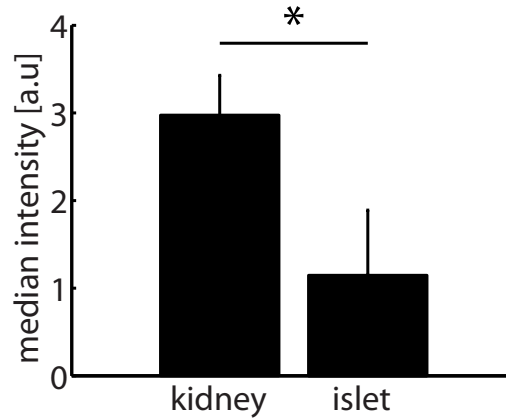


Figure 4.8: Median fluorescent intensity of the islet and kidney *ex vivo* 4 hours after injection of 1 μ g of Cy5.5-exendin-3. $*p < 0.01$ with Mann-Whitney non-parametric U-test.

Cy5.5-exendin-3 targets islets within minutes and is stably detected for hours

We monitored the accumulation of the tracer over time in different islets (Fig. 4.9). No fluorescent signal was detected in islets prior to the ligand injection. Right after injection of the ligand, a signal was visible in the islets and remained stable over 4 hours. Moving red blood cells cause dynamic light scattering, which can be used by OCM for imaging of the pancreas vasculature [189]. This enables a parallel visualization of the tracer, the islet structure and its vasculature with a temporal resolution of $\sim 20 \mu$ s per depth-profile. The full 3D volume ($512 \times 512 \times 512$ voxel) is imaged in less than 10 seconds for structure and in less than 1 minute for vascularization. The islet vascularization was unaltered after a 4 hour imaging session, which is crucial for a proper delivery of the ligand in the islets. Neither the surgical procedure (the pancreas of mice is exteriorized during the imaging session) nor the imaging is disturbing the blood supply in the islets and in the pancreas.

4.2.4 Discussion

The identification of β -cells specific tracers and the characterization of the dose and dynamics of tracer accumulation are mandatory steps on the road towards human non-invasive β -cell imaging. In this paper, we developed and validated an imaging platform well suited for the task of β -cell tracer assessment. As a proof of principle we addressed the specificity of exendin-3 by *in vitro* imaging of cells expressing GLP1R and by *in vivo* imaging of pancreatic islets. Using this OCM platform, we demonstrated that: (1) Cy5.5-exendin-3 is internalized *in vitro* by CHL cells expressing GLP1R; (2) *in vivo* for fluorescence labeled tracer investigations a dose as low as 1 μ g of the tracer is

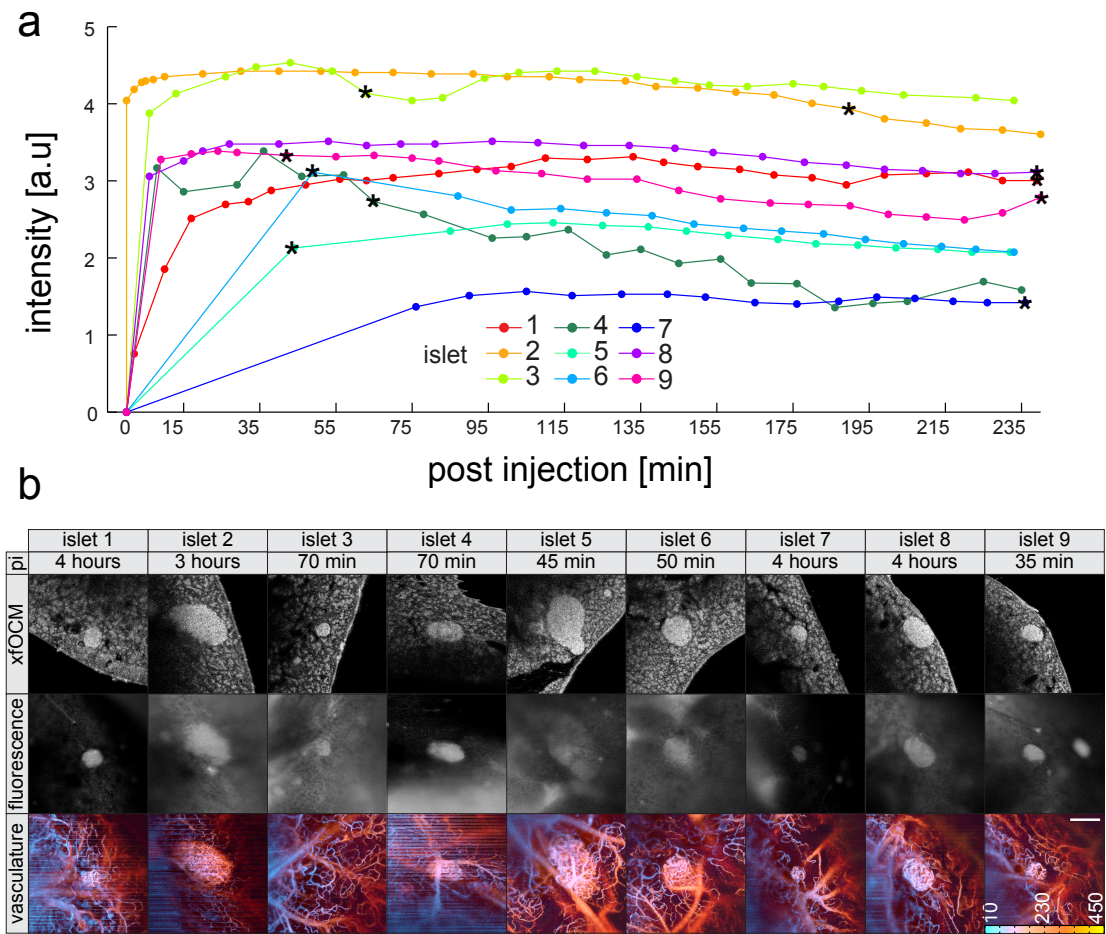


Figure 4.9: **Dynamics of the tracer *in vivo*.** (a) Fluorescence signal detected over time after injection of 1 μ g of Cy5.5-exendin-3. (b) xfOCM (virtual structural section and maximum projection of vascularization) with fluorescence images at different time points indicated with a star symbol in (a). Depth is color-coded in micrometers. Stripes in the vascularization images are due to residual pancreas movements. Scale bar: 200 μ m.

sufficient to be optically detected and quantified inside islets with a sufficient signal ratio discriminating well endocrine and exocrine tissue; (3) *in vivo* the tracer is specifically internalized as confirmed by blocking experiments with an excess of unlabeled exendin-3; (4) the discrimination of pancreatic islets by the fluorescent tracer is obtained already a few minutes after injection and is observable for at least 4 hours. Last but not least, we showed that Cy5.5-exendin-3 is internalized by β -cells but not by α -cells. In contrast to what was suggested by Reiner et al. [230], we show that exendin-3 conjugated with Cy5.5 at the C-terminus lysine in position 40 specifically and efficiently accumulates in CHL cells expressing GLP1R and in the β -cells *in vivo*.

Compared to classical optical fluorescence microscopy applied to image islets of Langerhans, our OCM platform offers several essential advantages: first, 3-dimensional OCM imaging requires only two lateral scans, resulting in a faster acquisition speed; second, no genetically modified mice to image islets of Langerhans are needed; and third, no injection of an external agent is needed to visualize the pancreas vascularization. However, to access the pancreas, a laparotomy and exteriorization of the pancreas are still required, as it is the case for any optical imaging method. A high β -cell tracer detection requires good delivery and therefore demands a well perfused organ. The label-free imaging of the vascularization during the whole imaging session proved to be an essential asset for the assessment of tracer dynamics and accumulation. The artifacts visible in some vascularization images in Fig. 4.9 could be removed by a better stabilization of the pancreas, which remains an experimentally difficult endeavour for small animal imaging. A potential alternative could be the acquisition of additional transversal scan lines to better identify bulk intensity shifts [231] and to discard them.

To assess the specificity of a potential tracer *in vivo*, optical approaches are needed to resolve individual islets and compare their intensity to other neighboring tissues. While islets can be discriminated due their intrinsic higher scattering signal in OCM, a fluorophore is necessary to detect the tracer. This can sometimes modify the binding properties of tracers, a limitation of the technique also shared by confocal imaging and in general by other techniques offering such resolution in space and time. However, the speed of the technique allows to perform live imaging and quantifications of multiple islets in parallel. Previous assessments of dynamics by confocal microscopy have focused on one islet per mouse, which does not enable to assess the variation in signal [217]. We reveal that there is a range of responses, some islets being 3 fold stronger, but all islets reaching a plateau of signal in less than 15 minutes. This variability is averaged in PET/SPECT where the signal results from an integrated signal over multiple islets at different depths. The temporal signal over individual islets is however remarkably stable at the plateau, similar to confocal imaging [217], with little variations due to breathing, heartbeat and peristaltic movements.

Since fluorescence detection is less sensitive than radioactivity detection, we expect differences in the required doses to detect a signal when fluorescence microscopy is

Chapter 4. OCM and the specificity of β -cell tracers

used compared to PET/SPECT modalities. Our dose escalation study allows a better understanding of the differences in dosing between fluorescent tracers [217, 221] and radio-tracers [213, 224]. We confirmed that a fluorescence signal is detectable both at 14 μ g and 1 μ g similarly to other studies based on fluorescence detection of the tracer [217, 221]. Of note, the 1 μ g dose is lower than the doses previously used for confocal microscopy in mouse (2-8 nmol/10-40 μ g per animal) but higher than the pharmacologic doses administered in human (5 μ g Exenatid per injection). In human imaging, the greater sensitivity of PET will enable to use lower doses as PET/SPECT imaging in mouse only requires around 0.1 μ g per animal [211, 213, 220]. At this dose, no signal is detected in fluorescence, however, similarly to what is observed in PET/SPECT we observed that increased doses result in a decrease of the relative uptake: a 14 μ g dose results in a lower target to background when compared to a dose of 1 μ g of Cy5.5-exendin-3. It is likely that at 14 μ g, we increase the background. In agreement with the biodistribution observed in PET/SPECT a high kidney retention of the tracer was detected.

The presented imaging technology provides a rapid assessment of tracer characteristics *in vivo* complementing the tedious classical *ex vivo* procedures based on elaborate single time point biodistribution, autoradiography and immunohistochemistry experiments. Our optical imaging platform provides the basis for an efficient and exact *in vivo* dynamic characterization of β -cell tracer close to the cellular level. Thereby, it offers the possibility to simplify the initial screening to determine whether a potential tracer is specific for β -cells. Nevertheless, since the tracer detection relies on fluorescence, studies using PET/SPECT to image radio-labeled tracer injected in small rodents are required to determine the suitable dose for clinical imaging. Furthermore, the intrinsic contrast of islets and their vascularization opens the possibility to perform a label-free study during diabetes progression. In conclusion, this dual-modality imaging allows *in vivo* monitoring of islet structure, vascularization and tracer uptake for pancreas imaging. As shown, our approach is a preclinical and complementary imaging method to MRI/PET/SPECT to characterize β -cell tracers in mice when the tracer is large enough to be coupled to fluorescent probes.

Author contributions

C.B., L.J., M.B., M.G., A.G-B and T.L. designed the research. C.B, L.J and S.E. performed research and analyzed data. C.P., A.B., D.S., A.L. and M.G contributed new reagents-analytic tools. C.B. wrote the manuscript. All authors reviewed and edited the manuscript. T.L. is the guarantor of this work and, as such, had full access to all the data in the study and takes responsibility for the integrity of the data and the accuracy of the data analysis. The authors declare no conflict of interest.

Acknowledgements

We thank Janne Lehtonen (Novo Nordisk, Malov, Denmark) for the fixation protocol allowing the detection of the injected Cy5.5-exendin-3 on pancreatic cryosections.

Funding

This work was supported by the BetaImage project (EU FP7 222980) and by the Swiss National Science Foundation Grant (20320L-150191). The research leading to these results has received funding from the People Programme (Marie Curie Actions) of the European Union's Seventh Framework Programme FP7/2007-2013/ under REA grant agreement n° 289932. D. Szlag acknowledges support from the SCIEX-NMSch grant.

5 Label-free longitudinal study of type I diabetes

In previous chapters, the feasibility of using OCM to image islets of Langerhans and their vascularization has been demonstrated. Yet, while imaging islets of Langerhans is very important, the most prominent advantage of OCM is its potential for studying the etiology of diabetes. Transversal studies can bring significant information about the progression of the disease. However, in the case of diabetes, the heterogeneity of the progression renders such studies difficult to interpret. On top of that, even in the internalization of tracers, we have seen that there are significant variabilities between islets of different individuals, but also between different islets from the same pancreas (Chapter 4). Therefore, longitudinal studies of individual islets are required. Longitudinal imaging in the pancreas with OCM is in principle feasible, but it is prohibitively difficult to find the same islet between successive imaging sessions. In addition, the heavy surgery required by such studies prevents multiple time point imaging. The anterior chamber of the eye (ACE) transplantation model offers the opportunity to follow individual islets over time. In this chapter, we developed a platform combining OCM with the ACE transplantation model. We also identified the Zn^{2+} -insulin crystalline structures as the main source of the strong back-scattering of the β -cells. In this context, OCM allows a complete label-free non-invasive imaging of the islets with a molecular specificity for β -cells.

5.1 Journal article

Manuscript in preparation

Functional optical coherence imaging (FOCI)—A novel, label-free approach for longitudinal, 3D visualization of autoimmune diabetes

Corinne Berclaz^{1*}, Anja Schmidt-Christensen^{2*}, Daniel Szlag^{1,3*}, Jerome Extermann^{1,4}, Lisbeth Hansen², Arno Bouwens¹, Martin Villiger¹, Joan Goulley⁵, Frans Schuit⁶, Anne Grapin-Botton^{5,7}, Theo Lasser¹, and Dan Holmberg²

¹Laboratoire d'Optique Biomédicale, Ecole Polytechnique Fédérale de Lausanne, CH1015 Lausanne, Switzerland; ²EMV Immunology, BMC, Lund University, 221 00 Lund, Sweden; ³Institute of Physics, Faculty of Physics, Astronomy and Informatics, Nicolaus Copernicus University, Grudziadzka 5, PL-87-100 Torun, Poland; ⁴Hepia, University of Applied Science of Western Switzerland, 4 rue de la prairie, CH-1202 Genève, Switzerland; ⁵Swiss Institute for Experimental Cancer Research, School of Life Sciences, Ecole Polytechnique Fédérale de Lausanne, CH1015 Lausanne, Switzerland; ⁶Gene Expression Unit, Department of Molecular and Cellular Medicine, Katholieke Universiteit Leuven, Leuven, Belgium; ⁷DanStem, University of Copenhagen, 3B Blegdamsvej, DK-2200 Copenhagen N, Denmark; * These authors contributed equally to this work.

Longitudinal high-resolution optical imaging in animal models has provided valuable insight into disease mechanisms. However, many disorders, like type I diabetes, afflict tissues that are difficult to access by optical imaging *in vivo* and *in situ*. We present here a procedure based on optical coherence microscopy (OCM) for label-free quantitative detection of autoimmune inflammation and vascular imaging in pancreatic islets transplanted into the anterior chamber of the eye (ACE). We demonstrate that this method, called functional optical coherence imaging (FOCI), can be applied to longitudinal monitoring of progressive autoimmune insulitis, including the 3-dimensional quantification of β -cell volume, inflammation and vascularization. Applying FOCI to a spontaneous mouse model for type I diabetes, we observe that modifications of the pancreatic microvasculature accompany the progression of diabetes with a strong correlation between increasing insulitis and density of the vascular network of the islet. The label-free nature of FOCI contributes an important asset for transferring this imaging modality to human applications.

5.1.1 Introduction

Diabetes mellitus develops as a functional impairment in the insulin production, sometimes in association with insulin resistance. In both of the major types of diabetes mellitus, the progressive dysfunction of β -cell causes the disease development. However, the underlying mechanisms differ significantly. Thus, while T1D is the result of an autoimmune attack on the β -cells, T2D is considered to be driven by metabolic factors. These factors are associated with sedentary life style and obesity, albeit with accumulating evidence of low-grade inflammation. Modifications of the pancreatic microvasculature are likely to accompany the progression of both T1D and T2D. Alterations in vascular parameters, such as transient vasoconstriction, vasodilation, increased blood flow, and vascular leakage are necessary preludes to inflammation by orchestrating the influx of diverse cell types as well as affecting local homeostasis [52, 169, 232–234]. To fully appreciate how these events contribute to the pathogenesis, improved methodology allowing longitudinal, high-resolution monitoring of cells, vascularization and affected tissues during its natural progression is most warranted.

To date, longitudinal non-invasive, intra-vital imaging of the pancreas has been mainly restricted to non-optical imaging modalities like magnetic resonance imaging (MRI) and computed tomography (CT). While the medical potential of these imaging techniques is indisputable, they are limited by a restricted set of reagents targeting specific tissues and by a relatively low spatial resolution [52, 170, 235]. On the other hand, although the development of optical techniques has improved the resolution as well as the range of targetable tissues, they are mainly based on invasive surgery and with limited possibilities for longitudinal studies [38, 104, 236]. Optical Projection Tomography (OPT) has been used to image the adult mouse pancreas and to retrieve the three-dimensional and undistorted structure of the tissue [105]. While in this case inflammation could be quantified at different stages of the disease [31, 106], it is limited by being an *ex vivo* technique and requiring sample fixation and immunolabeling. In a more recent work, the anterior chamber of the eye (ACE) has been used as a valuable site to study transplanted pancreatic islets [108]. Engrafted on the iris, islets could be repeatedly imaged by using the eye as a natural body window. This minimally invasive approach allows longitudinal monitoring of individual islets by using two-photon fluorescence microscopy in combination with appropriate fluorochromes and transgenic mouse models expressing fluorescent proteins. In addition, it can be used to visualize islet vascularization, β -cell function [13] and autoimmune inflammation [111]. Most optical imaging modalities are based on labeling of specific molecular probes or transgenic expression of tagging molecules. This has resulted in an improved specificity, imaging depth and versatility, supporting the development of live and intravital optical imaging. However, the requirement for administration of labeled reagents or expression of transgenic flagging molecules remains an important obstacle when considering transferring these techniques to the imaging of human tissues and to clinical settings. The previously developed extended-focus optical coherence microscopy (xfOCM) platform [123] (Section 5.2.5 §*xfOCM*) circumvents many

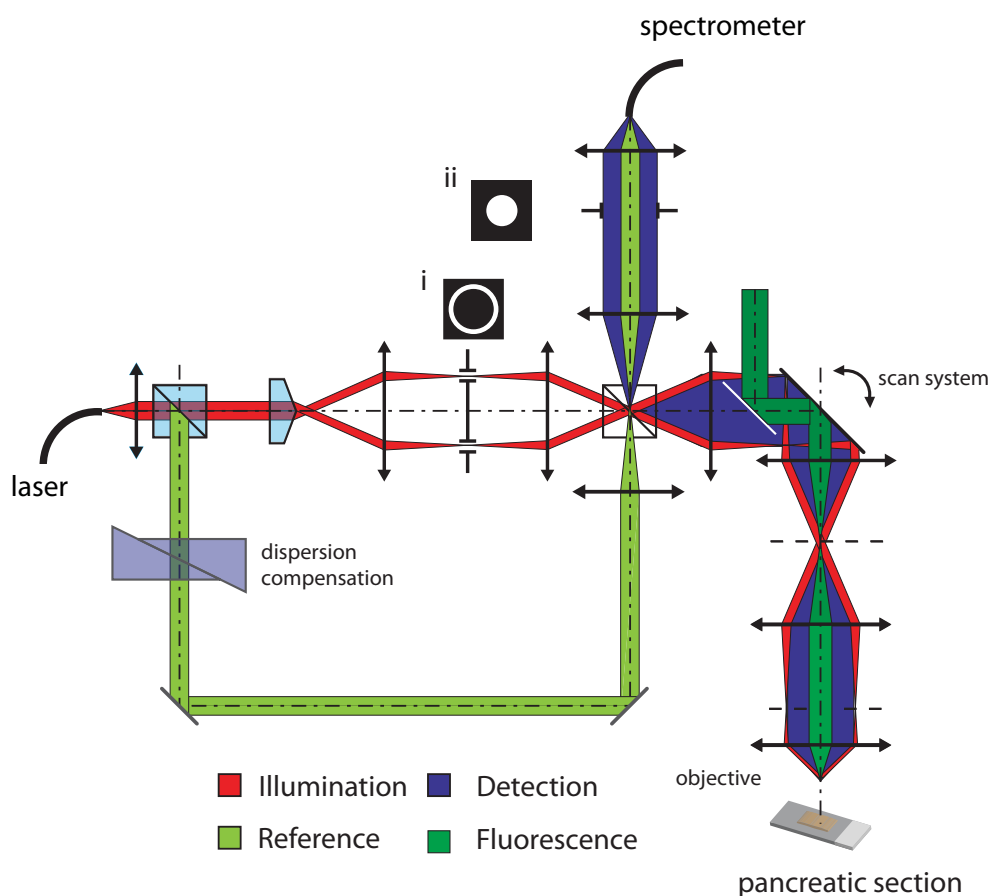


Figure 5.1: **Schematic layout of the instrument used to image fixed sample.** Acquisition of OCM and confocal fluorescence signal is done simultaneously. A dark-field effect is obtained by adding an annular mask (**i**) in the illumination and a pupil mask (**ii**) in the detection arm to remove the strong reflection of the coverslip.

of these hurdles, allowing for label-free visualization of pancreatic lobules, ducts, blood vessels and individual islets of Langerhans *ex vivo* and *in vivo*. So far, this technique has been restricted to visualizing individual islet and snapshots of islet distribution [107, 161]. Here, we introduce a new technique named functional optical coherence imaging (FOCI) to longitudinally image pancreatic islets transplanted into the ACE. We demonstrate that this imaging technique can, in a label-free manner, directly and specifically quantify the functional volume of β -cells. Further, using this approach, we longitudinally quantify alterations in the structure and vasculature during the progressing autoimmune attack of the pancreatic islets. We demonstrate how the vessel bed in the islets is remodeled during the inflammatory process, resulting in a significantly less dense network in infiltrated areas. We anticipate this technique to be adoptable to other tissues and organs that require accurate spatial, temporal and quantitative analyses of their structure and vasculature.

5.1.2 Results

β -cell specificity in OCM

In general, contrast in xfOCM is based on the scattering characteristics of the investigated tissue. Therefore, these coherent imaging methods do not provide a specific contrast. However, knowing the morphology of islets of Langerhans and β -cells, the contrast difference between exocrine and endocrine tissue becomes an intriguing question. We have previously shown that xfOCM imaging can be used to identify pancreatic islets in surgically exposed pancreases of live animals and that the strong scattering observed in the pancreas correlates with insulin producing β -cells [107]. Pancreatic β -cells contain a high zinc content [237]. Since OCM is sensitive to changes of refractive index, we hypothesized that the origin of the strong β -cell OCM signal is due to the zinc-insulin crystals made of hexamers of six insulin molecules with two Zn^{2+} ions stored inside the secretory vesicles. To test this hypothesis, thick pancreas sections of zinc transporter 8 (ZnT8) knockout mice, which lack zinc-insulin crystals in the secretory granules of β -cells [238] were subjected to immunohistochemical (IHC) analysis using anti-insulin antibody and analyzed simultaneously by OCM and confocal fluorescence microscopy. In order to suppress the specular reflection of the coverslip, we used a dark-field OCM (dfOCM) configuration extended with a confocal fluorescence channel (Fig. 5.1). Figure 5.2 shows transverse virtual sections at selected depth position of dfOCM stack and the corresponding fluorescence images.

While control pancreata showed a good correlation between dfOCM and insulin staining (Fig. 5.2a), the dfOCM signal in the ZnT8-KO mouse pancreata was significantly diminished (Fig. 5.2b,d), indicating that zinc within β -cells contributes to the OCM signal. To investigate this further, we imaged the pancreas of guinea pigs as they have a divergent insulin unable to form the hexameric crystals with zinc [239]. Therefore, β -cells in guinea pigs contain both insulin and zinc, but do not store insulin as zinc-insulin crystals. Guinea pig's β -cells did not show a strong scattering in dfOCM image (Fig. 5.2c,d). Together, these data identify the crystal of insulin with zinc to be the dominant scattering contribution in OCM and demonstrate that this label-free approach provides a high specific contrast for the functional β -cell volume.

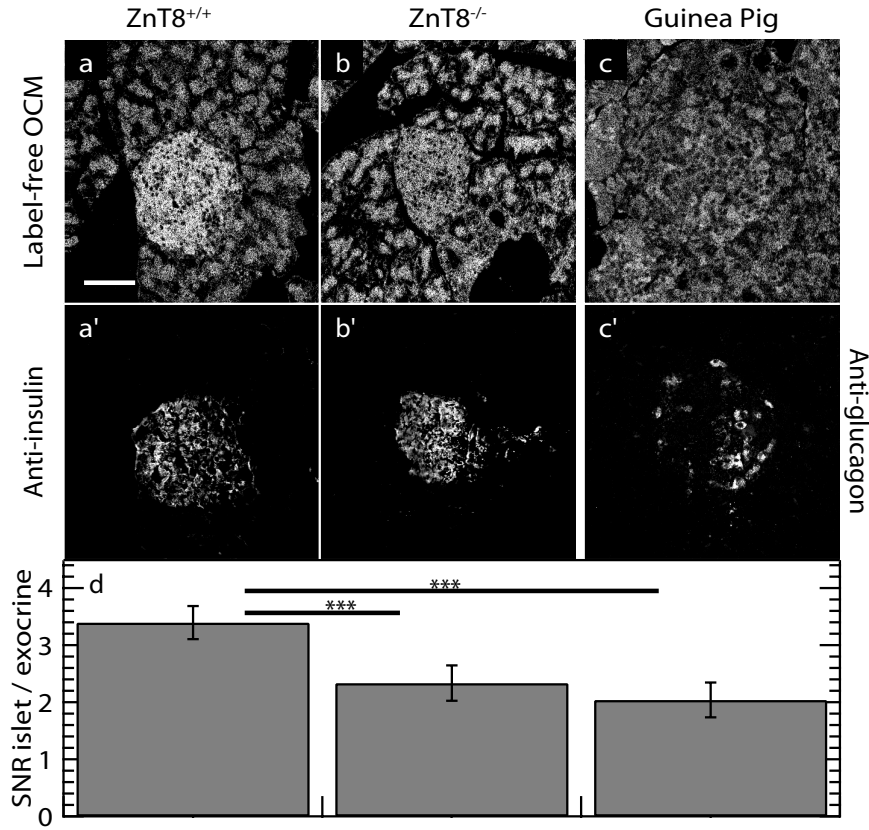


Figure 5.2: **Ex vivo dfOCM imaging of pancreas and β -cell specificity of the OCM signal.** Thick pancreas sections of ZnT8^{+/+} wildtype controls (a,a') or ZnT8^{-/-} mice lacking the insulin secretory granule (b,b') or guinea pig (c,c') were analyzed by IHC for specific fluorescence labeling of pancreatic islets with anti-insulin (a',b') or anti-glucagon (c') antibodies. Scale bar: 50 μ m. The sections were imaged by dfOCM extended with a confocal fluorescent channel. Representative images were chosen. (d) Raw data images were analyzed for signal to noise ratio (SNR) between the islets and the exocrine pancreas (n=50-60 islets per group). *** $p < 10^{-13}$ analyzed by a Mann-Whitney non-parametric U-test.

Longitudinal quantification of β -cell volume and islet vascularization using FOCI

Having established that the xfOCM signal specifically reflects the β -cell volume, we aimed next to apply this technique to longitudinal studies. While longitudinal imaging of the pancreas is feasible, it requires heavy laparoscopy and it is almost impossible to locate the same islet at successive imaging sessions. To overcome these caveats, we combined xfOCM with a longitudinal imaging platform to establish FOCI (Fig. 5.3).

Isolated, syngeneic islets were transplanted into the ACE of healthy mice. The islets were then repeatedly imaged by FOCI post transplantation. As illustrated in Figure 5.4a-d and 5.4e, islets were found to grow during the course of the study. Our data extend previous reports, which have shown that after an initial phase of vascularization, syngeneic islets transplanted into the ACE are sustained and functional over several months [108, 109]. The FOCI technology allows, unlike other optical techniques, for label-free 3D imaging of the vasculature network (Sections 5.2.5 to 5.2.7).

Taking advantage of this, we visualized and quantified the microvasculature in the transplanted islets over a 2 month period. As illustrated in Figure 5.4a-d and 5.4f, we found that in parallel with islet growth, re-vascularization of the grafted islet occurred rapidly over the first 2 weeks after transplantation to form a capillary network similar to that in native islets *in situ* (Fig. 5.5a).

Foci detects inflammation in pancreatic islets under autoimmune attack

We next applied FOCI to follow the progressive autoimmune destruction of β -cells in the NOD mouse model for T1D. NOD mice spontaneously develop insulitis from 3-4 weeks of age, which progressively increases and eventually leads to the destruction of most of the β -cell mass and to overt diabetes. We have previously reported that ACE-transplanted islets in the NOD genetic background are subject to a progressive insulitis and β -cell destruction mimicking the process seen in the NOD pancreas [111]. To determine if the inflammatory cells infiltrating the ACE-transplanted islets could be visualized in a label-free manner using FOCI, we next analyzed 14-week-old nondiabetic NOD mice that have been ACE-transplanted with syngeneic islets 4 weeks prior analysis.

As reported previously [111] and shown in Figure 5.6, NOD reporter mice can be used to visualize specific inflammatory cellular populations infiltrating the pancreatic islet. In order to interpret the OCM signal *in vivo* during the longitudinal study, we used NOD.Foxp3-GFP reporter mice to visualize the recruitment and accumulation of Foxp3⁺ regulatory T-cells to the site of inflammation along with other inflammatory leukocytes in the islet. The strong GFP signal indicating inflammation in the NOD islets (Fig. 5.6b), but not in B6.Foxp3-GFP recipient mice (Fig. 5.6h) matches completely the low FOCI signal in the center of the NOD islet. This supports the notion that this approach could be used to discriminate the β -cell volume from the infiltrated volume (Fig. 5.6c,e, and

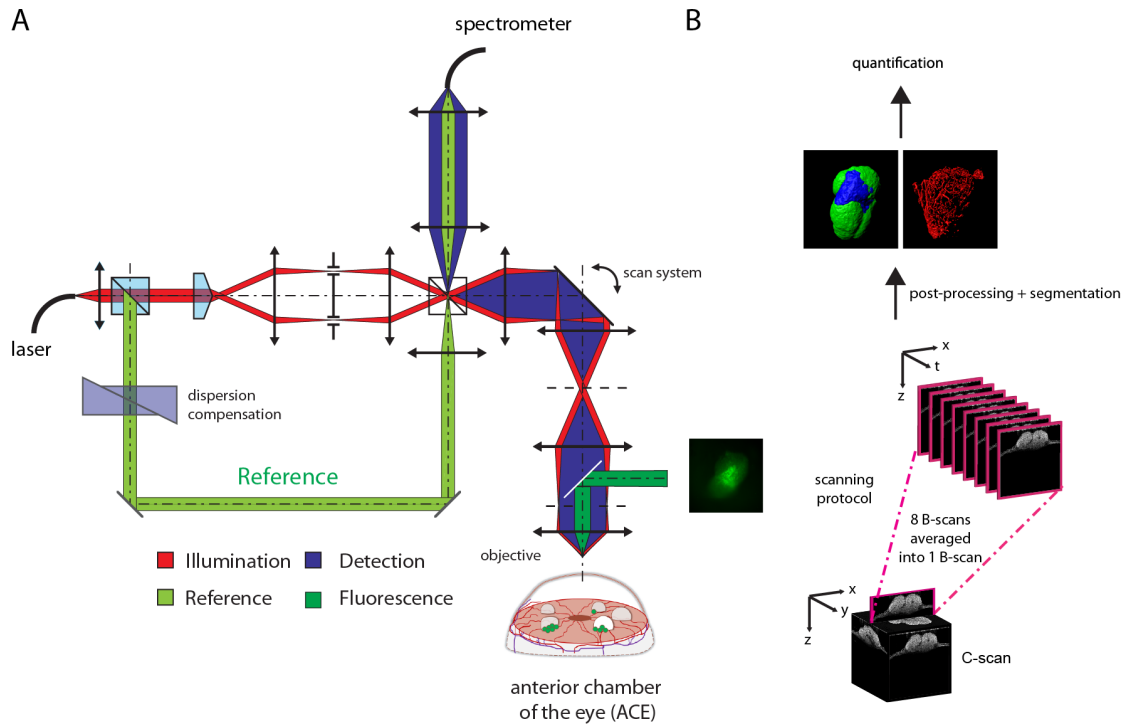


Figure 5.3: **Schematic layout of the instrument and processing used to image the ACE transplanted islets.** (a) Dual system combining fluorescent widefield microscopy and xfOCM. (b) Overview of the scanning protocol and image analysis.

Fig. 5.7). B6 control mice did not show such alteration in the FOCI signal (Fig. 5.6j). To confirm this, the mice were sacrificed after imaging and submitted to conventional immunohistochemical (IHC) analysis of the grafted islet. As illustrated in Figure 5.6f,e and Figure 5.8, the insulin staining matched the segmented OCM brighter signal, while the part in OCM with a significantly lower OCM signal corresponds to the area stained positive with a pan-leukocyte marker. These findings confirm that FOCI can detect inflammation in addition to the β -cell volume. However, while the high OCM signal is specific to insulin, the lower OCM signal cannot be solely attributed to infiltration. Indeed, other non- β endocrine cells and vessels also give weaker scattering. To estimate to which extent the other endocrine cells and vessels contribute to the non β -cell volume in inflamed islets, we quantified the non β -cell volume in non-inflamed healthy wild type islets. After initial fluctuations shortly after transplantation, the non β -cell volume remained stable with approximately 3% of the total islet volume (Fig. 5.9), which coincides with stabilization of islet vascular network after transplantation. To confirm that the insulinitis identified in the ACE transplanted NOD islets could be similarly detected by FOCI in the pancreas, we next analyzed images of surgically exposed pancreas from aged non-diabetic NOD mice. As illustrated in Figure 5.5b-d, we observed alterations in the refractory pattern of some of the imaged NOD islets, but not in control B6 mice (Fig. 5.5a). This FOCI signal was lower than the signal detected in β -cells and different

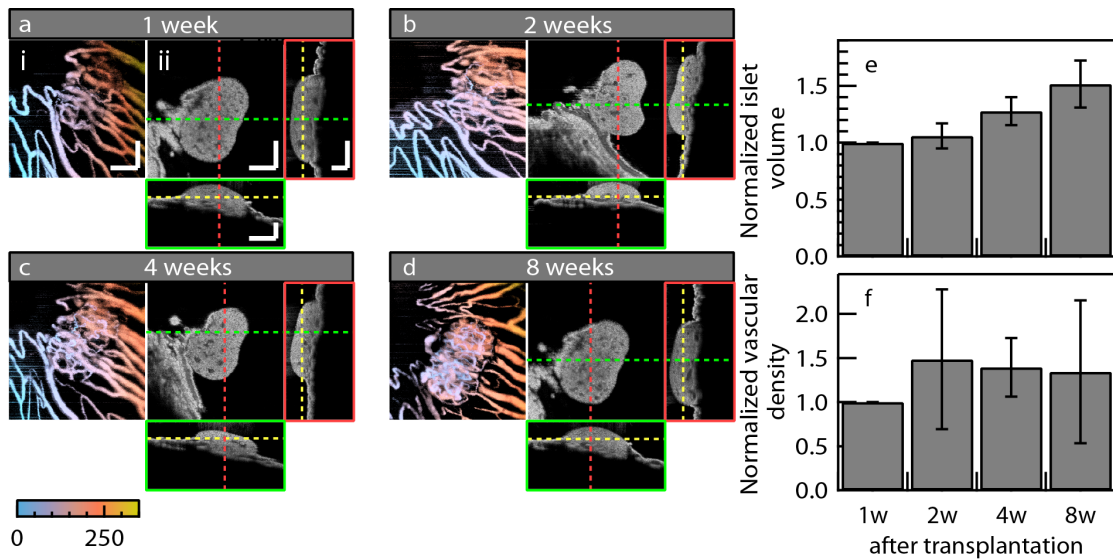


Figure 5.4: **Longitudinal imaging of ACE-transplanted islets by FOCI and quantification of β -cell volume and islet vascularization in healthy state.** Pancreatic islets were transplanted into the ACE of healthy wild type mice (n=4) and imaged repetitively by FOCI 1 week (w), 2w, 4w and 8w post transplantation. (a-d) Representative maximum projection of the vascularization (i) and orthogonal view of the islet structure (ii) at indicated time points post transplantation. (e) Islet volume over time normalized to the first time point. (f) Islet vascular density (total vessel volume / total islet volume) over time normalized to the first time point. (e,f) 5-12 islets were analyzed for each time point. Scale bar: 100 μ m, colorbar indicates depth position in micrometers.

from the signal detected in the exocrine tissue. These images potentially reflect insulinitis spanning from unaffected to peri-islet infiltration and full-blown intra-islet infiltration. We confirmed that this altered refractory pattern co-localizes with inflammation, by imaging thick sections of NOD mice stained with a pan-leukocyte marker (Fig. 5.10).

Insulinitis correlates with attenuated vascularization density

Using the FOCI technology we next monitored the vascular network of the islets longitudinally during progressive inflammation (Fig. 5.11). For this, 14-week-old recipient mice with an ongoing autoimmune process were used, expecting that the insulinitis in the ACE-transplanted islets of those mice would progress rather rapidly. As expected, Foxp3-GFP⁺-cells along with other inflammatory cells get recruited to the islet graft and accumulate over time (Fig. 5.11aii), resulting in continuous β -cell destruction. This is clearly distinguishable in the orthogonal FOCI view (Fig. 5.11ai), which was quantified (Fig. 5.11d) and shown in a 3D representation (Fig. 5.11b).

As expected, we could visualize a gradual increase in the total islet vascular network shortly after transplantation (Fig. 5.12). Counterintuitively, we noted a decrease in the

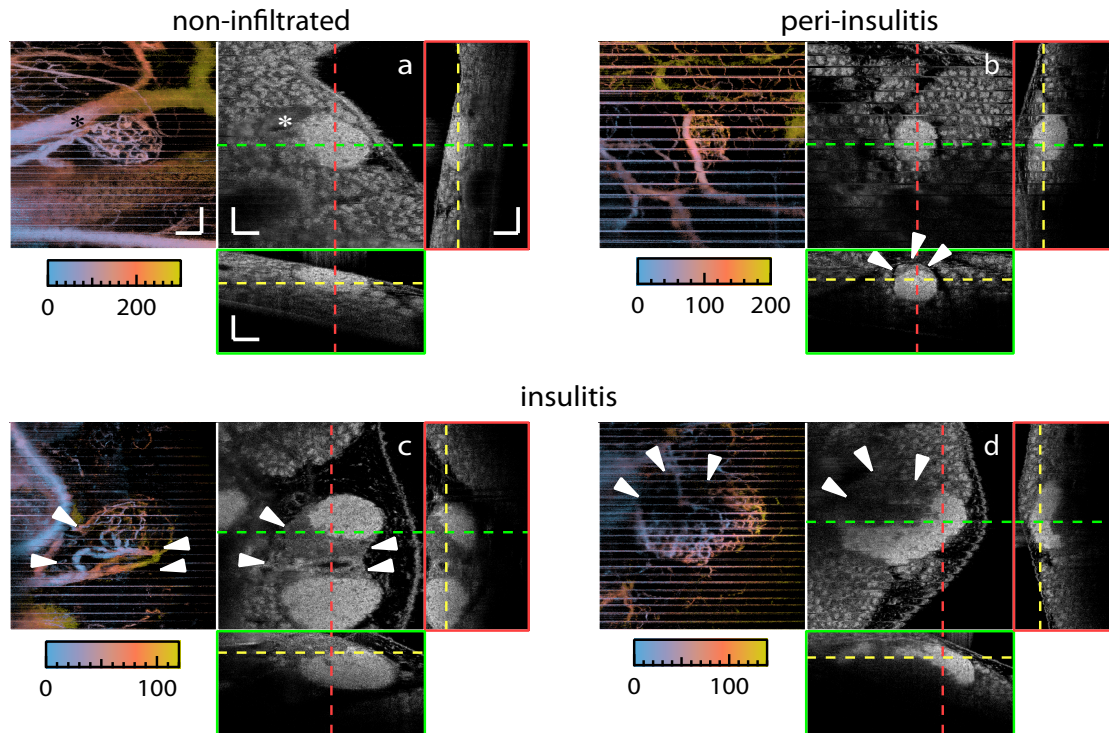


Figure 5.5: **OCM imaging of mouse pancreas.** Pancreas of B6.Foxp3-GFP control mice (**a**) or pre-diabetic NOD.Foxp3-GFP mice (**b,d**) were surgically exposed and subjected to live xfOCM imaging after laparoscopy. Shown are maximum projection in depth of the vascularization and the orthogonal view of virtual sections of a three-dimensional stack of a non-inflamed control islet (**a**), an islet with peri-insulitis (**b**) and fully inflamed islets with insulitis (**c-d**). Asterisk in (**a**) indicates a blood vessel, arrows indicate inflammation. Scale bar 100 μm . Colorbars indicate depth position in micrometers. Residual stripes in the vascularization images are due to residual pancreas movements.

microvasculature density in infiltrated regions of inflamed islets with eventually only few big vessels remaining (Fig. 5.11aiii and e, Fig. 5.6d). This was not observed in islets displaying only limited infiltration (Fig. 5.12 and 5.13). This indicates that the observed attenuation of microvasculature is correlated with the severity of inflammation. Additionally, an attenuation of the microvascular network was also observed in the inflamed islets imaged *in situ* in the surgically exposed pancreas (Fig. 5.5c-d), but not in control B6 mice *in situ* (Fig. 5.5a) or B6 islet grafts in the ACE (Fig. 5.4 and 5.6k).

To rule out that the regression of microvasculature observed by FOCI is caused by a signal loss due to reduced blood flow speed, we used IHC to analyze sections of pancreatic islets from aged non-diabetic NOD.Foxp3-GFP mice or ACE-transplanted islets from the same mice (4 weeks post-transplantation). In this way, we could confirm that vessel density, as revealed by anti-CD31, was decreased in inflamed areas compared with non-affected areas of the islets in the pancreas (Fig. 5.14a-c). In contrast, high endothelial venules

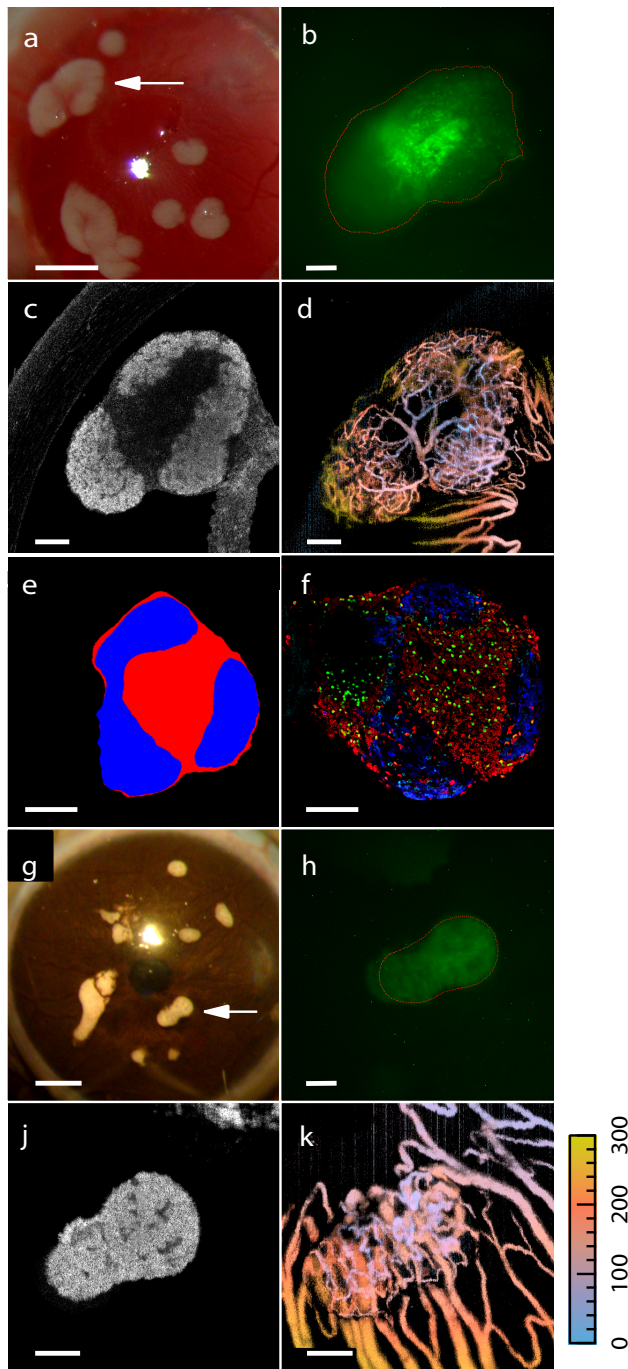


Figure 5.6: FOCI detects inflammation in ACE-transplanted islets affected by insulinitis. Pancreatic islets have been transplanted into the ACE of 10-week-old NOD.Foxp3-GFP recipients ($n=12$) with ongoing autoimmune inflammation (**a-f**) or healthy B6.Foxp3-GFP control mice (**g-k**) ($n=2$) and imaged by FOCI weekly post transplantation. Shown is one representative imaging session at 4 weeks (**a-f**) or 5 weeks (**g-k**) after transplantation. (**a,g**) Widefield microscopy images of the recipient mouse eye engrafted with islets on the iris. (**b,h**) Fluorescent widefield microscopy showing recruitment of Foxp3-GFP⁺ T-cells in the islet indicated by an arrow in NOD recipients (**a**) but not in B6 control mice (**g**). (**c,j**) FOCI virtual section of the engrafted islet. (**d,k**) FOCI maximum depth projection of the vascularization. (**e**) Virtual FOCI section segmented for β -cell (blue) and inflammation (red). (**f**) Cryosection of the graft-bearing eye ($n=7$) at imaging endpoint stained with antibodies specific for insulin (blue) and pan-leukocyte marker CD45 (red), GFP signal (Foxp3⁺ T-cells) is shown in green. Scale bar: 100 μ m; except for (**a,g**) scale bar: 500 μ m. Colorbar indicates depth position in micrometers in (**d**) and (**k**).

Figure 5.7: **Intensity plot through an inflamed islet graft in the eye.** Virtual OCM section of an ACE-transplanted islet and plot of the intensity along the yellow line show the difference of intensity between the insulin OCM signal and the infiltrated OCM signal. Scale bar: 100 μm .

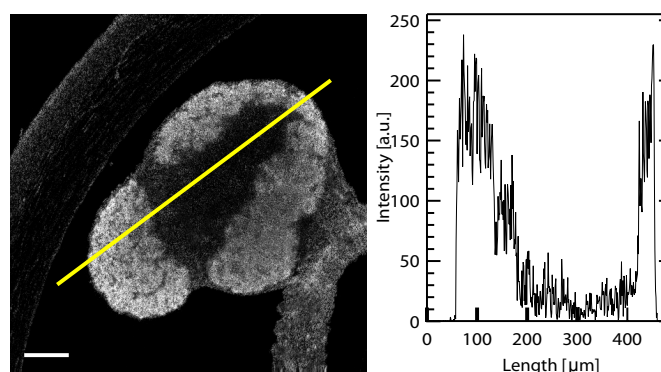


Figure 5.8: **Comparison between OCM signal and IHC.** (a,c) Virtual section of the segmented OCM signal from inflamed islet grafts in the eye (blue: insulin, red: infiltration). (b,d) corresponding IHC after fixation and immunolabeling of cryo-sections of the graft-bearing eye (blue: insulin, red: pan-leukocyte marker CD45, cyan: glucagon, green: Foxp3⁺-GFP-cells). Scale bar: 50 μm .

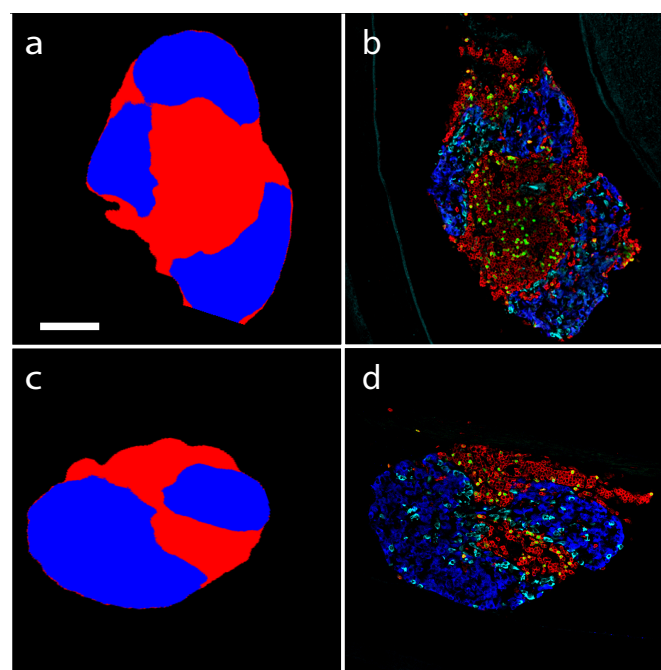
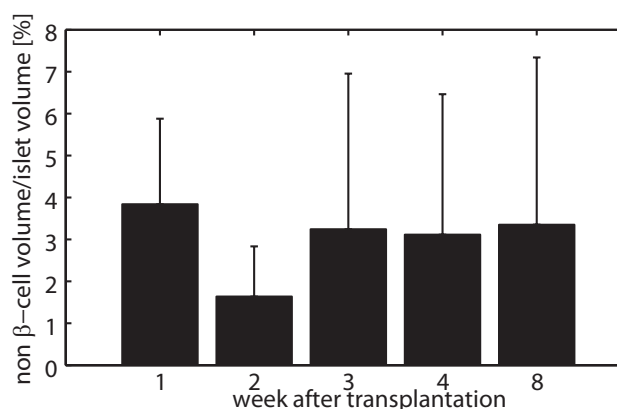


Figure 5.9: **Percentage of the non β -cell volume determined with FOCI in healthy islets grafted into the ACE.** The percentage of non β -cell volume was determined in healthy wild type islets transplanted into the ACE over an imaging period of 1-8 weeks post transplantation. The non β -cell volume was detected by subtracting the β -cell volume from the total islet volume.



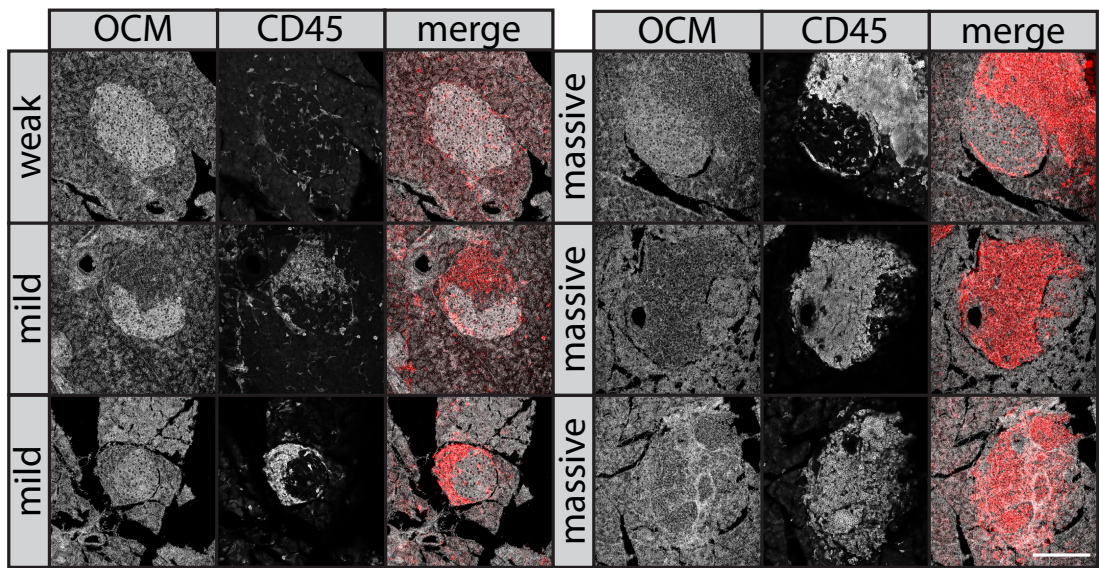


Figure 5.10: **Ex vivo imaging of NOD pancreas.** Thick pancreas sections of NOD.Foxp3-GFP mice were analyzed by IHC for specific fluorescence labeling of the pan-leukocyte marker CD45 to identify inflamed areas. The sections were imaged by dfOCM extended with a confocal fluorescent channel. Representative images show weak, mild or massive inflammation. Scale bar: 100 μm .

(HEV) [240] expressing the mucosal addressin cell adhesion molecule 1 (MAdCAM-1), predominated within inflamed islet areas (Fig. 5.14g-i). This supports previous observations of lymphocyte-HEV recognition in the development of insulitis in NOD mice [31, 241–243]. Interestingly, a similar distribution of CD31^+ versus HEVs was also seen in inflamed ACE transplanted NOD islets (Fig. 5.14d, k). However, MAdCAM-1⁺ HEVs were absent in B6 pancreas (Fig. 5.14e, l) and were also not detected in islet grafts in the ACE of B6 recipient mice (Fig. 5.14f, m).

5.1.3 Discussion

Our label-free 3D-images are based on a next generation Optical Coherence Microscope (OCM), which we named Functional Optical Coherence Imaging (FOCI) for its substantial extension to functional diabetes imaging. As demonstrated, FOCI provided label-free intravital imaging of pancreatic islets with a high specificity for insulin producing β -cells due to the zinc-insulin nanocrystals. The longitudinal recording of the autoimmune induced islets alterations in the ACE provided a detailed monitoring of the decreasing β -cell volume and the impact on the islet vasculature during the inflammatory process. Compared to similar imaging techniques like Optical Coherence Tomography (OCT) [244] or Optical Frequency Domain Imaging (OFDI) [245], FOCI has an almost isotropic resolution over the extended depth range. In comparison to alternative techniques, FOCI

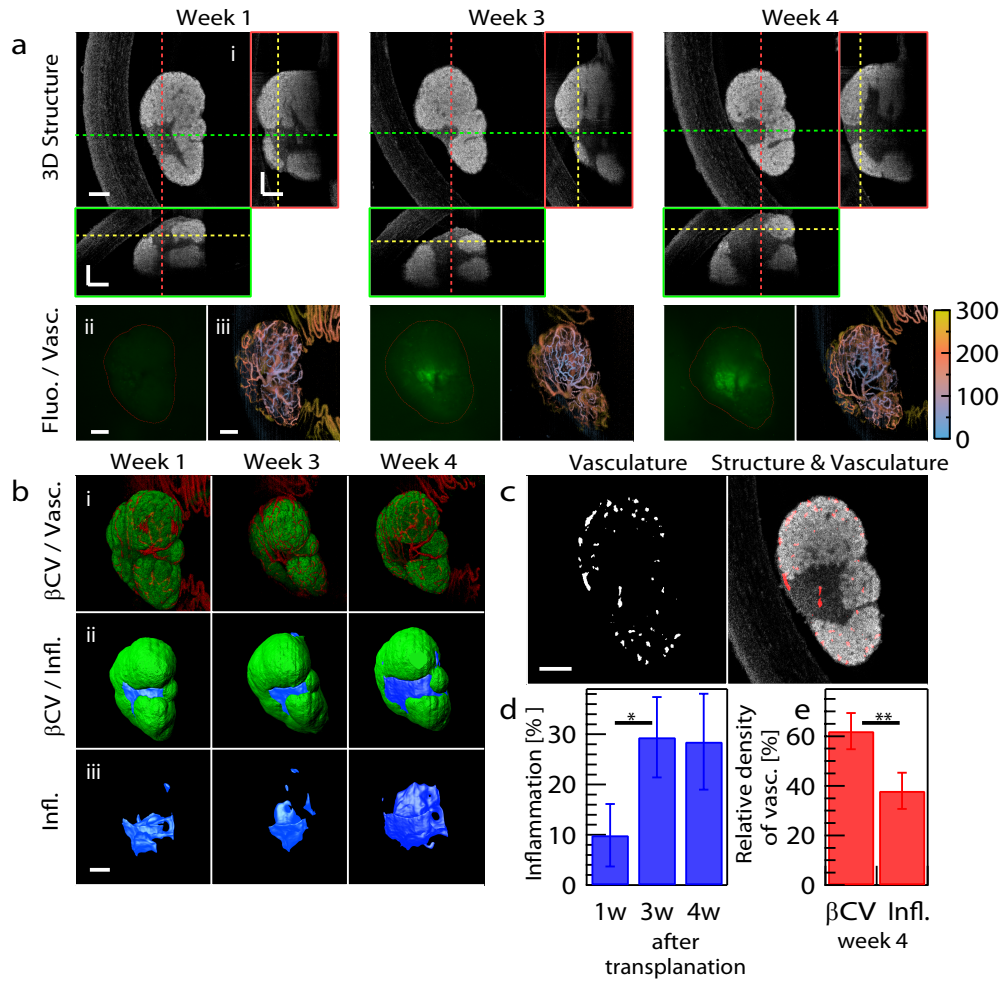


Figure 5.11: Longitudinal quantification of insulitis and the impact on vascularization. Pancreatic islets were transplanted into the ACE of 10 week-old NOD.Foxp3-GFP reporter mice ($n=12$) with ongoing autoimmune inflammation and imaged weekly from 1 week (w) after transplantation. Shown is a longitudinal imaging session of a selected islet at 1w, 3w and 4w after transplantation. **(a)** Orthogonal FOCI view of the islet graft **(ai)** and maximum projection in depth of the vascularization **(aiii)** at week 1-4 after transplantation. Live widefield fluorescence imaging **(aia)** shows the recruitment of Foxp3-GFP⁺ Treg cells to the islet graft in the eye. **(b)** Three-dimensional rendering corresponding to the recording in **(a)**; **(bi)** showing overlay of vasculature (red) and β -cell volume (β CV, green); **(bii)**: segmented β CV (green) and inflammation volume (Infl., blue) or **(biii)** inflammation volume alone. **(c)** Virtual FOCI section of vasculature and overlay of islet structure and vasculature. **(d)** Quantification of Inflammation volume per islet volume over time (in percent), based on 3D rendering in **(b)** ($n=5$ islets each time point), **(e)** Relative density of vascularization (in percent) in inflamed volumes of the islet (Infl.vol., blue in **(b)**) compared to non-affected β -cell volume (β CV, green in **(b)**) at 4 weeks after transplantation, based on 3D rendering as shown in **(b)** ($n=5$ islets), see also Section 5.2.7 § *Volumetric quantification*. Scale bar: 100 μ m, colorbar indicates depth position micrometers in **(a)**. $*p < 0.1$, $**p < 0.01$ were analyzed by a Mann-Whitney non-parametric U-test.

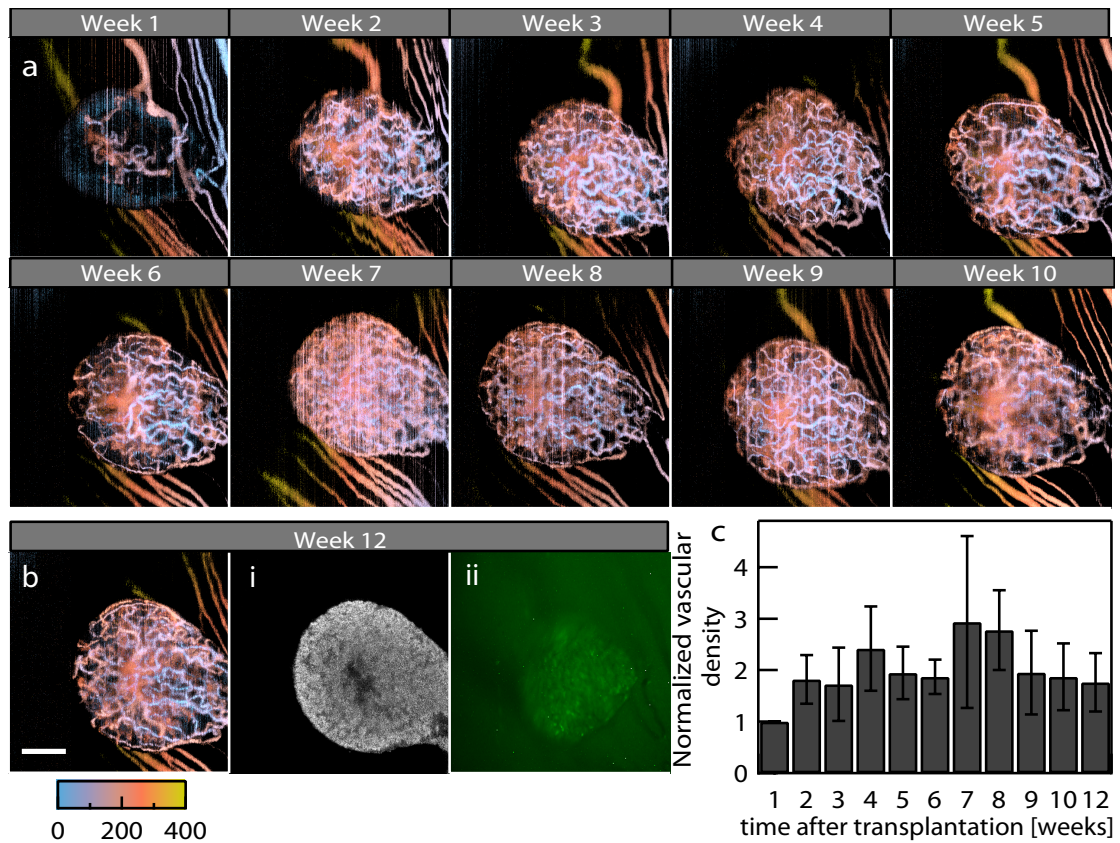


Figure 5.12: Longitudinal imaging of NOD mice with low infiltrated islets after transplantation. NOD.Foxp3-GFP⁺ reporter mice were ACE-transplanted with islets derived from NOD.Rag2^{-/-} mice. The mice were then subjected to non-invasive imaging weekly from day 8 up to 3 months after transplantation. This was done by fluorescent widefield microscopy and FOVI. Islets selected for analysis of vascularization density over time in (c) were chosen based on low GFP signal (Foxp3-GFP⁺ T-cells co-infiltrate islets) and low inflammation in the OCM image post transplantation. (a,b) Maximum projection in depth of the vascularization, depth is color-coded in micrometers. At week 12, a virtual section of the structure (i) and the widefield fluorescence image (ii) shows that the islet was not massively infiltrated and that low GFP signal was detected from the Foxp3-GFP⁺ T-cells. (c) Quantification of the evolution of the islet vessel density (vascular volume/islet volume) normalized by the first week over a timeframe of 1-12 weeks post transplantation (>5 islets analyzed per time point). Scale bar: 100 μ m.

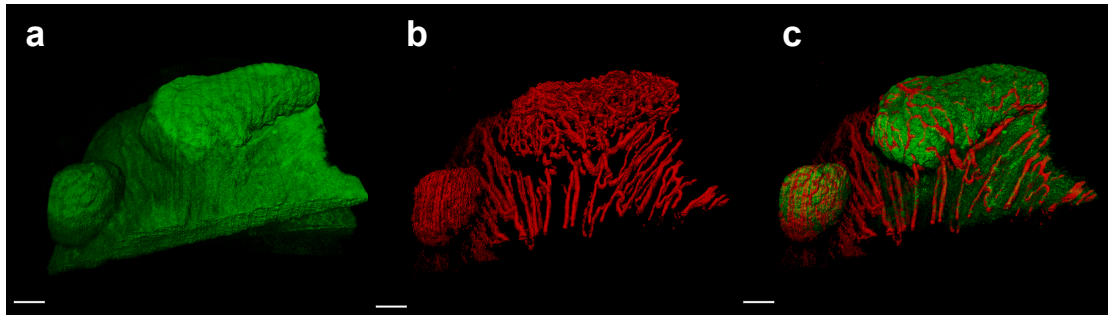


Figure 5.13: **Three-dimensional rendering of FOCI imaged islet engrafted in the eye of a NOD.Foxp3-GFP recipient mouse 5 weeks post transplantation, which did not show massive infiltration.** (a) islet structure, (b) vascularization and (c) thresholded structure to reveal the functional β -cell volume together with vascularization. Scale bar: 100 μ m.

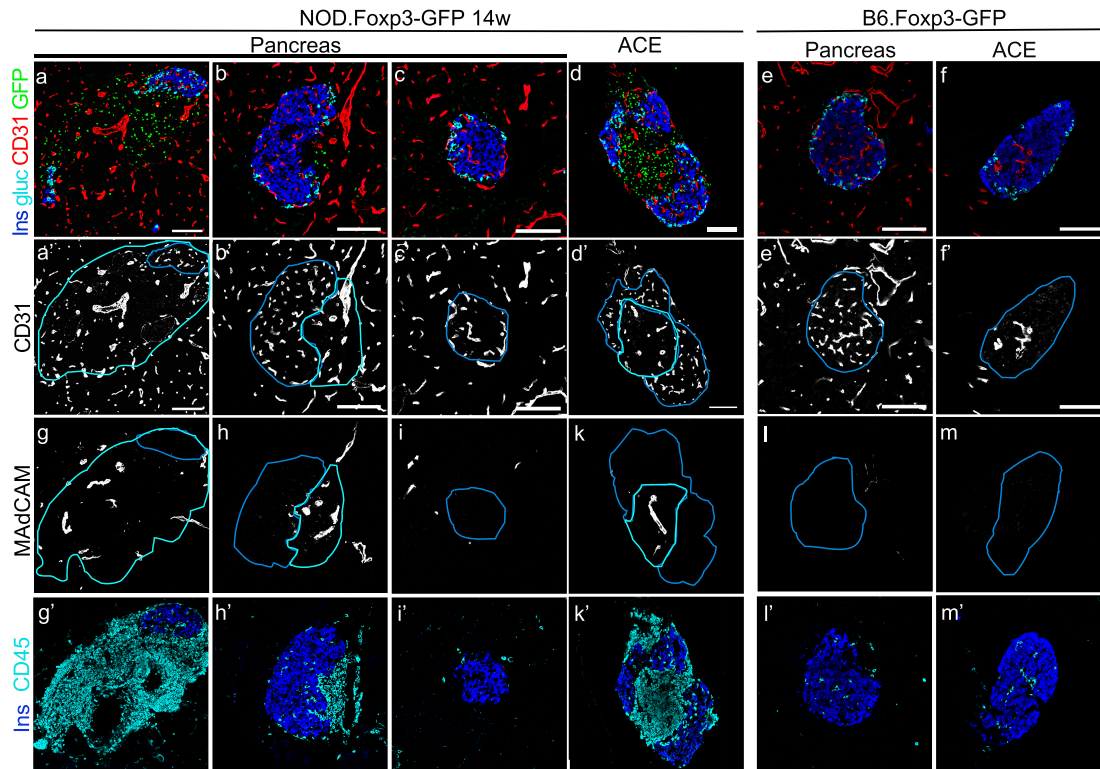


Figure 5.14: **Confirmation of the attenuation of microvasculature in insulitic areas by IHC and the identification of HEVs.** Pancreas and graft-bearing eyes of NOD.Foxp3-GFP reporter mice (14 week old, 4 weeks post-transplantation, $n=7$) (a-d, g-k) or healthy B6.Foxp3-GFP control mice ($n=2$, e,f, l-m) were cryosectioned at imaging endpoint and stained with antibodies specific for insulin (Ins; blue) indicated by blue lines, glucagon (Gluc; cyan in a-f), the vessel marker CD31 (a-f) and MADCAM-1 (g-m) or the pan-leukocyte marker CD45 (cyan) to identify inflamed areas (indicated by cyan-colored lines). GFP signal (Foxp3+ T-cells, first row) is shown in green. Representative images are shown, including the NOD pancreas with coinciding non-infiltrated (c,i), mild insulitis (b,h) and full-blown insulitis (a,g). Scale bar: 100 μ m.

5.1. Journal article

circumvents the need for a voxel per voxel scanning like confocal or multi-photon microscopy, which causes prolonged acquisition times. In addition, the contrast mechanism of FOCI is based on the intrinsic light scattering of tissue and does not require an extrinsic biomarker as for example classical confocal microscopy. The image acquisition of FOCI is based on a broadband NIR light source of around 5 mW on the cornea to acquire a full profile over the extended depth. It represents a substantially lower power exposure compared to two-photon fluorescence microscopy, where the full power is focused at each depth position. This allows long imaging periods without any risk of photo-damage of fragile islet structures and microvasculature. A key obstacle to the early detection of T1DM as well as to the rapid assessment of the effectiveness of therapeutic intervention has been the lack of direct, non-invasive technologies to visualize inflammation in the pancreas. To highlight the usefulness of the FOCI technique applied to the ACE model, we analyzed and compared islets from T1DM prone mice. The location and organization of the pancreas makes the study of this disease at the organ level difficult, requiring compromises on resolution for longitudinal studies in the timescale of disease progression, or end-point analyses. While direct examination of fixed pancreata has yielded valuable insight into the disease processes that lead to diabetes, such an approach only provides a snapshot of the disease. Thus, non-invasive imaging strategies to monitor changes within the islets associated with the development of diabetes are actively being sought to bridge this gap. By applying the FOCI technique, we revealed several features of the disease not previously accounted for. These included the observed diminished vascularization density in areas affected by insulitis, coinciding with the previously reported promotion of MAdCAM expressing HEVs. While the latter has been linked to a promotion of the guidance of lymphocyte trafficking and recruitment to the affected area, the overall reduction in the microvasculature is counterintuitive and remains to be understood in terms of its effect on the pathogenesis.

Impact and future perspectives

In summary, FOCI combined with the ACE model provides a novel and unique instrumentation for investigating functional and structural changes of the pathophysiology in diabetes. It enables the detection of onset and progression of insulitis *in vivo* in real-time, allowing the study of the natural history of the pathological lesions of T1DM in individual animals. We anticipate that this technique will become a powerful tool for the diabetes research community, drug discovery and testing. Especially, the label-free detection of β -cells and infiltration together with vascularization offers unique possibilities to study ACE human islets. However, we foresee that this should be equally true for other complex biological structures in other organ systems or tissues and their disease states. For example, other structures known for important light scattering such as amyloid plaques can be observed in Alzheimer's disease [128] and indicate perfectly the potential of this novel imaging technology.

Acknowledgements

The partly financial support by the Swiss National Science Foundation Grant (20320L-150191) and by the Swedish Research Council is highly acknowledged. D. Szlag acknowledges support from the SCIEX-NMSch grant. We thank Miguel Sison for his help with the dfOCM setup.

AUTHOR CONTRIBUTION A.S.C and L.H performed the islet grafts. C.B, J.E., A.B. and D.S performed the FOCI imaging. A.S.C performed and analyzed the immunohistochemistry experiments. D.S implemented the vascularization segmentation. C.B. performed the analysis and quantification of the FOCI images. C.B, J.E, J.G, M.V, A.G.B and F.S were involved in the Znt8 and guinea pigs experiments. C.B, A.S.C., D.S., J.E, T.L and D.H designed the experiment and wrote the manuscript. D.H and T.L initiated and supervised the project.

5.2 Material and Methods

5.2.1 Animals

B6 Rag2^{-/-} mice were backcrossed to NOD mice for the generation of NOD Rag2^{-/-} mice, as previously described [246]. NOD Foxp3-GFP mice were generated by speed-congenic backcrossing of the B6 Foxp3-GFP (Jax stock number 006772) to NOD mice, as previously described [111]. BALB/C mice were purchased from Taconic Denmark. All animals were bred and maintained in a specific pathogen-free environment at the animal facilities at Lund University. Guinea pigs were purchased from Harlan laboratories. ZnT8-KO mice and littermate were generated as previously described [238]. The ethics committee of Lund University and the Swiss cantonal veterinary authorities approved all experimental animal procedures.

Animal preparation for *in vivo* imaging with FOCI Mice were anesthetized in an induction box with 3% isoflurane mixed with oxygen (0.8-1 l/min). For imaging the anesthesia was maintained at 1% isoflurane. Mouse head and eyeball were restrained as previously described [108]. The mouse was kept on a heating stage during the whole imaging session. *In vivo* imaging was done with the xfOCM setup (Fig. 5.3) with a water immersion N-Achroplan 10x/0.3 Zeiss objective. Viscotears liquid gel (Alcon) was used as immersion liquid. Mice were subcutaneously injected with buprenorphine during the imaging session (0.15 mg/kg).

5.2.2 Pancreatic islet isolation, culture and ACE transplantation

Pancreatic islets were isolated according to the protocol previously described [109]. Islets were manually picked under a stereomicroscope and incubated in 5% CO₂ at 37° C

5.2. Material and Methods

overnight. At the time of transplantation, the recipient animal was anesthetized using inhalation anesthesia (isoflurane; Schering-Plough, Kenilworth, NJ, USA). To obtain post-operative analgesia, we administered buprenorphine (0.15 mg/kg; RB Pharmaceuticals, Slough, UK) subcutaneously. Between 10 and 50 cultured islets were transplanted per eye, as previously described [111]. For experiments including the study of healthy control islet grafts, 6-8 week-old BALB/C or B6.Foxp3-GFP recipient mice were ACE-transplanted with islets from BALB/C or B6.Rag2^{-/-} donors respectively. For experiments including the study of inflamed islet grafts mainly 10 week-old NOD.Foxp3-GFP recipient mice were ACE-transplanted with islets from NOD.Rag2^{-/-} donors.

5.2.3 Immunohistochemistry

Graft-bearing eyes or pancreas were isolated from mice after perfusion with 4% paraformaldehyde/PBS, cryo-protected in 30% sucrose/PBS, embedded in optimal cutting temperature compound (VWR, Radnor, PA, USA), frozen on dry ice and stored at -80° C. Frozen eyes and pancreas were cryo-sectioned (section thickness 8-10 µm). The eye sections have been cut parallel to the iris. Frozen sections were incubated with blocking buffer (10% Fetal Calf Serum in TRIS buffered saline (TBS) 0.1% Triton X-100) for 1 hour at room temperature. Incubation with primary antibodies was performed in a blocking buffer for 1 hour at room temperature. Antibodies used: guinea pig α -Insulin (Dako; Carpinteria, CA, USA); rat α -CD31 (MEC 13.3) and α -MAdCAM-1 (MECA-89, BD Biosciences; San Jose, CA, USA), rat biotinylated α -CD45 (30-F11, eBiosciences, San Diego, CA, USA), rabbit α -Glucagon, (Europroxima, Arnhem, Nederland). After three washing cycles in TBS-Triton X-100, secondary antibodies and DAPI have been added for 1 hour at room temperature. Secondary antibodies used: anti-guinea pig Alexa594, anti-rat Alexa647, anti-rabbit Alexa405 or Alexa 647; Life Technologies, Carlsbad, CA, USA). After three washes, sections were mounted with fluorescence mounting medium (Dako, Glostrup, Denmark) and image stacks have been acquired using a LSM700 Zeiss confocal microscope equipped with an Plan-Apochromat $\times 20/0,8$ objective (Carl Zeiss Jena GmbH, Germany). Post-acquisition enhancement (e.g. contrast enhancement for viewing purposes) was performed using Adobe Photoshop (Adobe, San Jose, CA, USA).

5.2.4 *Ex vivo* imaging with dfOCM

The pancreas of ZnT8^{+/+} (n=4), ZnT8^{-/-} (n=4) and guinea pigs (n=2) were fixed in 4% PFA in PBS, cryoprotected in 30% sucrose/PBS embedded in Optimal Cutting Temperature (CryomatrixTM, Thermo Scientific, Waltham, MA USA) compound and frozen in isopentane cooled with dry ice. 60 µm thick cryosections were prepared for staining. The sections were permeabilized 10 minutes with PBS-Triton X-100 0.25% and blocked in 10% fetal bovine serum for 30 minutes at room temperature. Incubation with primary antibodies (mouse α -insulin, Sigma-Aldrich, St Louis, MO, USA; rabbit

Chapter 5. Label-free longitudinal study of type I diabetes

α -glucagon, Cell Signaling, Danvers, MA, USA) was performed at 4° C overnight in a humid chamber. Secondary antibodies (anti-mouse Alexa647, anti-rabbit Alexa647, Life Technologies, Carlsbad, CA, USA) were incubated 45 minutes at room temperature. The sections were mounted with DABCO mounting medium and imaged using the dual system combining dfOCM [129] with confocal fluorescence (Fig. 5.1). All slides were analyzed blind-folded. Signal to noise ratio (SNR) is given as the mean of the islet intensity signal divided by the variance of the exocrine signal.

5.2.5 FOCI imaging

FOCI integrates the xfOCM instrument, with an improved acquisition (customized spectrometer for OCM) and optimized scanning modality for longitudinal functional imaging. A fast processing unit allows for real-time monitoring (structure and blood flow) and the platform is fully equipped for small animal imaging.

xfOCM instrument Our customized xfOCM [123] (extended focus Optical Coherence Microscopy) instrument, as shown in Figure 5.3, is based on a Mach-Zehnder interferometer. A beam splitter divides the beam of a broadband light source (fs-laser source; central wavelength $\lambda_c = 780$ nm; bandwidth $\Delta\lambda = 135$ nm, Femtolasers Inc., Austria) into a reference (green in Fig. 5.3) and an illumination beam (red in Fig. 5.3). The extended depth of field is due to a cone shaped optical element, called axicon, which provides an elongated uniform focal field over the whole imaged sample depth. This axicon generates a Bessel beam resulting in a high uniform lateral resolution (1.3 μm) deep inside the tissue structures. The axial resolution depends on the light source and on the light collection efficiency of the spectrometer. The broadband source provides a short coherence length (the coherence length l_c is proportional to the central wavelength λ_c and to the spectral width $\Delta\lambda$ of the light source : $l_c \propto \frac{\lambda_c^2}{\Delta\lambda}$), which results in a “coherence gating” in depth enabling a high axial resolution of ~ 2 μm in biological tissue. The investigated tissue, i.e., the transplanted islets, is scanned in the x-y lateral directions. The backscattered field from the sample interferes with the reference field and the resulting interference signal, called spectral interferogram, is detected by the spectrometer. The interferograms result from the different structures in depth in the tissue yielding a spectrum modulation due to constructive and destructive interference, which are recorded by a linear CMOS array detector (Basler Sprint spL4096-km). The Fourier transform of these spectral interferograms results in the depth profile.

OCM imaging has several unique features:

- OCM allows 3D imaging without depth scanning resulting in a multiplex advantage, which allows fast imaging of tissue structures with an *in vivo* penetration depth in the pancreas of ~ 300 μm and in ACE transplanted islet of ~ 400 μm .
- OCM is a label free imaging modality.

5.2. Material and Methods

The intrinsic contrast results from small refractive index changes of the sample structures. These features make OCM an ideal imaging method for small animal imaging.

Data acquisition Depth scans (A-scans) were acquired at a frequency of 70 kHz and were recorded by the line scan camera, digitized and stored on a Matrox frame grabber. The acquired data were processed at real-time for a preview of islet structure and blood flow. Multi-threading (in C++ programming language) was used to analyze the tomograms at frame rate of approximately 6 frames/s, which allowed for an interactive search of selected islet locations and a rapid vitality assessment of islets during the imaging sessions. The data were stored on high speed solid state drives for post data processing.

Scanning protocols The transverse scanners (x-slow axis, y-fast axis) were synchronized with the acquisition of spectral interferograms (depth scans). High motion contrast was achieved by acquiring along the fast axis 8 tomograms (B-scans) at the same location. These tomograms are averaged for structural imaging or analyzed to extract the Doppler signal for vascular imaging. Data along x- and y-direction were therefore scanned with square patterns of 4096×512 points over a range ($500 \times 500 \mu\text{m}^2$ - $800 \times 800 \mu\text{m}^2$) in order to match the islet size. This provided an isotropic sampling with a transverse pixel size of $1 \mu\text{m}$ - $1.5 \mu\text{m}$. This scanning protocol and acquisition speed were empirically set to minimize sample movements and simultaneously to match the blood flow speed.

5.2.6 Data processing

The acquired spectra (raw data, Fig. 5.15) are recorded as an intensity over wavelength ($I = I(\lambda)$). The average background signal is subtracted from the spectra (BG) and the spectra are resampled ($\lambda - k$) in the k -space ($k = \frac{2\pi}{\lambda}$). A Fourier transform (FT) allows calculating and extracting the depth profile (A-scan). For each A-scan and at each depth position the scattering signal is given as a complex field in amplitude and phase.

Two types of information can be analyzed independently:

- **Static** The magnitude of the complex field corresponds to the static (no motion) tissue, i.e., the structural information. The obtained three-dimensional microstructure is shown in logarithmic scale (Log) after histogram equalization (Hist).
- **Dynamic** Phase shifts induced by moving red blood cells (RBCs) across the sampling volume constitute the intrinsic contrast for visualization of the microvascular flow. The phase changes of the scattering signal are measured at different time points (repeated B-scans) in order to extract the Doppler signal information. All temporal variations are analyzed pixel by pixel along the oversampled slow axis. The time delay between adjacent pixels corresponds to the B-scan time interval of 7.4 ms.

Processing for extracting the vascularization

Phase variance The microvascularization is determined by extracting the circular phase variance (σ^2) over 8 tomograms (B-scans) acquired at the same transverse position using the following equation:

$$\sigma^2(x, y, z) = 1 - \left| \frac{A(x, y, z, t + \Delta t)A^*(x, y, z, t)}{\frac{1}{2}|A(x, y, z, t + \Delta t)|^2 + |A(x, y, z, t)|^2} \right| \quad (5.1)$$

where $A(x, y, z)$ represents the position of the A-scan in the C-scan and Δt the time difference between the two acquisitions. A schematic representation of the corresponding scan protocol for the phase variance is shown in Fig. 5.3b. To improve the contrast, an averaging of the circular phase variance over the axial direction can be applied. The values for the circular phase variance are limited between 0 and 1. In absence of an object, the circular phase variance of the noise is close to 1. To suppress this background contribution, the signal is weighted by the temporal derivative (TD) for a better contrast enhancement, background removal and minimization of phase decorrelation (explained below).

Bulk intensity shift (BIS) and global phase fluctuations (GPF) xfOCM is highly sensitive to all dynamic changes along the optical path in general and in particular to sample movements. Dynamic imaging requires discrimination between RBCs and physiological motions (cardiac and respiratory motions). Prior to circular phase variance calculations, we reduced all physiological motions. In analogy to what Lee *et al.* [231] observed, we consider two main consequences of motion effects: (1) bulk image shift (BIS) where the shift is larger than one pixel, and (2) global phase fluctuation (GPF) where the shift is within the range of one pixel. All BISs are analyzed with a reference tomogram (B-scan) chosen from the B-scan time-sequence. Bulk shifts are identified by maximizing the normalized cross-correlation of shifted B-scans:

$$\Gamma_{BIS}(\Delta z, \Delta x, t) = \frac{\left| \sum_{z,x} B(z + \Delta z, x + \Delta x, t)B^*(z, x, t_0) \right|}{\sqrt{\sum_{z,x} |B(z + \Delta z, x + \Delta x, t)|^2} \sqrt{\sum_{z,x} |B(z, x, t_0)|^2}} \quad (5.2)$$

where $B(z, x, t_0)$ represents the reference B-scan. To limit the computation time, we used an efficient subpixel image registration method [247], where the achieved accuracy is well comparable to the conventional cross-correlation method based on fast Fourier transform. According to this approach, we developed an algorithm for a fast recognition of the bulk shifted B-scans. When the B-scan shift is larger than 1 pixel, the phase information is lost and cannot be used. Therefore, this B-scan was excluded from the phase variance calculation and the analysis was performed on the remaining tomograms. The GPF was also analyzed with a selected reference tomogram. GPF is less than 1 pixel and affects only the phase information. The phase correction is done in the axial and lateral

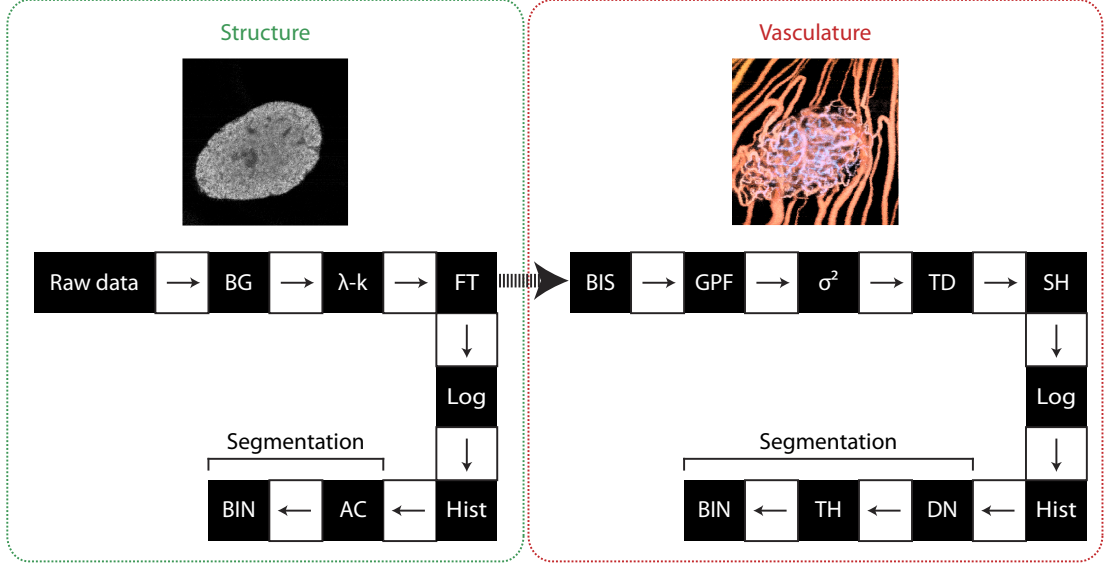


Figure 5.15: **Data processing flow chart.** **Raw data:** spectra acquired by the xfOCM; **BG:** the average background signal subtracted from the spectra; **λ-k:** resampling procedure from optical wavelength space to optical wavenumber space; **FT:** Fourier transform; **Log:** logarithm to base 10 applied to the magnitude of FT; **Hist:** histogram equalization; **AC:** active contour; **BIS:** bulk intensity shift removal; **GPF:** global phase fluctuation correction; σ^2 : circular phase variance analysis; **TD:** temporal derivative used as a weight for phase variance; **SH:** step-down exponential filtering of shadows; **DN:** denoising algorithm to remove remaining background noise; **TH:** image thresholding; **BIN:** image binarization.

directions. Global phase fluctuations correction factor are determined at each transverse position for the different time (8 B-scans) by:

$$GPF_{axial}(x, t) = -arg\left(\sum_z B(z, x, t)B^*(z, x, t_0)\right)$$

$$GPF_{lateral}(z, t) = -arg\left(\sum_x B(z, x, t)B^*(z, x, t_0)\right)$$

The complex signal B is then multiplied by the calculated GPF correction factors. To significantly remove phase fluctuation this operation is repeated 5 times axially and laterally. The correction for axial shift is applied as follows:

$$B_{corrected}(x, t) = \sum_z B(z + \Delta z, x, t)e^{iGPF_{axial}(x, t)}B^*(z, x, t_0) \quad (5.3)$$

Temporal derivative (TD) Phase variance allows to discriminate between static (structure) and dynamic (motion) phase contributions of the sample. However, the background signal (phase noise) outside the sample is not eliminated. The temporal derivative was

used to reveal vessels structures from OCT data [166]. Weighing the phase variance with the temporal derivative of xFOCM signal suppresses largely this contribution and improves significantly the background filtering:

$$TD = \sqrt{|B(z, x, t + \Delta t) - B(z, x, t)|^2} \quad (5.4)$$

The temporal derivative is taken as the difference between two consecutive tomograms acquired at the same location. Finally, if more than two B-scans have been acquired at the same location, the mean is taken.

5.2.7 Image post processing

Phase variance analysis provides an image of the vascularization in all three dimensions. Here, we implement a quantitative analysis of the vascular network inside the islets of Langerhans. The algorithms are automated or semi-automated to limit labor-intensive work and minimize the analysis prone to operator's error.

Segmentation of three-dimensional structure β -cells are characterized by a high contrast in the xFOCM tomograms. Based on the intensity information, we segmented the β -cells volume using an algorithm based on active contours (AC) [130] and sparse field algorithms [148], which was already applied to quantify β -cell volume in *ex-vivo* pancreatic sections imaged with xFOCM [161]. In a healthy islet the β -cells volume represents the major part of the islet, which is not the case in an infiltrated islet. The infiltrated volume was obtained by subtracting the β -cell volume from the islet volume.

Denoising of three-dimensional vascular network Due to the high scattering of RBCs, the vascular network is easily detectable in all three dimensions by xFOCM. However, deeper structures show less contrast due to multiple scattering or absorption of the sample. Additionally Doppler techniques suffer from artifacts caused by forward scattering. Indeed, in structural tomograms, a shadow (dark stripe) are visible below the vessels due to absorbed light by RBCs. On the contrary, in phase variance tomograms, these shadows are converted into signal similar to the one given by the vessels, which yields a signal extending below each vessel. We remove these artifacts by applying a step-down exponential filter [180] starting from the top surface of the tissue (SH step in Fig. 5.15). In order to remove artifacts from the step-down filter, the attenuation coefficients are smoothed by an additional interpolation (after removal of out of range coefficients). To remove remaining background noise, we applied a denoising algorithm (DN) suppressing Gaussian and Poisson noise. This approach uses the minimization of an unbiased estimate of the mean squared error (MSE) for noise, a linear parametrization of the denoising process and the preservation of noise statistics across scales within the Haar discret wavelet transform (DWT). For more information on this algorithm, we refer the reader to Luisier *et al.* [248]. Finally, the denoised image is thresholded (TH) and binarized

(BIN) with ImageJ.

Three-dimensional rendering Three-dimensional rendering is performed using Imaris software. Specific information is split between different channels (first channel structure, second channel vascularization, etc.). Additionally, the β -cell volume together with infiltration volume is segmented using surface topography (β -cells in green and infiltration volume in blue).

Volumetric quantification To extract vessel density, the vascular network volume part was divided by the corresponding segmented β -cells (βCV), islet or inflammation (infl.) volume. For Figure 5.11e, the relative vascular density of β -cells volume ($rvd_{\beta CV}$) and relative vascular density of inflammation volume ($rvd_{infl.}$) was computed like this:

$$\begin{aligned} rvd_{\beta CV} &= \frac{d_{\beta CV}}{d_{\beta CV} + d_{infl}} \cdot 100\% & d_{\beta CV} &= \frac{\text{vascular volume inside } \beta CV}{\beta CV} \\ rvd_{infl.} &= \frac{d_{infl}}{d_{\beta CV} + d_{infl}} \cdot 100\% & d_{infl.} &= \frac{\text{vascular volume inside infl. volume}}{\text{infl. volume}} \end{aligned}$$

For Figure 5.4 and Figure 5.12 normalized vascular density is $nd_{islet,w(i)}$:

$$\begin{aligned} nd_{islet,w(i)} &= \frac{d_{islet,w(i)}}{d_{islet,w(1)}} \\ d_{islet} &= \frac{\text{vascular volume inside islet}}{\text{islet volume}} \end{aligned}$$

Automatic attenuation compensation and contrast enhancement to match xfOCM image with IHC The xfOCM static signal is attenuated over depth due to multiple scattering and absorption. To reliably detect signals reflected from deep tissue structures, we applied a deattenuation algorithm based on the fact that local attenuation is proportional to the local reflectivity [249]. This deattenuation algorithm is used for figures 5.6e and 5.8 to compare the segmented OCM data with the IHC.

5.3 ACE long term imaging

In this thesis, we showed that OCM allows the monitoring of the β -cell volume as well as the vascularization. This opens the door to the application of OCM as a platform to test the effects of drugs that are supposed to delay/stop the progression of diabetes. To obtain a baseline, we followed isograft islets in the ACE of BALB/C mice over a period of 10 months (Fig. 5.16).

An intriguing point is that the islets kept growing throughout the study (Fig. 5.16a,b and Fig. 5.17), reaching 11 months post transplantation a volume in average 3.5 times larger than at the time of the graft. Interestingly, the vascular density initially increased, but then reached a plateau at around 13% (Fig. 5.18), which indicates an adaptation of the vascular network to the increasing islet volume. Indeed, only 12 days after transplantation, the grafted islets have a similar vascularization as islets *in situ*. However, the vascular density is still a little bit lower than the plateau reached in the following weeks (Fig. 5.18). This percentage of vascularization is in the range of what was observed in islets *in situ* and is comparable to the vessel density measured by Almaça *et al.* [175] in islets grafted in the ACE by tail vein injection of fluorescent labeled dextran. The grafted islets have a tendency to fuse together, giving rise to large islets over time. This growth generally did not prevent the longitudinal imaging of islets. However, at the last point in time, we observed a massive structural change for mouse 1 where islets 5 to 7 fused together (Fig. 5.17). This growth is very surprising since both the grafted islets and the recipient are adults. Indeed, the rate of pancreatic β -cells replication has been shown to be restricted and very low in aged mice [250–253]. A deeper analysis of these phenomena is required. In particular, we need to determine whether the β -cell volume expansion occurs through increased proliferation or by swelling. The mechanisms beyond this increased β -cell volume are unknown. It could be the absence of contact with the exocrine tissue that does not restrain the expansion of β -cells.

Between the imaging sessions, the eyeball has not always the same orientation. Part of a same islet can appear deeper in an imaging session and therefore be more attenuated and less well segmented. The non β -cell volume is computed by subtracting the β -cell volume from the islet volume. The islet volume is computed by manually filling the holes inside the β -cell volume. The origin of these darker areas is non β -cell volume such as other endocrine cells, ducts and vessels. Therefore, we could infer that the non β -cell volume should be at least comparable to the vascular volume. However, only large vessels give a significantly darker signal and, for smaller vessels, their structural detection depends also on their orientation with respect to the beam. Since the OCM signal is attenuated in depth, the algorithm may fail to resolve the deeper part of the islet. However, this attenuated part is manually added to the β -cell volume when it can be attributed to it upon inspection by eye. This subjective part can lead to variations in the β -cell volume detection. Nevertheless, the percentage of non β -cell volume measured in control mice indicates that only an infiltration higher than 3% could be detected in NOD mice (Fig. 5.16d).

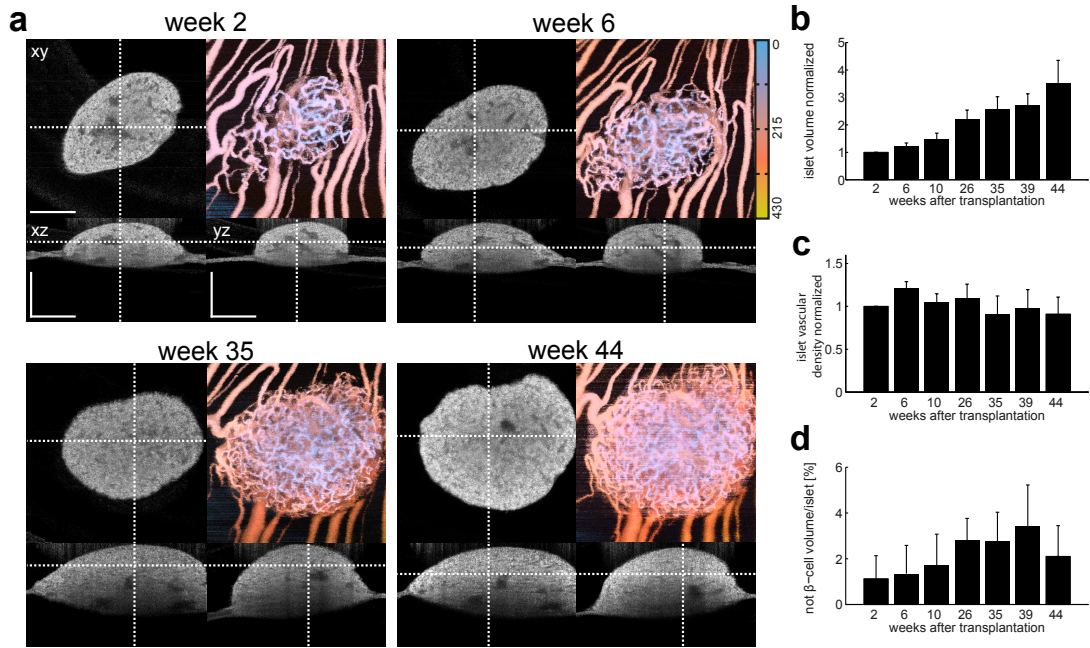


Figure 5.16: **Longitudinal imaging over 10 months on BALB/C mice.** (a) Structure and corresponding maximum depth projection of the vascularization. Colorbar indicates depth position in micrometers. The zero position corresponds to the beginning of the tomogram to have the islet in focus. (b) Evolution of the volume of the islet normalized by the initial volume at week 2. (c) Islet vascular density evolution normalized by the density at week 2. (d) Percentage of the tissue not detected as β -cell volume in the segmentation. A minimum of 5 islets per time point were analyzed. Scale bar: 200 μ m.

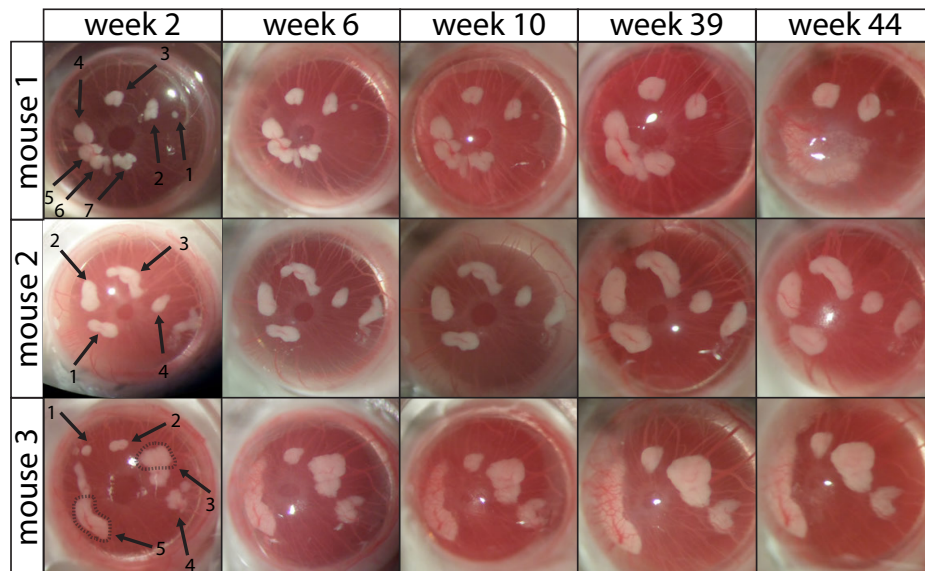


Figure 5.17: **Macro-view of 3 BALB/C mice.** Arrows indicate islets that were followed over time. The growth is visible for all islets.

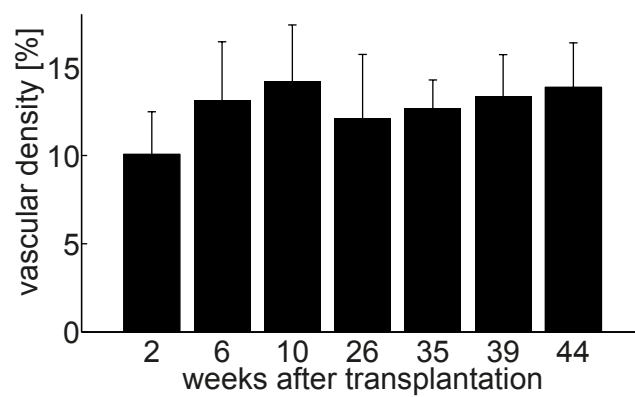


Figure 5.18: Islet vascular density in percentage computed on a subvolume.

6 Conclusion and Perspective

This thesis exploited the main advantages of OCM, i.e., its label-free contrast and fast acquisition, to image islets of Langerhans. We started from *ex vivo* measurements and progressed towards a functional study allowing to monitor islet structure and its vascularization during the development of autoimmune diabetes. In the particular case of pancreas imaging, the label-free OCM technique has a specific contrast for β -cells. We demonstrated the origin of the strong scattering of islets in OCM to be dominated by nanocrystalline aggregates made of insulin and zinc ions. *Ex vivo* measurements are important for validation of the technique and to determine the origin of different contrasts in OCM. Yet, despite a faster acquisition, *ex vivo* OCM imaging has few advantages compared to fluorescence microscopy, which offers a higher spatial resolution and molecular specificity. The advantages of OCM become more evident for *in vivo* studies where fast acquisition is required both to decrease the duration of imaging sessions and to overcome the movement artifacts of the tissue. In the particular case of pancreas imaging, less invasive imaging can be achieved through a laparotomy and by imaging the duodenal pancreas encircled by the duodenum. In this way, no splenectomy is required and longitudinal imaging could be performed, even if it requires a complex procedure and surgical skills. Despite a stabilization of the pancreas achieved by placing the duodenum around a small pillar, cardiac, breathing and peristaltic movements cannot be completely eliminated. In particular, the stabilization achieved is highly dependent on the duodenum anatomy of each mouse, which limits the repeatability and success of each imaging session. The multiplex acquisition of OCM limits the impact of these movements, with only some artifacts between B-scans in the case of a poor stabilization.

The *in silico* simulations performed in Chapter 2 indicated that the islet distribution-based criterion has a better prediction accuracy than the integral β -cell volume criterion and that, in specific conditions, imaging of a subpart of the pancreas might be sufficient to indicate a deviation from a healthy situation. However, a more complex infiltration scenario drives OCM to its limits to detect earlier phase of diabetes progression. Nevertheless, this does not prevent the detection of structural and functional changes at the islet level. Besides the opportunity to image wild type mice as opposed to genetically modified mice,

another *in vivo* advantage of OCM is the simultaneous label-free angiography, which avoids the injection of exogenous labels that can accumulate in organs and cause toxicity.

Blood flow assessment As described in Chapter 3, OCM can extract blood velocity even though the detection of red blood cells in capillaries is difficult. Indeed, red blood cells are passing through capillaries one at a time, which results in a varying filling of the vessel over time. Therefore, depending on when the A-scan is taken, one or no red blood cell is detected, giving rise to a unreliable statistic to extract the Doppler frequency shift. As a result, some capillaries are not visible in one volume, thereby explaining why more vessels are detected in angiography than in resolved blood flow. One way to overcome this issue would be to inject intralipid to fill continuously the capillaries with scatterers [190]. However, we cannot rule out that the strong scattering of the islet could still hinder the detection of the endocrine blood flow. Indeed, blood flow could rarely be detected inside small endocrine capillaries, but it could be resolved mainly in large vessels in the ACE transplanted islets. An alternative solution to go deeper into the tissue would be to use a light source in the 1.3 μm wavelength range. However, the β -cell contrast at these wavelengths has to be determined. Assessment of axial blood flow is common in the OCT community but imposes severe limitations. Indeed, the axial velocity component depends on the angle between the vessel and the optical axis. Therefore, these measurements are really sensitive to movements and impose severe conditions to compare changes over time or between different animals. Total flow ($\frac{\text{mm}}{\text{s}}$) can be deduced by resolving both axial and lateral flow velocity [189]. However, to resolve the lateral flow, a larger oversampling is required, thereby leading to larger acquisition times. To address this problem, the total blood flow could be computed from B-scans only, yielding the blood flow velocity for a vessel cross-section. An alternative is to use perfusion ($\frac{L}{\text{min}}$) or volumetric flow ($\frac{L}{\text{min mm}^2}$), by integrating the axial Doppler frequencies in an *en face* view of a cross-section of a vessel [163].

The best way to validate our technique would be to quantify the increase of islet blood flow after glucose injection, as already shown using fluorescent labeled red blood cells [43] or injection of microspheres [28, 30]. However, preliminary measurements show that the level of anesthesia reached with isoflurane can alter the blood flow, which might prevent the glucose blood flow response. Instead, injectable anesthesia could be investigated. A monitoring of vital parameters such as heart beat and breathing rate are therefore required. Depending on the expected time resolution and stability of the tissue, we could perform B-scans over time on different vessels previously chosen based an angiography or acquire full 3D volume of the islets.

Multimodal imaging Enhancement of OCM with a fluorescent channel adds specificity for structures or molecules not visible with OCM only. A fluorescent channel was used to determine the specificity of a potential β -cell marker by assessing the co-localization of the OCM islet signal with the fluorescent signal from the tracer. The multiplex advantage of OCM allows to rapidly scan the tissue, thereby imaging several islets during

the imaging session. This advantage allowed us to show that the accumulation of the tracer was not identical between islets. A widefield fluorescent channel was also added to correlate the degradation of the OCM signal with infiltration of Foxp3⁺ T-cells. However, both confocal and widefield fluorescent channels are limited in penetration depth. The addition of a two-photon fluorescence channel would allow the correlation of the molecular signature of particular cells over a similar depth than the OCM signal.

ACE model The combination of OCM with the ACE transplantation model showed that the destruction of the β -cell volume following massive infiltration can be detected with OCM. However, the infiltration signal is not as specific as the β -cell signal. Indeed, depending on the orientation, the endothelial vessels can give rise to a weaker signal and the multiple scattering below vessels decreases the strong OCM signal of β -cells. The shadow artifacts spanned by vessels has to be removed in a post-processing step, which has the drawback of removing some of the small capillaries. As a result, OCM angiography may not be sensitive to minor changes of islet vascular density. Nevertheless, a reorganisation of the vascular network coinciding with destroyed β -cell volume was clearly observable. The longitudinal study in Chapter 5 has been done on NOD mice grafted at 10 weeks of age with already ongoing autoimmune inflammation. As expected islet grafts were rapidly infiltrated already 1 week post transplantation and a massive destruction was observed only 3 weeks after transplantation in the ACE. Further studies of the initial events of early insulitis and progression of inflammation during the natural course of diabetes of young grafted mice would be interesting, especially looking at the evolution of the vascularization. To dissociate the revascularization process from the remodelling of the vascularization due to the inflammation process, an adoptive transfer of T-cells from diabetic mice to NOD.Rag2^{-/-} grafted mice could be done. The OCM platform coupled with the ACE model could be suitable to study the effect of drugs that aim to block the immune response. Longitudinal studies with drug treatment could determine whether the vascular network or the β -cell volume is first restored. Along the same lines, drugs supposed to promote the proliferation of β -cells could be assessed and monitored. Nevertheless, prior to using this platform in this context, further investigations into the ACE model, and more particularly into the apparent constant growth of the islets, needs to be carried out.

In general, longitudinal studies correlate with large amounts of data to segment. Therefore, two improvements of the current segmentation of β -cell volume could be foreseen: (1) elimination of manual operations, especially to detect the deeper part of the islets and (2) acceleration of the imaging processing, e.g., by implementing the algorithm on graphics processing unit (GPU) cards.

Another unique property of OCM is both the label-free imaging of the vascular network together with the extraction of blood flow velocity. We demonstrated that OCM angiography can be used to monitor the vascular network in islets of Langerhans during the inflammation process in a mouse model of T1DM. A future important development

would be the quantification of blood velocity in a healthy state as well as during the development of diabetes. Despite some eyeball movements, the ACE imaging offers a better and more reproducible stability. Therefore, ACE seems a better choice to monitor blood flow than the pancreas, especially since it offers the possibility to perform longitudinal studies. For T1DM, the relationship between blood flow, vascularization and inflammation could be determined. Since the islet vasculature becomes wider in T2DM models [113, 118, 169], islet blood flow signature in T1DM and T2DM diabetes could be compared. We can assume that an increased blood flow following glucose injection is related to an efficient insulin delivery. It would be therefore interesting to determine whether this response is altered during the progression of diabetes. Stabilization issues have to be solved by developing acquisition protocols (including new scanning systems) adapted to the biological question, i.e., modification of the blood flow at a short interval following islet stimulation or during longitudinal studies. Besides stability issues, a better understanding of the anesthesia and its impact on the blood flow have to be carefully investigated.

Label-free imaging is crucial, especially for the imaging of human tissue. Indeed, examination of human pancreas biopsies have confirmed that human pancreatic islets can also be detected with OCM (Fig. 6.1). This finding opens the possibility of imaging human islets grafted into the ACE of mice. It is well known that there are differences between the organisation of human and rodent islets [5–7]. Even with limited access to diabetic human pancreas, there are indications that animal models do not recapitulate exactly the human insulinitis process. Compared to NOD mice, human islets exhibit a weaker infiltration with a more heterogeneous spatial pattern of inflammation, with some islets not being attacked [254, 255]. OCM would allow an easy comparison of these differences, especially in terms of vascularization and inflammation of the islets. In addition, OCM could be useful for studying xenograft rejections. The most exciting application would be a longitudinal study of human islets from a diabetic patient grafted into the ACE of a humanized mouse whose immune system has been reconstituted from the same diabetic patient.

This thesis investigated selected areas of application for OCM in islets of Langerhans imaging. We demonstrated applications of OCM to image islets of Langerhans both *ex vivo* and *in vivo*, and we have shown its advantages and limitations. The label-free imaging property of OCM is both its strength and its weakness due to the lack of specificity of its signal. However, it offers an unique opportunity to reveal structures in three dimensions with a fast acquisition. The lack of specificity can be overcome by enhancing OCM with a second modality such as fluorescence microscopy. Using this approach, it can facilitate the initial screening of β -cell tracers. Finally, we developed tools allowing quantification of the β -cell volume, inflammation and vascularization during the progression of T1DM.

In this work, we have applied OCM as a research tool requiring interdisciplinary skills and

a team constituted of engineers from different fields. Even if classical OCT instruments are available, they do not have the required resolution and depth of field to image islets of Langerhans. Therefore, to establish OCM as a standard tool for biological research on the pancreas and islets of Langerhans, the technology needs to be routinely available as a tool in laboratories. This would require an industrialization of the xFOCM platform, ideally integrating a two-photon microscope to add molecular specificity for structures undetectable with OCM only (e.g., immune cells, β -cell tracers).

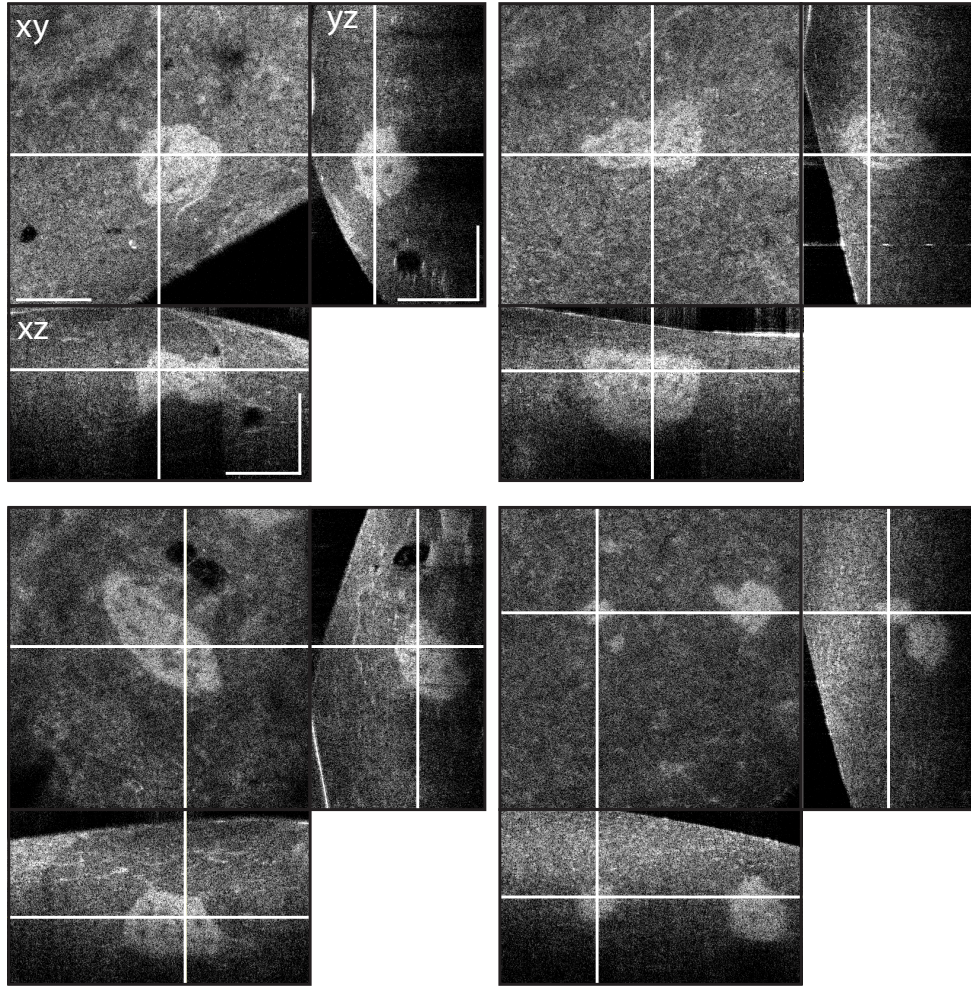


Figure 6.1: Biopsies of human pancreas imaged with xFOCM. Scale bar: 200 μm .

Acknowledgements

I would like to thank Prof. Theo Lasser and Prof. Anne Grapin-Botton, who gave me the possibility to work on this exciting interdisciplinary project. I am grateful to Theo for his unconditional support and for his enthusiasm. I really appreciated his availability for scientific and personal discussions. I would like to thank Anne for being always available to answer my questions and guide me, in spite of her moving to Copenhagen. I really enjoyed our scientific discussions and her encouragements.

A thesis is a long and demanding work, but thanks to the good atmosphere in the laboratory, I really enjoyed this period. I would like to thank all current and former members of the Laboratoire d'Optique Biomédicale (LOB): Sergiy Mayilo, Stéphane Broillet, Stefan Geissbühler, Azat Sharipov, Akihiro Sato, Tomas Lukes, Miguel Sison, Amir Nahas, Claudio Dellagiacoma, Christophe Pache, Martin Villiger, Daniel Szlag, Marcin Sylwestrzak, Séverine Coquoz, Arno Bouwens, Paul Marchand, David Nguyen, Tristan Bolmont, Taoufiq Harach, Jérôme Extermann, Noelia Bocchio, Erica Martin-Williams, Iwan Maerki, Matthias Geissbühler, Marcel Leutenegger, Antonio Lopez, and Ronald Gianotti. I am grateful to Judith Chaubert, Fabienne Ubezio, Christiane Good and Noelia Simone for their support, which goes way beyond administrative issues. Christophe and I were lucky to have an office just for the two of us for quite some time and it was a really enjoyable time. I would like to thank Claudio with whom I shared my office for a short time and who had the great idea, with Christophe, to add some nice posters of mountains in our office. They are still hanging there, and they allowed me to escape from time to time. At the end of my thesis, I enjoyed sharing my office with Daniel and Miguel. Special mention to Miguel for his attention to detail; he would know my schedule better than me.

Special thanks to Arno and Christophe with whom I had a lot of discussions about OCM and who helped me with many technical issues. I also really enjoyed our numerous non-scientific discussions, which generated a lot of laughs. When I could not see any solution to a problem, a discussion with Arno would always point me in the right direction. I thank Paul and Fabienne for teaching me that people do not only go “en montagne” but also “à la montagne”. I would like to thank Stéphane, with whom I started the PhD; it was nice to share the different steps of our PhD theses.

Acknowledgements

I have to thank the “crazy” office of the new LOB generation: Séverine, Paul and David. Their weird ideas and loud laughs were a perfect distraction from the writing of this thesis (also, I owe them my new phone). Special thanks to the tea drinkers at LOB—or maybe should it be Tekoe thanking me for bringing you there? Thanks to Séverine for joining the LOB; thanks to you, the number of women at LOB doubled. I would like to thank Jérôme and Daniel for the countless hours spent next to the microscope while imaging the mice; I hope you did not dream too much about finding islets. Thanks to Jérôme for always making me look at the bright side of any situation and for his feedback on the thesis manuscript.

I would like to thank Tonio and Ronald who built most of the mechanical and electronical parts used in this work. Tonio, your music and your loud laugh were always a good distraction during breaks or long imaging sessions.

I would like to thank Gisèle Ferrand for her precious help with animal handling. Thanks to Sandra Offner who taught me intravenous tail vein injection. I would also like to thank the team from the histology core facility who were always very helpful.

A large part of this work would not have been possible without international collaborations. I would like to thank Lieke Joosten, Maarten Brom and Martin Gotthardt at the Radboud University Medical Center for their precious help with the evaluation of Cy5.5-exendin-3 as a β -cell tracer. Special thanks to Dan Holmberg, Anja Schmidt-Christensen and Lisbeth Hansen at the Lund University to have made possible the ACE model in our laboratory. I would also like to thank the former member of the UPGRA group with whom I worked and who introduced me to pancreas development: Cédric Cortijo, Chiara Greggio, Filippo De Franceschi, Emilie Gesina, Laurence Lemaire, Joan Goulley, David Martin, Marianne Nkosi, Marine Rentler-Courcier, Yung Hae Kim, Mathieu Gouzi, Keiichi Katsumoto, Nancy Thompson, and Yvan Pfister.

I would like to thank Joan Goulley and Martin Villiger who initiated me to this research topic during my master project and gave me the motivation to pursue a PhD in this field.

I would also like to thank Prof. Nicolas Grandjean, Prof. Luc Bouwens, Dr. Erwin Ilegems and Prof. Michael Liebling for kindly accepting to be part of my thesis committee.

My good thanks go to my friends in Valais, Lausanne and abroad. Un tout grand merci à mes parents et à ma soeur qui m'ont toujours soutenue et encouragée tout au long de mes études. My deepest thank to Grégory who always supports me and shared the ups and downs of my thesis.

Lausanne, February 2015

Corinne Berclaz

Bibliography

- [1] A. Kim et al. “Islet architecture: a comparative study”. *Islets* 1.2 (2009), 129–136.
- [2] P. A. Halban. “Cellular sources of new pancreatic β cells and therapeutic implications for regenerative medicine”. *Nature Cell Biology* 6.11 (2004), 1021–1025.
- [3] G. C. Weir and S. Bonner-Weir. “Islet β cell mass in diabetes and how it relates to function, birth, and death.” *Annals of the New York Academy of Sciences* 1281.1 (2013), 92–105.
- [4] A. Hörnblad, A. Cheddad, and U. Ahlgren. “An improved protocol for optical projection tomography imaging reveals lobular heterogeneities in pancreatic islet and β -cell mass distribution.” *Islets* 3.4 (2011), 204–208.
- [5] M. Brissova et al. “Assessment of human pancreatic islet architecture and composition by laser scanning confocal microscopy.” *The Journal of Histochemistry and Cytochemistry* 53.9 (2005), 1087–1097.
- [6] O. Cabrera et al. “The unique cytoarchitecture of human pancreatic islets has implications for islet cell function.” *Proceedings of the National Academy of Sciences of the United States of America* 103.7 (2006), 2334–2339.
- [7] D. Bosco et al. “Unique arrangement of α - and β -cells in human islets of Langerhans.” *Diabetes* 59.5 (2010), 1202–1210.
- [8] M. F. Dunn. “Zinc-ligand interactions modulate assembly and stability of the insulin hexamer – a review.” *Biometals* 18.4 (2005), 295–303.
- [9] G. Dodson and D. Steiner. “The role of assembly in insulin’s biosynthesis.” *Current Opinion in Structural Biology* 8.2 (1998), 189–194.
- [10] C. S. Olofsson et al. “Fast insulin secretion reflects exocytosis of docked granules in mouse pancreatic B-cells.” *Pflügers Archiv* 444.1-2 (2002), 43–51.
- [11] E. Fava et al. “Novel standards in the measurement of rat insulin granules combining electron microscopy, high-content image analysis and in silico modelling.” *Diabetologia* 55.4 (2012), 1013–1023.
- [12] S. L. Howell. “The mechanism of insulin secretion.” *Diabetologia* 26.5 (1984), 319–327.

Bibliography

- [13] R. Rodriguez-Diaz et al. "Noninvasive in vivo model demonstrating the effects of autonomic innervation on pancreatic islet function." *Proceedings of the National Academy of Sciences of the United States of America* 109.52 (2012), 21456–21461.
- [14] Z. Fu, E. R. Gilbert, and D. Liu. "Regulation of insulin synthesis and secretion and pancreatic Beta-cell dysfunction in diabetes." *Current Diabetes Reviews* 9.1 (2013), 25–53.
- [15] P. Newsholme and M. Krause. "Nutritional regulation of insulin secretion: implications for diabetes." *The Clinical Biochemist Reviews* 33.2 (2012), 35–47.
- [16] P. Newsholme, K. Bender, A. Kiely, and L. Brennan. "Amino acid metabolism, insulin secretion and diabetes." *Biochemical Society Transactions* 35.5 (2007), 1180–1186.
- [17] L. J. C. van Loon et al. "Amino acid ingestion strongly enhances insulin secretion in patients with long-term type 2 diabetes." *Diabetes Care* 26.3 (2003), 625–630.
- [18] D. Keane and P. Newsholme. "Saturated and unsaturated (including arachidonic acid) non-esterified fatty acid modulation of insulin secretion from pancreatic beta-cells." *Biochemical Society Transactions* 36.5 (2008), 955–958.
- [19] H. C. Denroche, F. K. Huynh, and T. J. Kieffer. "The role of leptin in glucose homeostasis". *Journal of Diabetes Investigation* 3.2 (2012), 115–129.
- [20] S. C. Gunawardana. "Benefits of healthy adipose tissue in the treatment of diabetes." *World Journal of Diabetes* 5.4 (2014), 420–430.
- [21] X. Yu, B.-H. Park, M.-Y. Wang, Z. V. Wang, and R. H. Unger. "Making insulin-deficient type 1 diabetic rodents thrive without insulin." *Proceedings of the National Academy of Sciences of the United States of America* 105.37 (2008), 14070–14075.
- [22] M.-Y. Wang et al. "Leptin therapy in insulin-deficient type I diabetes." *Proceedings of the National Academy of Sciences of the United States of America* 107.11 (2010), 4813–4819.
- [23] H. C. Denroche et al. "Leptin therapy reverses hyperglycemia in mice with streptozotocin-induced diabetes, independent of hepatic leptin signaling." *Diabetes* 60.5 (2011), 1414–1423.
- [24] S. C. Gunawardana and D. W. Piston. "Reversal of type 1 diabetes in mice by brown adipose tissue transplant." *Diabetes* 61.3 (2012), 674–682.
- [25] M. W. Schwartz et al. "Cooperation between brain and islet in glucose homeostasis and diabetes". *Nature* 503.7474 (2013), 59–66.
- [26] N. Ballian and F. C. Brunnicardi. "Islet vasculature as a regulator of endocrine pancreas function." *World Journal of Surgery* 31.4 (2007), 705–714.
- [27] L. Jansson and P.-O. Carlsson. "Graft vascular function after transplantation of pancreatic islets." *Diabetologia* 45.6 (2002), 749–763.

-
- [28] L. Jansson and C. Hellerström. "Stimulation by glucose of the blood flow to the pancreatic islets of the rat." *Diabetologia* 25.1 (1983), 45–50.
- [29] N. Lifson, C. V. Lassa, and P. K. Dixit. "Relation between blood flow and morphology in islet organ of rat pancreas." *American Journal of Physiology* 249.1 (1985), E43–E48.
- [30] L. Jansson and S. Sandler. "Alloxan-induced diabetes in the mouse: Time course of pancreatic B-cell destruction as reflected in an increased islet vascular permeability". *Virchows Archiv* 410.1 (1986), 17–21.
- [31] T. Alanentalo et al. "Quantification and three-dimensional imaging of the insulinitis-induced destruction of β -cells in murine type 1 diabetes." *Diabetes* 59.7 (2010), 1756–1764.
- [32] S. Bonner-Weir and L. Orci. "New perspectives on the microvasculature of the islets of Langerhans in the rat." *Diabetes* 31.10 (1982), 883–889.
- [33] J. R. Henderson and M. C. Moss. "A morphometric study of the endocrine and exocrine capillaries of the pancreas." *Experimental Physiology* 70.3 (1985), 347–356.
- [34] A. M. Svensson, C. G. Ostenson, and L. Jansson. "Age-induced changes in pancreatic islet blood flow: evidence for an impaired regulation in diabetic GK rats." *American Journal of Physiology-Endocrinology and Metabolism* 279.5 (2000), E1139–E1144.
- [35] M. Brissova et al. "Pancreatic islet production of vascular endothelial growth factor- α is essential for islet vascularization, revascularization, and function." *Diabetes* 55.11 (2006), 2974–2985.
- [36] X. Li et al. "Islet microvasculature in islet hyperplasia and failure in a model of type 2 diabetes". *Diabetes* 55.11 (2006), 2965–2973.
- [37] D. Eberhard, M. Kragl, and E. Lammert. "'Giving and taking': endothelial and β -cells in the islets of Langerhans." *Trends in Endocrinology & Metabolism* 21.8 (2010), 457–463.
- [38] L. R. Nyman et al. "Real-time, multidimensional in vivo imaging used to investigate blood flow in mouse pancreatic islets." *The Journal of Clinical Investigation* 118.11 (2008), 3790–3797.
- [39] M. D. Menger, P. Vajkoczy, C. Beger, and K. Messmer. "Orientation of microvascular blood flow in pancreatic islet isografts." *The Journal of Clinical Investigation* 93.5 (1994), 2280–2285.
- [40] J. I. Stagner, E. Samols, and V. Marks. "The anterograde and retrograde infusion of glucagon antibodies suggests that A cells are vascularly perfused before D cells within the rat islet." *Diabetologia* 32.3 (1989), 203–206.
- [41] J. I. Stagner and E. Samols. "The vascular order of islet cellular perfusion in the human pancreas." *Diabetes* 41.1 (1992), 93–97.

Bibliography

- [42] E. Samols, J. I. Stagner, R. B. Ewart, and V. Marks. “The order of islet microvascular cellular perfusion is B—A—D in the perfused rat pancreas.” *The Journal of Clinical Investigation* 82.1 (1988), 350–353.
- [43] L. R. Nyman, E. Ford, A. C. Powers, and D. W. Piston. “Glucose-dependent blood flow dynamics in murine pancreatic islets in vivo.” *American Journal of Physiology-Endocrinology and Metabolism* 298.4 (2010), E807–E814.
- [44] E. Lammert et al. “Role of VEGF-A in vascularization of pancreatic islets”. *Current Biology* 13.12 (2003), 1070–1074.
- [45] J. D’Hoker et al. “Conditional hypovascularization and hypoxia in islets do not overtly influence adult β -cell mass or function.” *Diabetes* 62.12 (2013), 4165–4173.
- [46] R. B. Reinert et al. “Vascular endothelial growth factor-A and islet vascularization are necessary in developing, but not adult, pancreatic islets”. *Diabetes* 62.12 (2013), 4154–4164.
- [47] J. Agudo et al. “Vascular endothelial growth factor-mediated islet hypervascularization and inflammation contribute to progressive reduction of β -cell mass.” *Diabetes* 61.11 (2012), 2851–2861.
- [48] S. A. Villalta et al. “Inhibition of VEGFR-2 reverses type 1 diabetes in NOD mice by abrogating insulinitis and restoring islet function.” *Diabetes* 62.8 (2013), 2870–2878.
- [49] E. M. Akirav et al. “Glucose and inflammation control islet vascular density and β -cell function in nod mice: control of islet vasculature and vascular endothelial growth factor by glucose”. *Diabetes* 60.3 (2011), 876–883.
- [50] S. Sandler and L. Jansson. “Vascular permeability of pancreatic islets after administration of streptozotocin”. *Virchows Archiv* 407.4 (1985), 359–367.
- [51] M. de Paepe, M. Corriveau, and W. Tannous. “Increased vascular permeability in pancreas of diabetic rats: detection with high resolution protein A-gold cytochemistry”. *Diabetologia* 35.12 (1992), 1118–1124.
- [52] Z. Medarova et al. “Noninvasive magnetic resonance imaging of microvascular changes in type 1 diabetes.” *Diabetes* 56.11 (2007), 2677–2682.
- [53] American Diabetes Association. “Diagnosis and classification of diabetes mellitus.” *Diabetes Care* 37.Suppl 1 (2014), S81–S90.
- [54] T. Scully. “Diabetes in numbers.” *Nature* 485.7398 (2012), S2–S3.
- [55] L. Guariguata et al. “Global estimates of diabetes prevalence for 2013 and projections for 2035.” *Diabetes Research and Clinical Practice* 103.2 (2014), 137–149.
- [56] American Diabetes Association. “2. Classification and Diagnosis of Diabetes”. *Diabetes Care* 38.Suppl 1 (2015), S8–S16.

-
- [57] A. Green and C. C. Patterson. “Trends in the incidence of childhood-onset diabetes in Europe 1989-1998.” *Diabetologia* 44.3 (2001), B3–B8.
- [58] J. A. Bluestone, K. Herold, and G. Eisenbarth. “Genetics, pathogenesis and clinical interventions in type 1 diabetes.” *Nature* 464.7293 (2010), 1293–1300.
- [59] K. C. Herold, D. A. A. Vignali, A. Cooke, and J. A. Bluestone. “Type 1 diabetes: translating mechanistic observations into effective clinical outcomes.” *Nature Reviews Immunology* 13.4 (2013), 243–256.
- [60] M. A. Atkinson, G. S. Eisenbarth, and A. W. Michels. “Type 1 diabetes.” *Lancet* 383.9911 (2014), 69–82.
- [61] P. Concannon, S. S. Rich, and G. T. Nepom. “Genetics of type 1A diabetes.” *The New England Journal of Medicine* 360.16 (2009), 1646–1654.
- [62] T. L. van Belle, K. T. Coppieters, and M. G. von Herrath. “Type 1 diabetes: etiology, immunology, and therapeutic strategies.” *Physiological Reviews* 91.1 (2011), 79–118.
- [63] V. Hyttinen, J. Kaprio, L. Kinnunen, M. Koskenvuo, and J. Tuomilehto. “Genetic liability of type 1 diabetes and the onset age among 22,650 young Finnish twin pairs: a nationwide follow-up study.” *Diabetes* 52.4 (2003), 1052–1055.
- [64] M. McCall and A. M. J. Shapiro. “Islet cell transplantation.” *Seminars in Pediatric Surgery* 23.2 (2014), 83–90.
- [65] A. M. J. Shapiro et al. “Islet transplantation in seven patients with type 1 diabetes mellitus using a glucocorticoid-free immunosuppressive regimen”. *New England Journal of Medicine* 343.4 (2000), 230–238.
- [66] S. A. White, J. A. Shaw, and D. E. Sutherland. “Pancreas transplantation.” *Lancet* 373.9677 (2009), 1808–1817.
- [67] E. A. Ryan et al. “Five-year follow-up after clinical islet transplantation.” *Diabetes* 54.7 (2005), 2060–2069.
- [68] A. M. J. Shapiro et al. “International trial of the Edmonton protocol for islet transplantation.” *The New England Journal of Medicine* 355.13 (2006), 1318–1330.
- [69] F. B. Barton et al. “Improvement in outcomes of clinical islet transplantation: 1999-2010.” *Diabetes Care* 35.7 (2012), 1436–1445.
- [70] Y. Lin and Z. Sun. “Current views on type 2 diabetes.” *The Journal of Endocrinology* 204.1 (2010), 1–11.
- [71] S. K. Thomsen and A. L. Gloyn. “The pancreatic β cell: recent insights from human genetics”. *Trends in Endocrinology & Metabolism* 25.8 (2014), 425–434.
- [72] A. Vetere, A. Choudhary, S. M. Burns, and B. K. Wagner. “Targeting the pancreatic β -cell to treat diabetes”. *Nature Reviews Drug Discovery* 13.4 (2014), 278–289.

Bibliography

- [73] S. S. Fajans, G. I. Bell, and K. S. Polonsky. “Molecular mechanisms and clinical pathophysiology of maturity-onset diabetes of the young.” *New England Journal of Medicine* 345.13 (2001), 971–980.
- [74] L. Hansen and O. Pedersen. “Genetics of type 2 diabetes mellitus: status and perspectives.” *Diabetes, Obesity and Metabolism* 7.2 (2005), 122–135.
- [75] Y. Reznik et al. “Hepatocyte nuclear factor-1 alpha gene inactivation: cosegregation between liver adenomatosis and diabetes phenotypes in two maturity-onset diabetes of the young (MODY) 3 families.” *The Journal of Clinical Endocrinology & Metabolism* 89.3 (2004), 1476–1480.
- [76] P. Igarashi, X. Shao, B. T. McNally, and T. k. I. Hiesberger. “Roles of HNF-1beta in kidney development and congenital cystic diseases.” *Kidney International* 68.5 (2005), 1944–1947.
- [77] C. Bingham and A. T. Hattersley. “Renal cysts and diabetes syndrome resulting from mutations in hepatocyte nuclear factor-1beta.” *Nephrology Dialysis Transplantation* 19.11 (2004), 2703–2708.
- [78] L. Aguilar-Bryan and J. Bryan. “Neonatal Diabetes Mellitus”. *Endocrine Reviews* 29.3 (2008), 265–291.
- [79] L. Bellamy, J.-P. Casas, A. D. Hingorani, and D. Williams. “Type 2 diabetes mellitus after gestational diabetes: a systematic review and meta-analysis.” *Lancet* 373.9677 (2009), 1773–1779.
- [80] A. J. F. King. “The use of animal models in diabetes research.” *British Journal of Pharmacology* 166.3 (2012), 877–894.
- [81] M. Gannon. “Molecular genetic analysis of diabetes in mice”. *Trends in Genetics* 17.10 (2001), S23–S28.
- [82] J. P. Mordes, R. Bortell, E. P. Blankenhorn, A. A. Rossini, and D. L. Greiner. “Rat models of type 1 diabetes: genetics, environment, and autoimmunity”. *Ilar Journal* 45.3 (2004), 278–291.
- [83] M. S. Anderson and J. A. Bluestone. “The NOD mouse: a model of immune dysregulation.” *Annual Review of Immunology* 23 (2005), 447–485.
- [84] P. Pozzilli, A. Signore, A. J. Williams, and P. E. Beales. “NOD mouse colonies around the world—recent facts and figures.” *Immunology Today* 14.5 (1993), 193–196.
- [85] G. B. Rudy, R. M. Sutherland, and A. M. Lew. “Temporal discontinuities in progression of NOD autoimmune diabetes”. *Immunologic Research* 16.2 (1997), 137–147.
- [86] S. Sreenan et al. “Increased beta-cell proliferation and reduced mass before diabetes onset in the nonobese diabetic mouse.” *Diabetes* 48.5 (1999), 989–996.
- [87] Y.-W. Wang et al. “Spontaneous Type 2 Diabetic Rodent Models”. *Journal of Diabetes Research* 2013 (2013).

-
- [88] D. Coleman. “Obese and diabetes: two mutant genes causing diabetes-obesity syndromes in mice”. *Diabetologia* 14.3 (1978), 141–148.
- [89] M. Shiota and R. Printz. “Diabetes in Zucker diabetic fatty rat”. *Animal Models in Diabetes Research*. Springer, 2012, pp. 103–123.
- [90] M. S. Winzell and B. Ahrén. “The high-fat diet-fed mouse: a model for studying mechanisms and treatment of impaired glucose tolerance and type 2 diabetes.” *Diabetes* 53.Suppl 3 (2004), S215–S219.
- [91] S. Lamprianou et al. “High-resolution magnetic resonance imaging quantitatively detects individual pancreatic islets.” *Diabetes* 60.11 (2011), 2853–2860.
- [92] D. Holmberg and U. Ahlgren. “Imaging the pancreas: from ex vivo to non-invasive technology.” *Diabetologia* 51.12 (2008), 2148–2154.
- [93] J. Virostko, E. D. Jansen, and A. C. Powers. “Current status of imaging pancreatic islets.” *Current Diabetes Reports* 6.4 (2006), 328–332.
- [94] D. Botsikas et al. “Pancreatic magnetic resonance imaging after manganese injection distinguishes type 2 diabetic and normoglycemic patients.” *Islets* 4.3 (2012), 243–248.
- [95] P. F. Antkowiak, B. K. Stevens, C. S. Nunemaker, M. McDuffie, and F. H. Epstein. “Manganese-enhanced magnetic resonance imaging detects declining pancreatic β -cell mass in a cyclophosphamide-accelerated mouse model of type 1 diabetes.” *Diabetes* 62.1 (2012), 44–48.
- [96] M. Brom, K. Andrałojć, W. J. G. Oyen, O. C. Boerman, and M. Gotthardt. “Development of radiotracers for the determination of the beta-cell mass in vivo.” *Current Pharmaceutical Design* 16.14 (2010), 1561–1567.
- [97] B. A. Blomberg, I. Codreanu, G. Cheng, T. J. Werner, and A. Alavi. “Beta-cell imaging: call for evidence-based and scientific approach.” *Molecular Imaging and Biology* 15.2 (2013), 123–130.
- [98] S.-Y. Park et al. “Optical imaging of pancreatic beta cells in living mice expressing a mouse insulin I promoter-firefly luciferase transgene.” *Genesis* 43.2 (2005), 80–86.
- [99] D. Sever et al. “Evaluation of impaired β -cell function in nonobese-diabetic (NOD) mouse model using bioluminescence imaging”. *The FASEB Journal* 25.2 (2011), 676–684.
- [100] S.-Y. Park and G. I. Bell. “Noninvasive monitoring of changes in pancreatic beta-cell mass by bioluminescent imaging in MIP-luc transgenic mice.” *Hormone and Metabolic Research* 41.1 (2009), 1–4.
- [101] T. Katsumata et al. “Bioluminescence imaging of β cells and intrahepatic insulin gene activity under normal and pathological conditions.” *PloS One* 8.4 (2013), e60411.

Bibliography

- [102] M. Hara et al. “Transgenic mice with green fluorescent protein-labeled pancreatic beta -cells.” *American Journal of Physiology-Endocrinology and Metabolism* 284.1 (2003), E177–E183.
- [103] M. Hara et al. “Imaging pancreatic beta-cells in the intact pancreas.” *American Journal of Physiology-Endocrinology and Metabolism* 290.5 (2006), 2569–2578.
- [104] K. Coppieters, M. M. Martinic, W. B. Kiosses, N. Amirian, and M. von Herrath. “A novel technique for the in vivo imaging of autoimmune diabetes development in the pancreas by two-photon microscopy.” *PloS One* 5.12 (2010), e15732.
- [105] T. Alanentalo et al. “Tomographic molecular imaging and 3D quantification within adult mouse organs.” *Nature Methods* 4.1 (2007), 31–33.
- [106] T. Alanentalo et al. “High-resolution three-dimensional imaging of islet-infiltrate interactions based on optical projection tomography assessments of the intact adult mouse pancreas.” *Journal of Biomedical Optics* 13.5 (2008), 054070–054070–4.
- [107] M. Villiger et al. “In vivo imaging of murine endocrine islets of Langerhans with extended-focus optical coherence microscopy.” *Diabetologia* 52.8 (2009), 1599–1607.
- [108] S. Speier et al. “Noninvasive in vivo imaging of pancreatic islet cell biology.” *Nature Medicine* 14.5 (2008), 574–578.
- [109] D. Nyqvist, M. Köhler, H. Wahlstedt, and P.-O. Berggren. “Donor islet endothelial cells participate in formation of functional vessels within pancreatic islet grafts.” *Diabetes* 54.8 (2005), 2287–2293.
- [110] M. H. Abdulreda et al. “High-resolution, noninvasive longitudinal live imaging of immune responses.” *Proceedings of the National Academy of Sciences of the United States of America* 108.31 (2011), 12863–12868.
- [111] A. Schmidt-Christensen et al. “Imaging dynamics of CD11c+ cells and Foxp3+ cells in progressive autoimmune insulinitis in the NOD mouse model of type 1 diabetes.” *Diabetologia* 56.12 (2013), 2669–2678.
- [112] M. Mojibian et al. “Implanted islets in the anterior chamber of the eye are prone to autoimmune attack in a mouse model of diabetes.” *Diabetologia* 56.10 (2013), 2213–2221.
- [113] E. Ilegems et al. “Reporter islets in the eye reveal the plasticity of the endocrine pancreas.” *Proceedings of the National Academy of Sciences of the United States of America* 110.51 (2013), 20581–20586.
- [114] H. Chmelova et al. “Distinct roles of beta cell mass and function during type 1 diabetes onset and remission.” *Diabetes* (2015), db141055.
- [115] V. L. Perez et al. “The anterior chamber of the eye as a clinical transplantation site for the treatment of diabetes: a study in a baboon model of diabetes.” *Diabetologia* 54.5 (2011), 1121–1126.

-
- [116] L. Jansson, A. Andersson, B. Bodin, and O. Källskog. “Pancreatic islet blood flow during euglycaemic, hyperinsulinaemic clamp in anaesthetized rats.” *Acta Physiologica* 189.4 (2007), 319–324.
- [117] S. Moldovan et al. “Glucose-induced islet hyperemia is mediated by nitric oxide.” *American Journal of Surgery* 171.1 (1996), 16–20.
- [118] M. D. Menger, P. Vajkoczy, R. Leiderer, S. Jäger, and K. Messmer. “Influence of experimental hyperglycemia on microvascular blood perfusion of pancreatic islet isografts.” *The Journal of Clinical Investigation* 90.4 (1992), 1361–1369.
- [119] O. Sabek et al. “Imaging of human islet vascularization using a dorsal window model.” *Transplantation Proceedings* 42.6 (2010), 2112–2114.
- [120] R. Nishimura et al. “Tacrolimus inhibits the revascularization of isolated pancreatic islets.” *PloS One* 8.4 (2013), e56799.
- [121] Z. Medarova et al. “Imaging the pancreatic vasculature in diabetes models”. *Diabetes Metabolism Research and Reviews* 27.8 (2011), 767–772.
- [122] B. Saleh and M. Teich. *Fundamentals of Photonics*. Wiley Series in Pure and Applied Optics. Wiley, 2013.
- [123] R. Leitgeb, M. Villiger, A. Bachmann, L. Steinmann, and T. Lasser. “Extended focus depth for Fourier domain optical coherence microscopy.” *Optics Letters* 31.16 (2006), 2450–2452.
- [124] W. Drexler and J. Fujimoto. “State-of-the-art retinal optical coherence tomography”. *Progress in Retinal and Eye Research* 27.1 (2008), 45–88.
- [125] H. G. Bezerra, M. A. Costa, G. Guagliumi, A. M. Rollins, and D. I. Simon. “Intracoronary optical coherence tomography: a comprehensive review clinical and research applications.” *Journal of the American College of Cardiology* 2.11 (2009), 1035–1046.
- [126] L. L. Otis, M. J. Everett, U. S. Sathyam, and B. W. Colston. “Optical coherence tomography: a new imaging technology for dentistry”. *Journal of the American Dental Association* 131.4 (2000), 511–514.
- [127] E. Sattler, R. Kästle, and J. Welzel. “Optical coherence tomography in dermatology”. *Journal of Biomedical Optics* 18.6 (2013), 061224–061224.
- [128] T. Bolmont et al. “Label-Free Imaging of Cerebral -Amyloidosis with Extended-Focus Optical Coherence Microscopy”. *Journal of Neuroscience* 32.42 (2012), 14548–14556.
- [129] M. Villiger, C. Pache, and T. Lasser. “Dark-field optical coherence microscopy”. *Optics Letters* 35.20 (2010), 3489–3491.
- [130] T. F. Chan and L. A. Vese. “Active contours without edges”. *IEEE Transactions on Image Processing* 10.2 (2001), 266–277.

Bibliography

- [131] American Diabetes Association. “Diagnosis and classification of diabetes mellitus.” *Diabetes Care* 34.Suppl 1 (2011), S62–S69.
- [132] P. F. Antkowiak, M. H. Vandsburger, and F. H. Epstein. “Quantitative pancreatic β cell MRI using manganese-enhanced Look-Locker imaging and two-site water exchange analysis.” *Magnetic Resonance in Medicine* 67.6 (2012), 1730–1739.
- [133] F. Souza et al. “Longitudinal noninvasive PET-based beta cell mass estimates in a spontaneous diabetes rat model.” *The Journal of Clinical Investigation* 116.6 (2006), 1506–1513.
- [134] D. Wild et al. “Exendin-4-based radiopharmaceuticals for glucagonlike peptide-1 receptor PET/CT and SPECT/CT.” *Journal of Nuclear Medicine* 51.7 (2010), 1059–1067.
- [135] M. M. Martinic and M. G. von Herrath. “Real-time imaging of the pancreas during development of diabetes.” *Immunological Reviews* 221.1 (2008), 200–213.
- [136] A. Fercher, W. Drexler, C. Hitzenberger, and T. Lasser. “Optical coherence tomography-principles and applications”. *Reports on Progress in Physics* 66.2 (2003), 239.
- [137] J. G. Fujimoto. “Optical coherence tomography for ultrahigh resolution in vivo imaging.” *Nature Biotechnology* 21.11 (2003), 1361–1367.
- [138] J. A. Izatt, M. R. Hee, G. M. Owen, E. A. Swanson, and J. G. Fujimoto. “Optical coherence microscopy in scattering media.” *Optics Letters* 19.8 (1994), 590–592.
- [139] G. J. Tearney et al. “Optical biopsy in human pancreatobiliary tissue using optical coherence tomography.” *Digestive Diseases and Sciences* 43.6 (1998), 1193–1199.
- [140] P. A. Testoni et al. “Optical coherence tomography compared with histology of the main pancreatic duct structure in normal and pathological conditions: an ‘ex vivo study’.” *Digestive and Liver Disease* 38.9 (2006), 688–695.
- [141] N. A. Iftimia et al. “Differentiation of pancreatic cysts with optical coherence tomography (OCT) imaging: an ex vivo pilot study”. *Biomedical Optics Express* 2.8 (2011), 2372–2382.
- [142] Y. Hori et al. “Automatic characterization and segmentation of human skin using three-dimensional optical coherence tomography.” *Optics Express* 14.5 (2006), 1862–1877.
- [143] S. J. Chiu et al. “Automatic segmentation of seven retinal layers in SDOCT images congruent with expert manual segmentation”. *Optics Express* 18.18 (2010), 19413–19428.
- [144] I. Ghorbel, F. Rossant, I. Bloch, S. Tick, and M. Paques. “Automated segmentation of macular layers in OCT images and quantitative evaluation of performances”. *Pattern Recognition* 44.8 (2011), 1590–1603.

-
- [145] H. Nagai. “Configurational anatomy of the pancreas: its surgical relevance from ontogenetic and comparative-anatomical viewpoints”. *Journal of Hepato-Biliary-Pancreatic Surgery* 10.1 (2003), 48–56.
- [146] L. D. Shultz et al. “Human lymphoid and myeloid cell development in NOD/LtSz-scid IL2R γ null mice engrafted with mobilized human hemopoietic stem cells”. *The Journal of Immunology* 174.10 (2005), 6477–6489.
- [147] S. Osher and R. P. Fedkiw. *Level Set Methods and Dynamic Implicit Surfaces*. Springer, 2003.
- [148] R. T. Whitaker. “A level-set approach to 3D reconstruction from range data”. *International Journal of Computer Vision* 29.3 (1998), 203–231.
- [149] S. Lankton. *Sparse Field Methods*. Tech. rep. Georgia institute of technology, 2009.
- [150] J. Malcolm, Y. Rathi, A. Yezzi, and A. Tannenbaum. “Fast approximate surface evolution in arbitrary dimension”. *Medical Imaging*. International Society for Optics and Photonics. 2008, pp. 69144C–69144C.
- [151] A. C. Davison and D. V. Hinkley. *Bootstrap methods and their application*. Vol. 1. Cambridge University Press, 1997.
- [152] T. Bock, K. Svenstrup, B. Pakkenberg, and K. Buschard. “Unbiased estimation of total β -cell number and mean β -cell volume in rodent pancreas.” *APMIS* 107.7-12 (1999), 791–799.
- [153] A. Clauset and C. R. Shalizi. “Power-law distributions in empirical data”. *SIAM Review* 51.4 (2009), 661–703.
- [154] T. Bock, B. Pakkenberg, and K. Buschard. “Increased islet volume but unchanged islet number in ob/ob mice.” *Diabetes* 52.7 (2003), 1716–1722.
- [155] P. O. Bastien-Dionne, L. Valenti, N. Kon, W. Gu, and J. Buteau. “Glucagon-like peptide 1 inhibits the sirtuin deacetylase SirT1 to stimulate pancreatic β -cell mass expansion”. *Diabetes* 60.12 (2011), 3217–3222.
- [156] S. Hamada et al. “Upregulation of the mammalian target of rapamycin complex 1 pathway by ras homolog enriched in brain in pancreatic β -cells leads to increased β -cell mass and prevention of hyperglycemia”. *Diabetes* 58.6 (2009), 1321–1332.
- [157] M. Riopel et al. “Conditional β 1-integrin-deficient mice display impaired pancreatic β cell function.” *The Journal of Pathology* 224.1 (2011), 45–55.
- [158] P. L. Bollyky et al. “The toll-like receptor signaling molecule Myd88 contributes to pancreatic beta-cell homeostasis in response to injury.” *PloS One* 4.4 (2009), e5063.
- [159] D. Choi, E. P. Cai, S. A. Schroer, L. Wang, and M. Woo. “Vhl is required for normal pancreatic β cell function and the maintenance of β cell mass with age in mice.” *Laboratory Investigation* 91.4 (2011), 527–538.

Bibliography

- [160] M. Chintinne et al. "Contribution of postnatally formed small beta cell aggregates to functional beta cell mass in adult rat pancreas." *Diabetologia* 53.11 (2010), 2380–2388.
- [161] C. Berclaz et al. "Diabetes imaging-quantitative assessment of islets of Langerhans distribution in murine pancreas using extended-focus optical coherence microscopy." *Biomedical Optics Express* 3.6 (2012), 1365–1380.
- [162] R. K. Wang, L. An, P. Francis, and D. J. Wilson. "Depth-resolved imaging of capillary networks in retina and choroid using ultrahigh sensitive optical microangiography." *Optics Letters* 35.9 (2010), 1467–1469.
- [163] V. J. Srinivasan et al. "Quantitative cerebral blood flow with optical coherence tomography." *Optics Express* 18.3 (2010), 2477–2494.
- [164] L. An, J. Qin, and R. K. Wang. "Ultrahigh sensitive optical microangiography for in vivo imaging of microcirculations within human skin tissue beds." *Optics Express* 18.8 (2010), 8220–8228.
- [165] A. Szkulmowska, M. Szkulmowski, D. Szlag, A. Kowalczyk, and M. Wojtkowski. "Three-dimensional quantitative imaging of retinal and choroidal blood flow velocity using joint Spectral and Time domain Optical Coherence Tomography." *Optics Express* 17.13 (2009), 10584–10598.
- [166] V. J. Srinivasan et al. "Rapid volumetric angiography of cortical microvasculature with optical coherence tomography." *Optics Letters* 35.1 (2010), 43–45.
- [167] A. Bouwens, T. Bolmont, D. Szlag, C. Berclaz, and T. Lasser. "Quantitative cerebral blood flow imaging with extended-focus optical coherence microscopy." *Optics Letters* 39.1 (2013), 37–40.
- [168] D. Szlag. "Development of methods for Optical Coherence Microscopy". PhD thesis. Nicolaus Copernicus University, Torun, Poland, 2014.
- [169] C. Dai et al. "Pancreatic islet vasculature adapts to insulin resistance through dilation and not angiogenesis". *Diabetes* 62.12 (2013), 4144–4153.
- [170] J. L. Gaglia et al. "Noninvasive imaging of pancreatic islet inflammation in type 1A diabetes patients." *The Journal of Clinical Investigation* 121.1 (2011), 442–445.
- [171] P.-O. Carlsson, F. Palm, and G. Mattsson. "Low revascularization of experimentally transplanted human pancreatic islets". *The Journal of Clinical Endocrinology & Metabolism* 87.12 (2013), 5418–5423.
- [172] G. Mattsson, L. Jansson, and P.-O. Carlsson. "Decreased vascular density in mouse pancreatic islets after transplantation." *Diabetes* 51.5 (2002), 1362–1366.
- [173] G. Christoffersson et al. "Clinical and experimental pancreatic islet transplantation to striated muscle: establishment of a vascular system similar to that in native islets." *Diabetes* 59.10 (2010), 2569–2578.

-
- [174] J. Henriksnäs et al. “Markedly decreased blood perfusion of pancreatic islets transplanted intraportally into the liver: disruption of islet integrity necessary for islet revascularization.” *Diabetes* 61.3 (2012), 665–673.
- [175] J. Almagea et al. “Young capillary vessels rejuvenate aged pancreatic islets.” *Proceedings of the National Academy of Sciences of the United States of America* 111.49 (2014), 17612–17617.
- [176] Y.-Y. Fu et al. “Three-dimensional optical method for integrated visualization of mouse islet microstructure and vascular network with subcellular-level resolution.” *Journal of Biomedical Optics* 15.4 (2010), 046018–046018–9.
- [177] Y. El-Gohary et al. “Three-dimensional analysis of the islet vasculature.” *The Anatomical Record* 295.9 (2012), 1473–1481.
- [178] T. Murakami et al. “Blood flow patterns in the rat pancreas: a simulative demonstration by injection replication and scanning electron microscopy.” *Microscopy Research and Technique* 37.5-6 (1997), 497–508.
- [179] M. D. Menger et al. “Angiogenesis and Hemodynamics of Microvasculature of Transplanted Islets of Langerhans”. *Diabetes* 38.Suppl 1 (1989), 199–201.
- [180] B. J. Vakoc et al. “Three-dimensional microscopy of the tumor microenvironment in vivo using optical frequency domain imaging.” *Nature Medicine* 15.10 (2009), 1219–1223.
- [181] M. Szkulmowski, A. Szkulmowska, T. Bajraszewski, A. Kowalczyk, and M. Wojtkowski. “Flow velocity estimation using joint Spectral and Time domain Optical Coherence Tomography.” *Optics Express* 16.9 (2008), 6008–6025.
- [182] J. Walther and E. Koch. “Enhanced joint spectral and time domain optical coherence tomography for quantitative flow velocity measurement”. *European Conferences on Biomedical Optics*. International Society for Optics and Photonics. 2011, p. 80910L.
- [183] J. A. Ben Janssen et al. “Effects of anesthetics on systemic hemodynamics in mice.” *American Journal of Physiology-Heart and Circulatory Physiology* 287.4 (2004), H1618–H1624.
- [184] R. B. Reinert et al. “Vascular endothelial growth factor coordinates islet innervation via vascular scaffolding.” *Development* 141.7 (2014), 1480–1491.
- [185] W. S. Kamoun et al. “Simultaneous measurement of RBC velocity, flux, hematocrit and shear rate in vascular networks”. *Nature Methods* 7.8 (2010), 655–660.
- [186] E. Chaigneau, M. Oheim, E. Audinat, and S. Charpak. “Two-photon imaging of capillary blood flow in olfactory bulb glomeruli.” *Proceedings of the National Academy of Sciences of the United States of America* 100.22 (2003), 13081–13086.
- [187] A. Y. Shih et al. “Two-photon microscopy as a tool to study blood flow and neurovascular coupling in the rodent brain.” *Journal of Cerebral Blood Flow and Metabolism* 32.7 (2012), 1277–1309.

Bibliography

- [188] H. Radhakrishnan and V. J. Srinivasan. “Compartment-resolved imaging of cortical functional hyperemia with OCT angiography.” *Biomedical Optics Express* 4.8 (2013), 1255–1268.
- [189] A. Bouwens et al. “Quantitative lateral and axial flow imaging with optical coherence microscopy and tomography”. *Optics Express* 21.15 (2013), 17711–17729.
- [190] Y. Pan, J. You, N. D. Volkow, K. Park, and C. Du. “Ultrasensitive detection of 3D cerebral microvascular network dynamics in vivo.” *NeuroImage* 103 (2014), 492–501.
- [191] I. R. Sweet et al. “Systematic screening of potential beta-cell imaging agents.” *Biochemical and Biophysical Research Communications* 314.4 (2004), 976–983.
- [192] M. P. Kung et al. “In vivo imaging of beta-cell mass in rats using 18F-FP-(+)-DTBZ: a potential PET ligand for studying diabetes mellitus.” *Journal of Nuclear Medicine* 49.7 (2008), 1171–1176.
- [193] N. R. Simpson et al. “Visualizing pancreatic β -cell mass with [11C]DTBZ.” *Nuclear Medicine and Biology* 33.7 (2006), 855–864.
- [194] J. Virostko et al. “Multimodal image coregistration and inducible selective cell ablation to evaluate imaging ligands.” *Proceedings of the National Academy of Sciences of the United States of America* 108.51 (2011), 20719–20724.
- [195] R. Goland et al. “11C-dihydrotetrabenazine PET of the pancreas in subjects with long-standing type 1 diabetes and in healthy controls.” *Journal of Nuclear Medicine* 50.3 (2009), 382–389.
- [196] Y. Saisho et al. “Relationship between pancreatic vesicular monoamine transporter 2 (VMAT2) and insulin expression in human pancreas.” *Journal of Molecular Histology* 39.5 (2008), 543–551.
- [197] Q. Mei, T. O. Mundinger, A. Lernmark, and G. J. Taborsky. “Early, selective, and marked loss of sympathetic nerves from the islets of BioBreeder diabetic rats.” *Diabetes* 51.10 (2002), 2997–3002.
- [198] M. K.-H. Schäfer et al. “Species-specific vesicular monoamine transporter 2 (VMAT2) expression in mammalian pancreatic beta cells: implications for optimising radioligand-based human beta cell mass (BCM) imaging in animal models.” *Diabetologia* 56.5 (2013), 1047–1056.
- [199] J. J. Meier and M. A. Nauck. “Glucagon-like peptide 1(GLP-1) in biology and pathology.” *Diabetes Metabolism Research and Reviews* 21.2 (2005), 91–117.
- [200] B. Ahrén. “GLP-1 for type 2 diabetes.” *Experimental Cell Research* 317.9 (2011), 1239–1245.
- [201] Y. Wei and S. Mojsov. “Tissue-specific expression of the human receptor for glucagon-like peptide-I: brain, heart and pancreatic forms have the same deduced amino acid sequences.” *FEBS Letters* 358.3 (1995), 219–224.

-
- [202] J. L. Dunphy, R. G. Taylor, and P. J. Fuller. "Tissue distribution of rat glucagon receptor and GLP-1 receptor gene expression." *Molecular and Cellular Endocrinology* 141.1-2 (1998), 179–186.
- [203] M. Körner, M. Stöckli, B. Waser, and J. C. Reubi. "GLP-1 receptor expression in human tumors and human normal tissues: potential for in vivo targeting." *Journal of Nuclear Medicine* 48.5 (2007), 736–743.
- [204] D. Tornehave, P. Kristensen, J. Rømer, L. B. Knudsen, and R. S. Heller. "Expression of the GLP-1 receptor in mouse, rat, and human pancreas." *Journal of Histochemistry & Cytochemistry* 56.9 (2008), 841–851.
- [205] C. Pyke et al. "GLP-1 receptor localization in monkey and human tissue: novel distribution revealed with extensively validated monoclonal antibody." *Endocrinology* 155.4 (2014), 1280–1290.
- [206] R. S. Heller, T. J. Kieffer, and J. F. Habener. "Insulinotropic glucagon-like peptide I receptor expression in glucagon-producing alpha-cells of the rat endocrine pancreas." *Diabetes* 46.5 (1997), 785–791.
- [207] S. N. Roed et al. "Real-time trafficking and signaling of the glucagon-like peptide-1 receptor." *Molecular and Cellular Endocrinology* 382.2 (2014), 938–949.
- [208] B. M. Connolly et al. "Ex vivo imaging of pancreatic beta cells using a radiolabeled GLP-1 receptor agonist." *Molecular Imaging and Biology* 14.1 (2012), 79–87.
- [209] Z. Wu et al. "In vivo imaging of transplanted islets with ^{64}Cu -DO3A-VS-Cys40-Exendin-4 by targeting GLP-1 receptor." *Bioconjugate Chemistry* 22.8 (2011), 1587–1594.
- [210] Y. Wang et al. "Synthesis and evaluation of ^{18}F exendin (9–39) as a potential biomarker to measure pancreatic β -cell mass". *Nuclear Medicine and Biology* 39.2 (2012), 167–176.
- [211] Z. Wu et al. "Development and evaluation of ^{18}F -TTCO-Cys40-Exendin-4: a PET probe for imaging transplanted islets." *Journal of Nuclear Medicine* 54.2 (2013), 244–251.
- [212] K. Mikkola et al. " ^{64}Cu - and ^{68}Ga -labelled $[\text{Nle}(14),\text{Lys}(40)(\text{Ahx-NODAGA})\text{NH}_2]$ -exendin-4 for pancreatic beta cell imaging in rats." *Molecular Imaging and Biology* 16.2 (2014), 255–263.
- [213] M. Brom et al. "Non-invasive quantification of the beta cell mass by SPECT with ^{111}In -labelled exendin." *Diabetologia* 57.5 (2014), 950–959.
- [214] I. Mathijs et al. "A standardized method for in vivo mouse pancreas imaging and semiquantitative β cell mass measurement by dual isotope SPECT." *Molecular Imaging and Biology* 17.1 (2015), 58–66.
- [215] P. Wang et al. "GLP-1R-targeting magnetic nanoparticles for pancreatic islet imaging." *Diabetes* 63.5 (2014), 1465–1474.

Bibliography

- [216] L. Vinet et al. “Targeting GLP-1 receptors for repeated magnetic resonance imaging differentiates graded losses of pancreatic beta cells in mice”. *Diabetologia* 58.2 (2015), 304–312.
- [217] T. Reiner et al. “Accurate measurement of pancreatic islet beta-cell mass using a second-generation fluorescent exendin-4 analog.” *Proceedings of the National Academy of Sciences of the United States of America* 108.31 (2011), 12815–12820.
- [218] S. M. Clardy et al. “Fluorescent exendin-4 derivatives for pancreatic β -cell analysis.” *Bioconjugate Chemistry* 25.1 (2014), 171–177.
- [219] L. Nalin et al. “Positron emission tomography imaging of the glucagon-like peptide-1 receptor in healthy and streptozotocin-induced diabetic pigs”. *European Journal of Nuclear Medicine and Molecular Imaging* 41.9 (2014), 1800–1810.
- [220] R. K. Selvaraju et al. “In vivo imaging of the glucagonlike peptide 1 receptor in the pancreas with 68Ga-labeled DO3A-exendin-4.” *Journal of Nuclear Medicine* 54.8 (2013), 1458–1463.
- [221] C. Brand et al. “In Vivo Imaging of GLP-1R with a Targeted Bimodal PET/Fluorescence Imaging Agent.” *Bioconjugate Chemistry* 25.7 (2014), 1323–1330.
- [222] M. Gotthardt et al. “Use of the incretin hormone glucagon-like peptide-1 (GLP-1) for the detection of insulinomas: initial experimental results.” *European Journal of Nuclear Medicine and Molecular Imaging* 29.5 (2002), 597–606.
- [223] D. Wild et al. “[Lys40(Ahx-DTPA-111In)NH₂]exendin-4, a very promising ligand for glucagon-like peptide-1 (GLP-1) receptor targeting.” *Journal of Nuclear Medicine* 47.12 (2006), 2025–2033.
- [224] M. Brom, W. J. G. Oyen, L. Joosten, M. Gotthardt, and O. C. Boerman. “68Ga-labelled exendin-3, a new agent for the detection of insulinomas with PET.” *European Journal of Nuclear Medicine and Molecular Imaging* 37.7 (2010), 1345–1355.
- [225] E. Mukai et al. “GLP-1 receptor antagonist as a potential probe for pancreatic β -cell imaging”. *Biochemical and Biophysical Research Communications* 389.3 (2009), 523–526.
- [226] B. Waser and J. C. Reubi. “Radiolabelled GLP-1 receptor antagonist binds to GLP-1 receptor-expressing human tissues”. *European Journal of Nuclear Medicine and Molecular Imaging* 41.6 (2014), 1166–1171.
- [227] K. Andralojc et al. “Obstacles on the way to the clinical visualisation of beta cells: looking for the Aeneas of molecular imaging to navigate between Scylla and Charybdis”. *Diabetologia* 55.5 (2012), 1247–1257.
- [228] P. Richards et al. “Identification and characterization of GLP-1 receptor-expressing cells using a new transgenic mouse model.” *Diabetes* 63.4 (2014), 1224–1233.

-
- [229] B. van Eyll, B. Lankat-Buttgereit, and H. P. Bode. "Signal transduction of the GLP-1-receptor cloned from a human insulinoma". *FEBS Letters* 348.1 (1994), 7–13.
- [230] T. Reiner et al. "Near-Infrared Fluorescent Probe for Imaging of Pancreatic β Cells". *Bioconjugate Chemistry* 21.7 (2010), 1362–1368.
- [231] J. Lee, V. Srinivasan, H. Radhakrishnan, and D. A. Boas. "Motion correction for phase-resolved dynamic optical coherence tomography imaging of rodent cerebral cortex". *Optics Express* 19.22 (2011), 21258–21270.
- [232] P.-O. Carlsson, S. Sandler, and L. Jansson. "Pancreatic islet blood perfusion in the nonobese diabetic mouse: diabetes-prone female mice exhibit a higher blood flow compared with male mice in the prediabetic phase". *Endocrinology* 139.8 (1998), 3534–3541.
- [233] G. Papaccio, F. A. Pisanti, R. D. Montefiano, A. Graziano, and M. V. Latronico. "Th1 and Th2 cytokines exert regulatory effects upon islet microvascular areas in the NOD mouse". *Journal of Cellular Biochemistry* 86.4 (2002), 651–664.
- [234] J. S. Pober and R. S. Cotran. "The role of endothelial cells in inflammation." *Transplantation* 50.4 (1990), 537–544.
- [235] M. C. Denis, U. Mahmood, C. Benoist, D. Mathis, and R. Weissleder. "Imaging inflammation of the pancreatic islets in type 1 diabetes." *Proceedings of the National Academy of Sciences of the United States of America* 101.34 (2004), 12634–12639.
- [236] K. Coppieters, N. Amirian, and M. von Herrath. "Intravital imaging of CTLs killing islet cells in diabetic mice". *The Journal of Clinical Investigation* 122.1 (2012), 119–131.
- [237] K. Lemaire, F. Chimienti, and F. Schuit. "Zinc transporters and their role in the pancreatic β -cell." *Journal of Diabetes Investigation* 3.3 (2012), 202–211.
- [238] K. Lemaire et al. "Insulin crystallization depends on zinc transporter ZnT8 expression but is not required for normal glucose homeostasis in mice." *Proceedings of the National Academy of Sciences of the United States of America* 106.35 (2009), 14872–14877.
- [239] J. M. Conlon. "Evolution of the insulin molecule: insights into structure-activity and phylogenetic relationships." *Peptides* 22.7 (2001), 1183–1193.
- [240] R. E. Mebius, P. R. Streeter, S. Michie, E. C. Butcher, and I. L. Weissman. "A developmental switch in lymphocyte homing receptor and endothelial vascular addressin expression regulates lymphocyte homing and permits CD4⁺ CD3⁻ cells to colonize lymph nodes". *Proceedings of the National Academy of Sciences* 93.20 (1996), 11019–11024.

Bibliography

- [241] A. Hanninen, C. Taylor, and P. Streeter. “Vascular addressins are induced on islet vessels during insulinitis in nonobese diabetic mice and are involved in lymphoid cell binding to islet endothelium.” *The Journal of Clinical Investigation* 92.5 (1993), 2509–2515.
- [242] A. Hanninen, I. Jaakkola, and S. Jalkanen. “Mucosal addressin is required for the development of diabetes in nonobese diabetic mice”. *The Journal of Immunology* 160.12 (1998), 6018–6025.
- [243] C. Faveeuw, M. C. Gagnerault, and F. Lepault. “Expression of homing and adhesion molecules in infiltrated islets of Langerhans and salivary glands of nonobese diabetic mice.” *The Journal of Immunology* 152.12 (1994), 5969–5978.
- [244] D. Huang, E. Swanson, and C. Lin. “Optical coherence tomography”. *Science* 254.5035 (1991), 1178–1181.
- [245] S. Yun, G. Tearney, J. de Boer, N. Iftimia, and B. Bouma. “High-speed optical frequency-domain imaging”. *Optics Express* 11.22 (2003), 2953–2963.
- [246] I. Söderström et al. “Establishment and Characterization of RAG-2 Deficient Non-Obese Diabetic Mice.” *Scandinavian Journal of Immunology* 43.5 (1996), 525–530.
- [247] M. Guizar-Sicairos, S. T. Thurman, and J. R. Fienup. “Efficient subpixel image registration algorithms.” *Optics Letters* 33.2 (2008), 156–158.
- [248] F. Luisier, C. Vonesch, T. Blu, and M. Unser. “Fast interscale wavelet denoising of Poisson-corrupted images”. *Signal Processing* 90.2 (2010), 415–427.
- [249] M. J. A. Girard, N. G. Strouthidis, C. R. Ethier, and J. M. Mari. “Shadow Removal and Contrast Enhancement in Optical Coherence Tomography Images of the Human Optic Nerve Head”. *Investigative Ophthalmology & Visual Science* 52.10 (2011), 7738–7748.
- [250] M. Teta, S. Y. Long, L. M. Wartschow, M. M. Rankin, and J. A. Kushner. “Very slow turnover of beta-cells in aged adult mice.” *Diabetes* 54.9 (2005), 2557–2567.
- [251] M. M. Rankin and J. A. Kushner. “Adaptive beta-cell proliferation is severely restricted with advanced age.” *Diabetes* 58.6 (2009), 1365–1372.
- [252] M. Stolovich-Rain, A. Hija, J. Grimsby, B. Glaser, and Y. Dor. “Pancreatic beta cells in very old mice retain capacity for compensatory proliferation.” *The Journal of Biological Chemistry* 287.33 (2012), 27407–27414.
- [253] J. Kushner. “The role of aging upon β cell turnover.” *The Journal of Clinical Investigation* 123.3 (2013), 990–995.
- [254] P. I. Veld. “Insulinitis in human type 1 diabetes: a comparison between patients and animal models.” *Seminars in Immunopathology* 36.5 (2014), 569–579.
- [255] J. C. Reed and K. C. Herold. “Thinking bedside at the bench: the NOD mouse model of T1DM.” *Nature Reviews Endocrinology* Advance online publication (2015).

Curriculum Vitae

Corinne Berclaz

Date of birth: 28. March 1986
Email: corinne.berclaz@a3.epfl.ch
Citizenship: Switzerland

Education

- 2010-2015 Ph.D. student in the Laboratoire d'Optique Biomédicale
Supervisors: Prof. Theo Lasser and Prof. Anne Grapin-Botton
Doctoral School of Photonics
École Polytechnique Fédérale de Lausanne (EPFL)
- 2009-2010 M.Sc. in Biotechnology and Bioengineering
Minor in Biomedical Technologies
Best Master Project in Biomedical Technologies
Excellency Mention for the quality of the Master studies
École Polytechnique Fédérale de Lausanne (EPFL)
- 2005-2008 B.Sc. in Life Sciences and Technologies
École Polytechnique Fédérale de Lausanne (EPFL)

Teaching and Supervision

Supervision of student projects

- Optical coherence microscopy characterization of the ear skin as a new site of graft for islets of Langerhans, Xavier Blanc, 2011
- Optical Coherence Microscopy to image entire mouse pancreas in 3D, Manon Rostykus, 2012
- Characterization of the signal obtained from the islets of Langerhans in Optical Coherence Microscopy, Vivien Meyer, 2014

Teaching assistant

- Biomicroscopy I, Master course, Prof. Theo Lasser (1 semester)
- Biomicroscopy II, Master course, Prof. Theo Lasser (2 semesters)
- Imaging Optics, Master course, Prof. Theo Lasser (1 semester)

Peer-reviewed publications

1. “Diabetes imaging — quantitative assessment of islets of Langerhans distribution in murine pancreas using extended-focus optical coherence microscopy”, **Corinne Berclaz**, Joan Goulley, Martin Villiger, Christophe Pache, Arno Bouwens, Erica William-Martin, Dimitri Van de Ville, Anthony C. Davison, Anne Grapin-Botton and Theo Lasser; Biomedical Optics Express, 3(6):1365-80 (2012).
2. “Label-Free Imaging of Cerebral-Amyloidosis with Extended-Focus Optical Coherence Microscopy”, Tristan Bolmont, Arno Bouwens, Christophe Pache, Mitko Dimitrov, **Corinne Berclaz**, Martin Villiger, Bettina Wegenast-Braun, Theo Lasser, and Patrick C. Fraering; Journal of Neuroscience, 32(42):14548-14556 (2012).
3. “Mapping molecular statistics with balanced super-resolution optical fluctuation imaging (bSOFI)”, Stefan Geissbuehler, Noelia L. Bocchio, Claudio Dellagicama, **Corinne Berclaz**, Marcel Leutenegger, and Theo Lasser; Optical Nanoscopy, 1(4):1-7 (2012).
4. “Fast three-dimensional imaging of gold nanoparticles in living cells with photothermal optical lock-in Optical Coherence Microscopy”, Christophe Pache, Noelia L. Bocchio, Arno Bouwens, Martin Villiger, **Corinne Berclaz**, Joan Goulley, Matthew I. Gibson, Christian Santschi, and Theo Lasser; Optics Express, 20(19):21385-99 (2012).
5. “Quantitative cerebral blood flow imaging with extended-focus optical coherence microscopy”, Arno Bouwens, Tristan Bolmont, Daniel Szlag, **Corinne Berclaz** and Theo Lasser; Optics Letters, 39(1):37-40 (2013).
6. “Combined Optical Coherence and Fluorescence Microscopy to assess dynamics and specificity of pancreatic beta-cell tracers”, **Corinne Berclaz**, Christophe Pache, Arno Bouwens, Daniel Szlag, Antonio Lopez, Lieke Joosten, Selen Ekim, Maarten Brom, Martin Gotthardt, Anne Grapin-Botton, and Theo Lasser; Accepted in Scientific Reports (2015).

Conference contributions

1. **Corinne Berclaz**, Joan Goulley, Christophe Pache, Arno Bouwens, Erica Martin-William, Martin Villiger, Anne Grapin-Botton, Theo Lasser “xfOCM for the assessment of type I diabetes”. Talk presented at the European conferences on Biomedical Optics, Munich 2011.
2. **Corinne Berclaz**, Christophe Pache, Arno Bouwens, Antonio Lopez, Anne Grapin-Botton, Theo Lasser “Towards diabetes imaging based on optical coherence microscopy and confocal fluorescence imaging”. Talk presented at the BIOS conference, San Francisco, 2013.

3. **Corinne Berclaz**, Daniel Szlag, Arno Bouwens, Anne Grapin-Botton, and Theo Lasser “Blood flow and vascular network imaging inside the pancreas and islets of Langerhans based on functional optical coherence microscopy”. Poster presented at the 5th Workshop on Imaging Pancreatic Beta Cell, NIH campus, Bethesda, 2013.
4. **Corinne Berclaz**, Anja Schmidt-Christensen, Daniel Szlag, Jerome Extermann, Lisbeth Hansen, Arno Bouwens, Frans Schuit, Anne Grapin-Botton, Theo Lasser and Dan Holmberg “Diabetes imaging with optical coherence microscopy”. Talk presented at the FOM conference, Göttingen, 2015.